Magnetic nanostructures for biotechnological applications

Ludgero Peixoto
Mestrado Integrado em Engenharia Física
Departamento de Física e Astronomia
2018

Orientador
Prof. Dra. Célia Sousa, Faculdade de Ciências

Coorientador
Prof. Dr. João Pedro Esteves de Araújo, Faculdade de Ciências

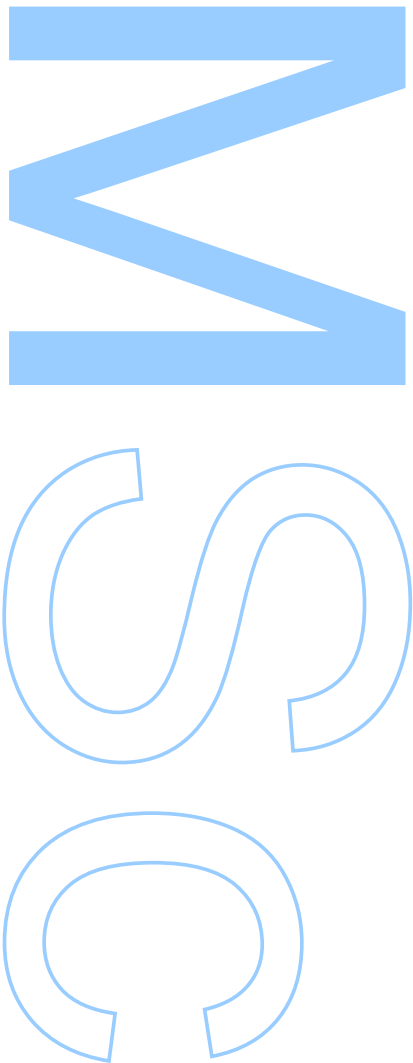

U.PORTO

FACULDADE DE CIÊNCIAS
UNIVERSIDADE DO PORTO

Todas as correções determinadas pelo júri, e só essas, foram efetuadas.

O Presidente do Júri,

Porto, _____/_____/_____

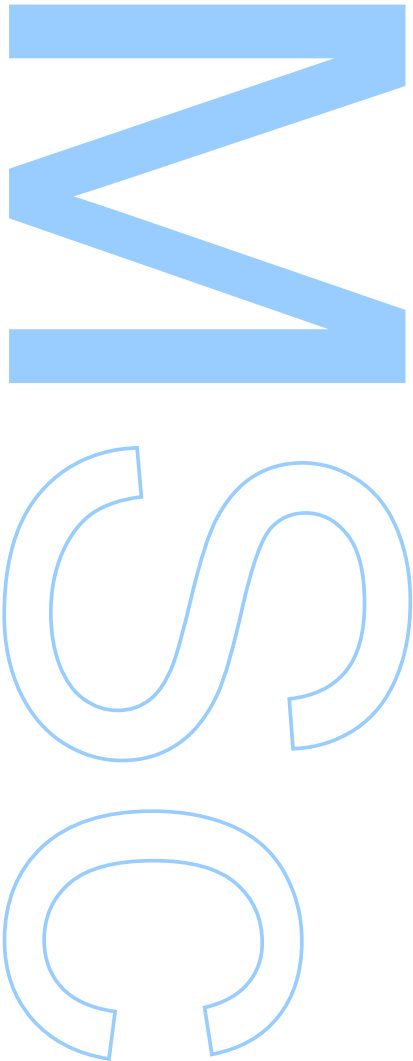

UNIVERSIDADE DO PORTO

MASTERS THESIS

Magnetic nano-structures for biotechnological applications

Author:
Ludgero PEIXOTO

Supervisor:
Célia SOUSA

A thesis submitted in fulfilment of the requirements
for the degree of Master of Science

at the

Faculdade de Ciências
Departamento de Física e Astronomia

December 2018

" I see now that the circumstances of one's birth are irrelevant. It is what you do with the gift of life that determines who you are. "

Takeshi Shudo

Acknowledgements

This work would have been a lot harder without everyone that supported me, one way or another. Firstly, I would like to thank my Supervisor, professor Célia Sousa, for all the kindness, guidance, continued support and overall help provided along the way. I would also like to thank my Co-supervisor professor João Pedro for allowing me to join this research group and for his always valued considerations.

Likewise, I would like to thank Rafael Morales, Carolina Redondo, Beatriz Mora from Universidade do Pais Basco and Sofia Costa Lima, Claudia Nunes, Salette Reis from FFUP. I would like to acknowledge the project H2020-MSCA-RISE-2016-734801 - MAGNAMED.

I am grateful to everyone that helped me at IFIMUP that always made me feel welcomed and taught me so much.

On a more personal note, a huge thanks to my family that were always there for me. To all the friendships made along the way, to the already existing ones, I am gratefull.

A special thanks to Mariana. For everything.

UNIVERSIDADE DO PORTO

Abstract

Faculdade de Ciências
Departamento de Física e Astronomia

Master of Science

Magnetic nano-structures for biotechnological applications

by Ludgero PEIXOTO

The advance in synthesis methods and the research of new magnetic effects [1] have been the driving forces that propel magnetic nanostructures to be used in several research fields, such as data storage and sensing [2–4]. In biomedical applications, magnetic nanoparticles, usually in the superparamagnetic state, are mainly used in drug targeting, in magnetic fluid hyperthermia (MFH) and as contrast enhancing agents [5–11]. Magneto-mechanically induced damage is a competing technique with MFH, for cancer therapy treatments, where instead of superparamagnetic particles, it prefers structures with a unique spin arrangement, namely micro/nano-discs in the spin-vortex state [12]. The main advantages of magneto-mechanical induced damage compared with MFH are the usage of lower frequencies and magnetic fields, as well as a lower concentration of particles [12]. Both techniques are important in cancer therapy research. MFH has already well-established research with clinical status [13] whereas magneto mechanical induced damage is in an earlier stage [12]. Taking into account the potential of micro-/nano-discs

for biomedical applications, the vortex state, how it behaves with aspect ratio and interdot distance and its potential applications are here reviewed.

To prepare magnetic nanostructures in vortex state, two different experimental routes were used: top-down and bottom-up, for nanodiscs and segmented nanowires, respectively. Nanodiscs with dimensions of about 500 nm have been fabricated by thermal evaporation and ion beam deposition on a substrate, patterned with interference lithography. The discs have been fully characterized with scanning electron microscopy (SEM), X-ray diffraction (XRD), superconducting quantum interference device (SQUID), magneto-optic Kerr effect (MOKE) and ferromagnetic resonance (FMR). The desired vortex state has been found in some particular of the samples.

Micromagnetic simulations were performed to determine the conditions needed for a vortex state in remanence and how it behaves with the interdot distance and aspect ratio. It was found that interdot distance equal to the discs' diameter is enough for the intereactions between discs to be considered negligeble. According to the simulations, a disc with an aspect ratio between 5 and 15 should sustain the vortex state in remanence.

Segmented nanowires (Fe and Cu) were electrodeposited in a porous alumina template obtained by hard anodization, with pore widening until pore diamter of 105 nm. The segmented nanowires were characterized by SEM and the behaviuor of the current density during the electrodeposition process was analised to undestand their morfology.The magnetic properties of the nanowires were acessed by VSM.

The thermally evaporated discs were released from the substrate by chemical etching of the sacrifical layer and used to study two fundamental paramenters for potencial biomedical application of these nanostructures: cell viability and cellular uptake. These discs were internalized and found to be innocuous to the cells, under no external magnetic field.

UNIVERSIDADE DO PORTO

Resumo

Faculdade de Ciências
Departamento de Física e Astronomia

Mestrado em (Engenharia) Física

Nano-estruturas para aplicações biotecnológicas

por Ludgero PEIXOTO

O progresso dos métodos de fabricação e a descoberta de novos efeitos magnéticos [1] tem levado a um crescente interesse em nano-estruturas magnéticas para serem usadas em diferentes áreas, como por exemplo *data storage* e *sensing* [2–4]. Em aplicações biomédicas, nanoparticulas magnéticas, normalmente no estado superparamagnético, são usadas em *drug targeting*, hipertermia magnética (MFH) e como agentes para melhorar o contraste [5–11]. *Magneto-mechanically induced damage* é uma técnica para a terapia de cancro que concorre com MFH, onde em vez de particulas superparamagnéticas, são usadas estruturas com estados magnéticos diferentes, nomeadamente o estado vortex [12]. As maiores vantagens desta técnica em comparação com MFH, são necessitar de baixas frequências, baixos campos magnéticos e menores concentrações de particulas [12]. Ambas as técnicas são importantes na pesquisa da terapia do cancro. MFH está num estado mais avançado, tendo estudos clínicos bem estabelecidos [13], comparado com *Magneto-mechanically induced damage* que ainda está, ainda, numa fase mais inicial[12]. Tendo noção

do potencial dos micro-/nano-discos para aplicações biomédicas, são aqui revistos o estado vortex, as suas dependências do *aspect ratio* e da distância entre discos, e as suas potenciais aplicações.

Para obter nanoestruturas magneticas no estado vortex, dois métodos experimentais foram utilizados: *top-down* e *bottom-up*, para nanodiscos e nanofios segmentados, respectivamente. Foram fabricados, por evaporação térmica e *ion beam deposition*, discos com dimensões de $\sim$ 500 nm num substrato padronizado por litografia de interferência. Estes discos foram caracterizados com uso a *Scanning Electron Microscopy* (SEM), *X-ray diffraction* (XRD), *Superconducting quantum interference device* (SQUID), *Magneto-optic Kerr effect* (MOKE) and *Ferromagnetic ressonance* (FMR). O estado vortex foi encontrado em certas regiões das amostras.

Simulações micromagnéticas foram feitas para determinar as condições necessárias para obter o estado vortex em remanência, e como se comporta com a variação da distância entre discos e do *aspect ratio*. A interação entre discos, separados mais do que o seu diâmetro, pode ser considerada como negligível. De acordo com as simulações, um disco com um *aspect ratio* entre 5 e 15 deve apresentar o estado vortex em remanência.

Nanofios segmentados (Fe e Cu) foram electrodepositados em templates de alumina nanoporosa obtidas por *hard anodization*, com diâmetro de poro de 105 nm, após o processo de alargamento do poro. Os nanofios segmentados foram caracterizados por SEM e o comportamento da densidade ce corrente foi estudado para compreender a sua morfologia. As propriedades magnéticas foram avaliadas por VSM.

Os discos produzidos por evaporação térmica foram libertados do substrato para ser estudada a viabilidade celular e a internalização destas nano-estruturas. Os discos foram internalizados e observou-se serem inócuos para as células, sem um campo magnético aplicado.

Contents

List of Figures

Abbreviations

MFM	Magnetic Force Microscopy
H_n	Nucleation Field
H_a	Annihilation Field
Py	Permalloy
EBL	Electron Beam Lithography
IL	Interference Lithography
NWs	Nanowires
XRD	X-ray diffraction
TEM	Transmission Electron Microscopy
SEM	Scanning Electron Microscopy
SQUID	Superconducting Quantum Interference Device
MOKE	Magneto-optical Kerr Effect
VSM	Vibrating Sample Magnetometer
LTEM	Lorentz transmission electron microscopy
MNPs	Magnetic Nanoparticles
FM	Ferromagnetic
SPM	Superparamagnetic
MRI	Magnetic Ressonance Imaging
MFH	Magnetic Fluid Hyperthermia
FMR	Ferromagnetic Ressonance

Chapter 1

Introduction

1.1 Vortex state in magnetic nanodiscs

As Brown's fundamental theorem [16] states, the competition between magnetostatic and exchange energies suppresses the formation of magnetic domains in very small magnetic particles, causing nanomagnets to behave as spins [17].

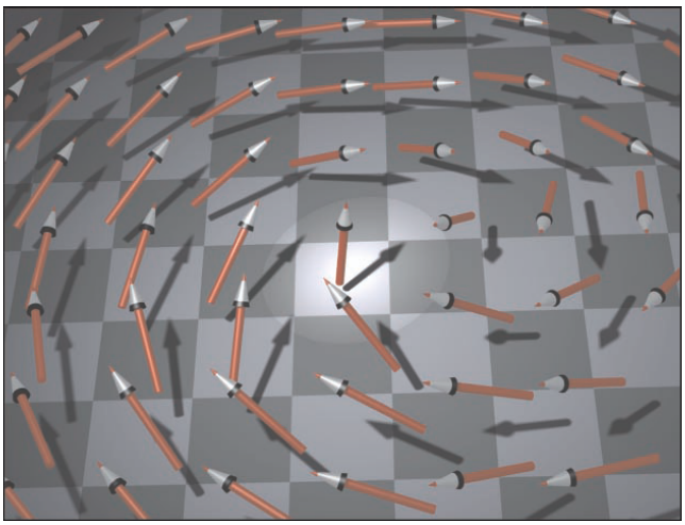

FIGURE 1.1: Vortex core schematic [18].

The geometry and aspect ratio of the structure is going to be a determinant factor to the spin configuration present in remanence. In micro/nano-discs, the minimization of energy forces the spins into a curling state, where the spin directions change gradually, starting parallel to the surface so as not to lose too much exchange energy, but to cancel the total dipole energy. Near the centre of the disc, the angles between adjacent spins increase until it is no longer possible to remain confined in-plane, resulting in a vortex core, with

magnetization perpendicular to the plane [19], as is illustrated in Figure 1.1. The shape of a vortex core is determined by the minimum of the total energy, which is dominated by the exchange and the magnetostatic or demagnetization energies. The vortex width is $w \sim 2\sqrt{A/K_d}$, where A is the exchange stiffness, $K_d = \mu_0 M_{sat}^2/2$ is the magnetostatic energy density and M_{sat} as the saturation magnetization [18].

The vortex-type remanent magnetization distribution is energetically favourable for the discs with weak magnetocrystalline anisotropy, [20] and is either deduced from the hysteresis loop's shape [17] or directly observed by magnetic imaging techniques like magnetic force microscopy (MFM) [21]. MFM experiments in soft magnetic materials must be, however, interpreted carefully since unavoidable tip-induced perturbations must be taken into account [22]. The shape of the hysteresis loop is the most used technique to study the vortex-sate and depends on the angle between the magnetic field angle and the disk array orientation [20].

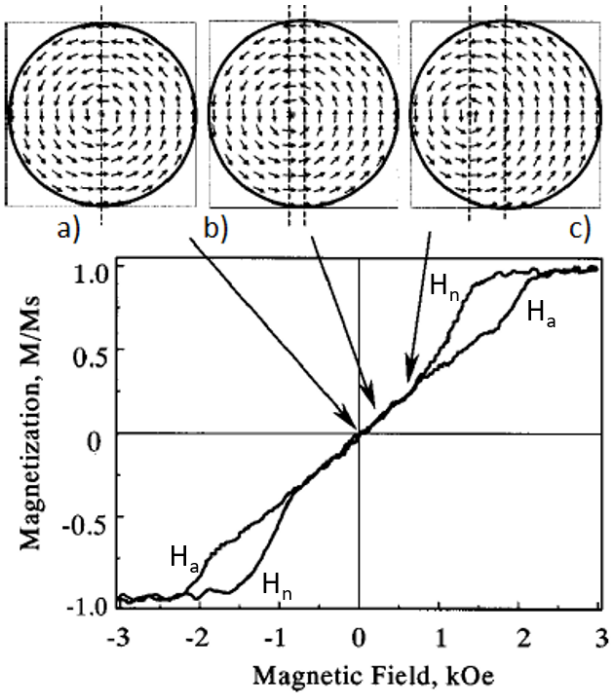

FIGURE 1.2: Hysteresis loop that shows vortex state, adapted from [20].

Figure 1.2 shows the magnetization dependence on the applied magnetic field. The loop was measured with a magneto-optical technique for the disc array with a thickness of 60 nm and diameter of 0.2 μm [20]. When the demagnetizing fields within each particle are no longer counterbalanced by the externally applied field, a magnetic vortex nucleates, being accompanied by an abrupt decrease in magnetization. The field at which this

phenomenon occurs is designated as the nucleation field, H_n. Then, a region where the magnetization responds linearly with the field follows, corresponding to the reversible movement of the vortex core and includes the remanent state with virtually no magnetization, that can be seen in Figure 1.2a. As the individual moments tend to align with field, this increasingly pushes the core to move perpendicularly to the direction of the field (Figure 1.2b and 1.2c). The continued decreasing of the field causes the vortex core to be expelled from the disc, marking the vortex annihilation field, H_a, after which the disc stabilizes in a single-domain state. The values of characteristic fields and the slope of the linear part of the hysteresis loop are strongly size-dependent. The nucleation and annihilation fields decrease with increasing the disc diameter [20, 23, 24]. The direction of the magnetization at the centre of the disc seems to turn randomly, either up or down, as up- and down-magnetizations are energetically equivalent without an externally applied field and do not depend on the vortex orientation. In contrast, after applying an external field perpendicular to the disc's plane, all centre spots exhibit the same contrast, indicating that all the vortex core magnetizations have been oriented into the field direction [19]. Arrays of magnetic structures whose geometry, size and spacing can be controlled in the fabrication process are an appropriate term for comparison with theoretical predictions. Magnetization reversal in the dot arrays is initiated in accordance with the balance of magnetostatic, exchange, and magnetic anisotropy energies when the interdot coupling is negligible. However, the magnetostatic interaction should be taken into account to describe the magnetic state of the patterned film, when interdot spacing is less than the lateral dot size. The dot shapes are also an important factor for coupling calculations in such close-packed dot arrays [23].

1.1.1 Fabrication methods and materials

Permalloy (80 % Nickel and 20 % Iron alloy; Py) discs have been extensively studied, being capable of bearing this spin structure, within a finite range of dimensions. Other materials that have also been studied include Supermalloy (75 % Nickel, 20 % Iron and 5 % Molybdenum alloy), Cobalt, Nickel and Iron. The main reports found in the literature are summarized in Table 1.1, where the materials, deposition and patterning techniques are shown.

The patterning needed to produce these nanostructures is usually achieved by means of lithography techniques. Optical lithography is a parallel writing technique used for

Ref	Material	Deposition Technique	Patterning
[12]	Py ($t = 60$ nm, $D = 1000$ nm)	Magnetron sputtering	OL
[20]	Py ($t = 60$ nm, $D = 200 - 800$ nm)	*	EBL
[25]	Au (5 nm)/Py (60 nm)/ Au (5 nm); $D = 2\mu$m	Thermal evaporation	ma-N 1410 resist as a milling mask
[26]	Au (5 nm)/Py (60 nm)/ Au (5 nm); $D = 1; 1,5; 2; 2,5\mu$m	Magnetron sputtering	OL
[17]	Supermalloy ($D = 55 - 500$ nm; $t = 6 - 15$ nm)/Au (5 nm)	electron beam evaporation	high-resolution EBL
[19]	Py ($t = 50$ nm, $D = 0,1 - 1\mu$m)	electron beam evaporation	EBL
[21]	$D = 150 - 1000$ nm, $t = 3; 5.5; 8.3; 15; 20$ nm	Thermal evaporation	EBL
[18]	Fe ($t = 8$ to 9 nm); lateral dimensions of 200 to 500 nm by 150 to 250 nm	Evaporation	self-organized growth of Fe
[27]	Cobalt/Al_2O_3/Py ($t = 0 - 30$/ $3/0 - 30$;$D = 300$ nm)	RF sputtering	EBL
[28]	Co ($15 - 40$ nm)/Au (6 nm); minor axis $= 250 - 375$ nm , major axis$= 400 - 600$ nm	thermal evaporation	IL
[23]	Py ($t = 80$ nm; $D = 0,2 - 0,4\mu$m)	electron beam evaporation	EBL
[24]	Py ($t = 40$ nm; $D = 500$ nm)	electron-beam evaporator	EBL
[29]	Py ($t = 5 - 50$ nm; $D = 0,8\mu$m)	dc magnetron sputtering	photolithography
[30]	Co ($t = 18 - 30$ nm; minor axis $= 250$ nm, major axis $= 450$ nm)	Thermal evaporation	IL
[31]	Fe ($t = 20$ nm; $D = 2\mu$m)	molecular beam epitaxy	EBL
[32]	Ni ($t = 16 \pm 1.5$ nm; $D = 40 - 90$ nm)	electrodeposition	X-ray IL
[33]	Py ($t = 25$ nm; $D = 700$ nm)	*	EBL

TABLE 1.1: Fabrication characteristics of the micro/nano-discs in vortex state reported in the literature (* No deposition technique mentioned).

large areas and dimensions, keeping in mind its high throughput capability but lack of high resolution. Over the years, many declarations of the demise of optical lithography were made, but each time the technology was salvaged by the introduction of various resolution improvements techniques such as changes in the exposure scheme, improvements in optical systems, exposure wavelength reduction and resolution enhancement technologies [34]. Rozhkova *et al.* [26] reported the fabrication process of disk arrays using optical lithography. The master mask had four different arrays covering a 3 cm^2 area each, with designed disk diameters of 1, 1.5, 2, and 2.5 μm arranged on a square lattice. The large area of the arrays produced 10^8 discs of each diameter from one cycle of microfabrication

[26]. The periodic or quasi-periodic nature of the pattern gives rise to the use of interfer-

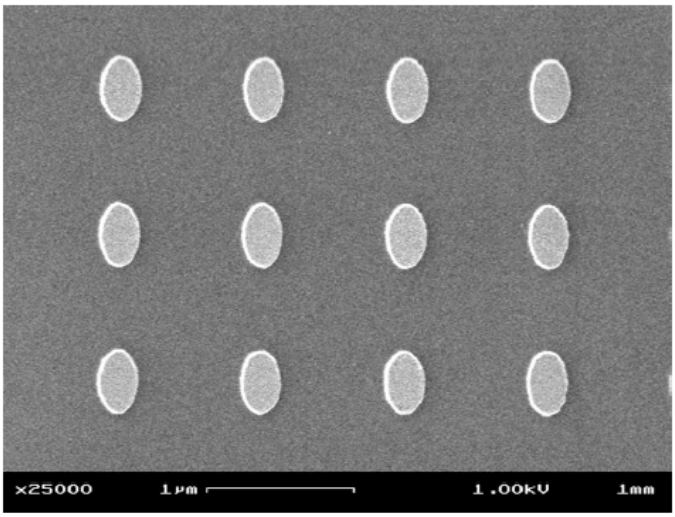

FIGURE 1.3: SEM images of an array of Co dots patterned by interference lithography [28].

ence lithography (IL), which is based on the interference of a small number of coherent laser beams to produce useful patterns over large areas. It is a mask-less technique able to pattern large areas while suffering from its resolution still being limited by diffraction [35]. Heyderman *et al.* [32] reported the use of interference lithography to fabricate arrays of nanoscale nickel dots which are uniform over 40 μm and have periods down to 71 nm. Combining extreme-ultraviolet light and interference lithography, magnetic dot arrays over large areas with periods well below 50 nm, and down to a theoretical limit of 6.5 nm for a 13 nm x-ray wavelength, can be fabricated [32]. Fernandez and Cerjan [28] used IL to fabricate an array of polycrystalline Co dots which can be seen in Figure 1.3. These dots measure 430 nm $\times$ 270 nm and are centred on a 1.0 μm grid. When higher resolutions are required and small patterned areas are enough, usually, the preferred techniques are ion beam lithography (IBL) and electron beam lithography (EBL), due to ultra-short wavelengths of ion/electron beams in the order of a few nanometres. Both of these techniques scan the surface of resist in a dot-by-dot fashion to generate the pattern, however, are more expensive and time-consuming than the above-mentioned alternatives. Cowburn *et al.* [17] reported the use of EBL, leading to a diameter distribution less than 2%, which means that all of the particles in the array are virtually identical to each other and so the measured average properties for the array can also be interpreted as the individual properties of a single nano-magnet.

To deposit the wanted metals, thermal and electron beam evaporation, are the more common options (Table 1.1). Thermal evaporation is the simplest and cheapest of the two options but the deposited films have poor density and adhesion. It is limited to low melting point metals and also suffers from a higher degree of impurities when compared with electron beam counterpart. Both of these techniques suffer from uniformity issues [36]. Sputtering comes as one alternative to improve the issue in uniformity, also enabling the use of more types of materials [37].

Another alternative would be to use bottom-up methods, where a combination of, for example, self-assembled nanoporous matrices and electrodeposition, enables the low-cost production of arrays of high vertical aspect-ratio nanowires (NWs), nanotubes (NTs), core-shell and multi-layered NWs, from a wide variety of materials [38–41]. Several works are reported in the synthesis of multi-layered nanowires ensures us that dimensions, where the vortex state is expected, can be achieved [42, 43]. Ivanov *et al.* [44] reported the use of densely packed cobalt nanowires arrays that can hold multiple stable magnetic vortex domains at remanence with different chiralities, fabricated by electrodeposition.

1.1.2 Physical characterization

After a successful deposition of the material with the desired pattern, a characterization of the sample follows. X-ray diffraction (XRD) is the main technique used for structural characterization, while transmission electron microscopy/scanning electron microscopy (TEM/SEM) give the morphological information. Despite these characterization techniques not allowing to identify the magnetic state of the samples (i.e. if vortex state is present), they provide information in regard of dimensions, shape and homogeneity as well as the crystallographic structure, which are fundamental to an accurate magnetic data interpretation.

There are essentially two different ways of magnetically characterizing the sample, either by direct observation or by inferring it from the hysteresis loop. MFM provides a direct monitoring of the reversal process. Fernandez and Cerjan [28] showed, in Figure 1.4, different images for various fields to investigate how the discs' reversal process occurs. Here it was observed the nucleation process's statistical nature, as the discs do not nucleate at the same field. MFM allows to directly monitor reversal in individual dots or in small groups of adjacent dots. However, this data must be carefully interpreted, as the magnetic stray field of the tip easily interferes with the vortex and its lateral resolution

typically being larger than the vortex core [22]. Wachowiak *et al.* [18] suggested the use of spin-polarized scanning tunnelling microscopy to address this issues if needed. Neal *et al.* [31] also showed that scanning Hall probe microscopy is also stated as a great promise technique since the Hall sensors are non-invasive and provide quantitative information about the out-of-plane component of magnetic induction.

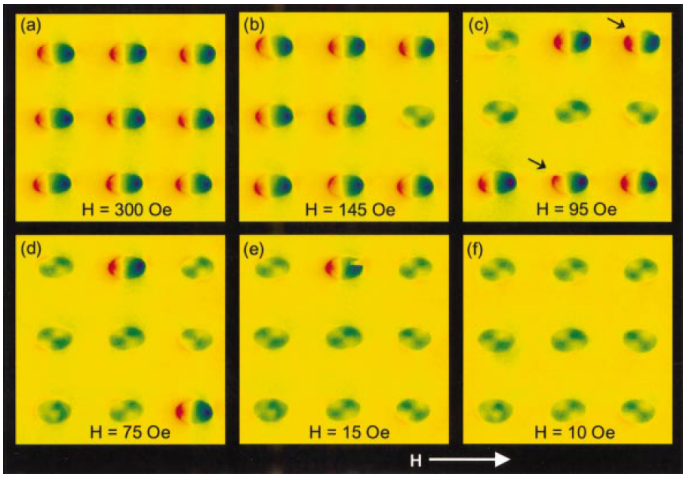

FIGURE 1.4: MFM images of 30 nm Co dots [28].

Measurements of the hysteresis loops provide an ensemble average of the reversal process and are usually performed with the Superconducting Quantum Interference Device (SQUID), Magneto-Optic Kerr Effect, (MOKE) or Vibrating Sample Magnetometer (VSM). VSM and SQUID are very sensitivity techniques but have a drawback, when measuring small/thin films the contribution of the substrate signal may mask the results, thus MOKE arises as a more surface sensitive technique. Several authors worked with MOKE to measure the magnetic properties of their samples [17, 20, 23, 27]. Also, others identified the vortex state using SQUID [30, 45, 46].

1.1.3 Magnetization reversal in arrays of discs *vs* isolated disc

1.1.3.1 Aspect ratio

The aspect ratio of the nanostructures is going to be determinant to the spin configuration present in remanence, so it is vital to understand which range of dimensions give us the vortex state. With this objective, a lot of work has been reported, where the magnetic behaviour of arrays of discs with different diameters and thickness was extensively studied.

Cowburn *et al.* [17] combined electron beam evaporation and EBL to fabricate various arrays of supermalloy discs with diameters ranging from 55 to 500 nm and thickness between 6 and 15 nm are studied. The results are summarized in Figure 1.5a, where different hysteresis loops for different dimensions are presented. Some of the loops do not show vortex behaviour, which allowed to experimentally determine a phase diagram, presented in Figure 1.5b. Here, also a theoretical line is shown. This line is not a prediction for the transition from vortex to single-domain behaviour but is rather a lower limit to that boundary, below which vortex nucleation is impossible [17]. The experimental results, also in Figure 1.5b, seem to corroborate the lower limit theoretical line, never crossing it.

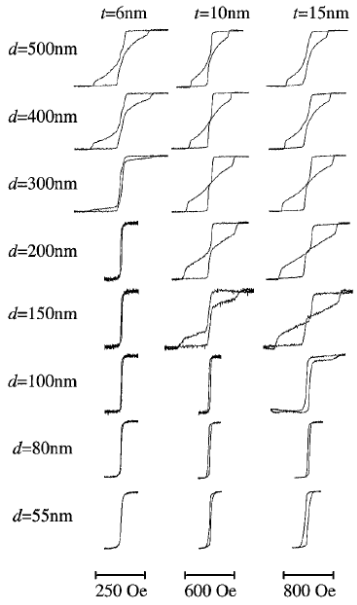

(A) Hysteresis loops measured as a function of diameter (D) and thickness (t)

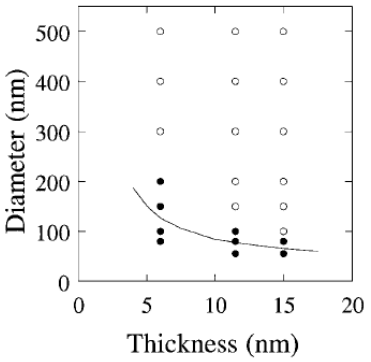

(B) Phase diagram (closed dots correspond to the samples without vortex state and open dots correspond to the samples where the vortex state was observed.

FIGURE 1.5: Magnetic behaviours for different aspect ratios [17].

Schneider *et al.* [21] developed the same type of study for flat permalloy cylinders with thickness of 3, 5.5, 8.3, 15, and 20 nm, and diameters varied between 150 and 1000 nm. This time, however, the characteristic vortex fields' dependence on the aspect ratio was the direct subject being studied, as is shown in Figure 1.6. These authors used the Fresnel mode of Lorentz transmission electron microscopy (LTEM) to obtain information about the micromagnetic properties of the permalloy discs. The sample was tilted under a constant field H_{OL} of the slightly excited standard objective (super twin) lens. The field was perpendicular with respect to the untilted sample plane, leading to an out-of-plane component $H_{\mathrm{OP}} = H_{\mathrm{OL}} \cos \alpha$, oriented parallel to the cylinder's z-axis, always present during the experiments and varying slightly for different tilting angles α. A single vortex

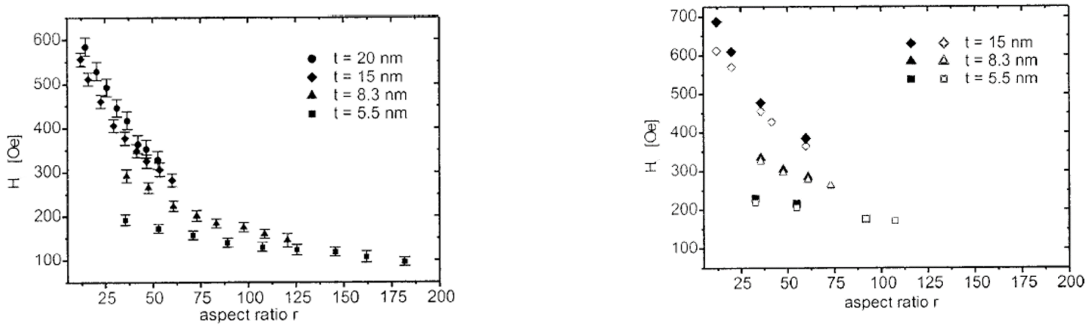

(A) Experimental LTEM data. (B) Simulated data.

FIGURE 1.6: Vortex annihilation field *vs* aspect ratio $r = D/t$. Closed symbols are simulated data; open symbols correspond to the LTEM experiment [21].

at H=0 was the initial magnetization configuration of both the LTEM observations and the micromagnetic simulations. The applied field was then increased to determine H_a for various values of thickness, t, and diameter, D. The vortex annihilation field H_a, obtained by the LTEM experiments, is plotted versus the aspect ratio $r = D/t$ in Figure 1.6a. If the thickness, t, of the cylinders is also considered, H_a is not only dependent on r, but also on t. These results are compared with micromagnetic simulations. The experimental data revealed good qualitative agreement with the simulations, in regard to the dependence of H_a on both, the aspect ratio r and the thickness t. The simulation also shows that the presence of a magnetic field H_{OP} perpendicular to the disc's plane, present in LTEM experiments, reduces the vortex annihilation field H_a (Figure 1.6b). The decrease of H_a depends on the thickness, as lower field values are needed for thinner cylinders. For large aspect ratios, the influence of H_{OP} decreases due to an increase in demagnetizing field ($H_{demag,z}$) along the cylinder z-axis, which is given by:

$$H_{demag,z} = -N_z M_z \tag{1.1}$$

where N_z is the demagnetizing factor, given by:

$$N_z \cong -4\pi(1 - \frac{\pi}{2r}) \tag{1.2}$$

in the very flat ellipsoid approximation [47] (for values of $r \gtrsim 10$), and M_z is the magnetization component parallel to the disc's z axis. Hence, demagnetizing field $H_{demag,z}$ counteracts and reduces the effect of H_{OP} more strongly for larger aspect ratios, r. The dependence of H_a on r for a given thickness t can be explained by the self-magnetostatic or stray field energy, E_{demag} . For a decrease in diameter D, the distance of the positive

and negative magnetic charges on the cylinder sides is reduced and yields an increase of E_{demag}. Thus, a vortex configuration is energetically more favourable due to reduced magnetic surface charges compared to the homogeneously magnetized disc. H_a thickness' dependence is the result of the different behaviour of E_{demag} and the exchange energy,E_{ex}, with aspect ratio r, diameter D, and thickness t of the cylinder. These authors state that, according to numerical simulations, E_{ex} of the single vortex configuration remains almost constant in applied magnetic field and E_{demag} increases strongly due to the increase of magnetization in applied magnetic fields. This different scaling of E_{demag} and E_{ex} can be seen by these rough approximations,

$$E_{\text{demag,SD}} = \frac{1}{8}\pi^3 M_s^2 r t^3 e \tag{1.3}$$

and

$$E_{\text{ex,SV}} = 2A\pi t \ln(\frac{rt}{2r_{\text{VC}}}) + \epsilon_{\text{VC}} r_{\text{VC}}^2 \pi t, \tag{1.4}$$

,where r_{VC} is the radius and ϵ_{VC} is the average energy density of the vortex core [48].

Figure 1.7 represents the vortex nucleation and its dependence with regard to the aspect ratio, r. The absolute value of H_n decreases with an increase in r, which means the states of high normalized magnetization M/M_s that precede the formation of the vortex—the single domain and intermediary states—are more stable at large values of r. This observation can be explained by the lower demagnetizing energy $E_{dmag,SD}$ (in Eq. 1.3), of elements with larger aspect ratio r. Even if in some cases the vortex nucleation occurred near zero, all observed cylinders of thickness $t = 5.5 - 20$ nm were in a single vortex state at $H = 0$ Oe. For $t = 5.5$ nm especially, but also for $t = 8.3$ nm, the single vortex is not centred in all of the discs, but is slightly displaced and therefore the remanent magnetization is non-zero. A reason for this can be the pinning of the vortex at positions where the energy has a local minimum due to surface roughness. These displaced remanent vortices also explain why the hysteresis loops of such elements are not always closed at zero applied field, even though the vortex is already present [21].

In another work, Schneider *et al.* [49] reported the study of the variation of the nucleation and saturation fields of circular permalloy discs, in respect to the diameter of the patterned elements. The thickness was maintained constant at 15 nm while the diameter was varied between 180 and 950 nm. In Figure 1.8, magnetic images of the nano-discs, obtained by LTEM, are shown with all nano-discs in the vortex state at remanence; the dark or bright spots in the disk centres indicate clockwise (CW) or counter-clockwise

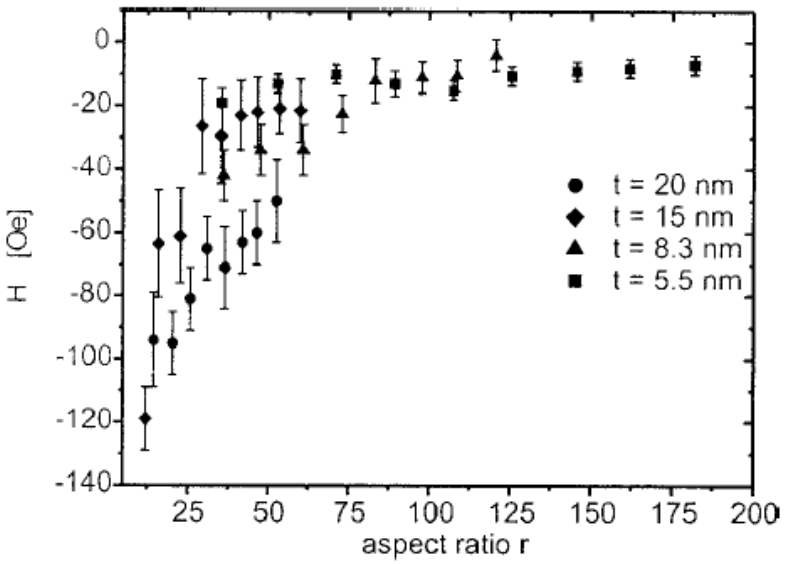

FIGURE 1.7: Vortex nucleation field vs aspect ratio $r = D/t$ [21].

(CCW) sense of rotation of the magnetization. The particles are separated by distances that caused less than 10 Oe of dipolar interaction between the particles if they were fully saturated and placed on a square array. The perpendicular magnetic component resultant

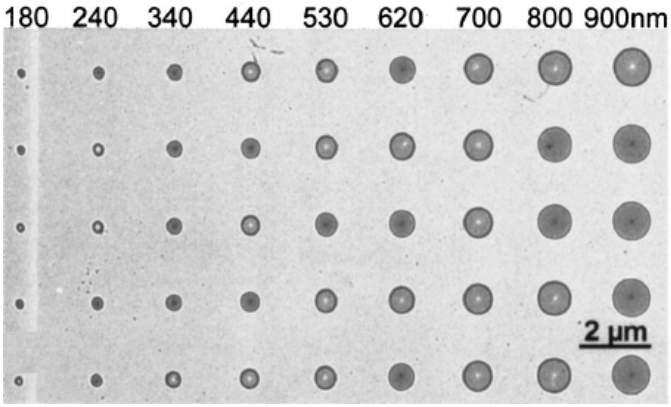

FIGURE 1.8: Images of vortex state in permaloy nanodiscs, as a function of the diameter, obtained by LTEM [49].

of the LTEM experiments' tilting of the sample, 1300 Oe, is regarded as small compared to the nano-discs' calculated out-of-plane demagnetizing field $H_{\mathrm{p,demag}}$, which takes values of 8.5 kOe for the smallest discs (d=180 nm) and 9.4 kOe for the largest discs (d=900 nm). This field is then assumed as not to interfere in the results. The nucleation field denotes the field value where first magnetization inhomogeneities become observable in a contrast variation within the discs. The saturation field strongly depends on the disk diameter D which can be explained by the increasing contribution of the magnetostatic self energy with decreasing diameter, whereas H_n is almost constant within the error margin

for larger disc diameters and increases for the smallest discs of diameter 180nm, as can be seen in Figure 1.9 [49].

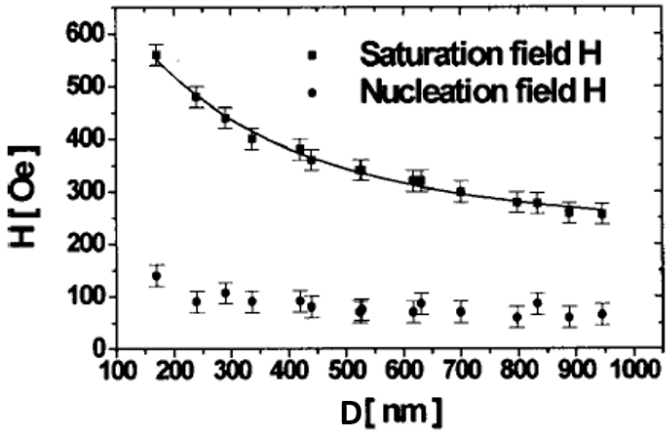

FIGURE 1.9: Values of saturation and nucleation field *vs* diameter [49].

Fernandez *et al.* [30] studied magnetization reversal in Co elliptical dots varying the thickness from 18 to 30 nm. When the 18 nm thick Co dots are saturated along their short-axis, 92% of them relax into a remanent state that can be seen in MFM images 1.10. The four equal quadrants that have alternating dark and light contrast are interpreted to indicate the presence of a single vortex, as shown in Figure 1.10. The rest of the dots either adopt a uniformly magnetized state parallel to the easy-axis or they relax into a double-vortex structure. It is to be noted that both signs of vortex circulation are reported, with equal probability and that the grey scales are said to be adjusted to maximize the contrast in the image, as the MFM signal is substantially weaker for the single-vortex state compared to the uniformly magnetized state (by a factor of ~ 5). The behaviour of the 30 nm dots is very similar to thinner ones, with two main differences. The tip perturbations do not allow a clear image of the remanent state; in the hard-axis, the uniformity of the response of the array improves, as almost all the dots are in a single vortex state (97%).

The easy-axis loop of 30 nm Co dots, shows a large remanence ($0.9M_S$) and a coercivity of 200 Oe. This represents an increase in coercivity of nearly 20 times over the sheet film coercivity [30]. By contrast, the hard-axis loop shows zero remanent magnetization. Moreover, the hard-axis loop is closed over a central portion of the loop. These results are viewed as consistent with the formation of a nearly flux-closed, single-vortex state at remanence. The closure of the loop near zero field implies that the vortices can move freely within the dots without being pinned by defects. The easy-axis and hard-axis loops are characterized by two relatively abrupt changes in magnetization, in both graphs of

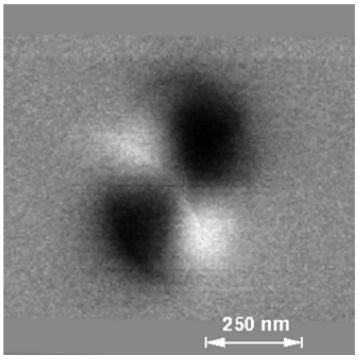

(A) MFM image of a single 18 nm thick Co dot after saturating the sample in the hard-axis direction and then removing the field.

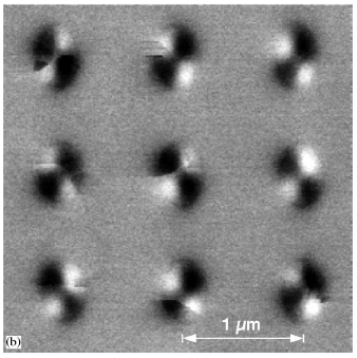

(B) MFM image of an array 18 nm thick Co dots in the hard-axis remanent state.

FIGURE 1.10: MFM Co dots hard-axis. The contrast here indicates that the dot has relaxed into a configuration in which a single vortex occupies the centre of the dot [30].

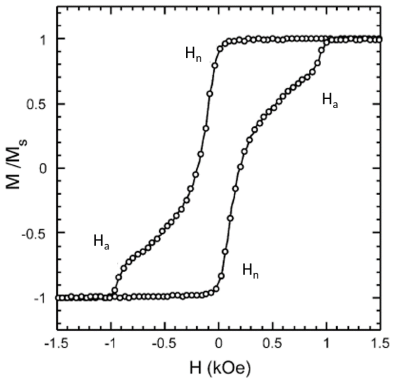

(A) The easy-axis loop.

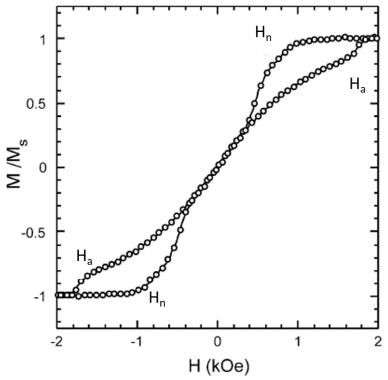

(B) The hard-axis loop.

FIGURE 1.11: Magnetic hysteresis loops for an array of 30 nm thick Co dots measured with VSM [30].

Figure 1.11. The significance of these transitions is clear from the MFM analysis. The first transition H_{n} marks the nucleation of a single vortex at one edge of the dots, while the second transition H_{a} marks the annihilation of the vortex at the opposite edge.

1.1.3.2 Effects of interdot distance

When considering an array of discs instead of an isolated one, the difference in behaviour comes from the magneto-static coupling between them. Thus, the inter-dots distance, d, is also an important factor for coupling calculations in close-packed dot arrays. Several authors have studied this subject as it is important for the correct modelling of real samples, which usually contains a high number of discs.

Experimental data and calculations reported by Novosad *et al.* [23] show a strong dependence of the vortex characteristic fields on the inter-dot distance. This is illustrated in

Figure 1.12, where are represented two hysteresis loops for arrays of discs with different distances between dots. The loops share the same shape, as expected of vortex-like behaviour but have different H_n and H_a. These values, as well as the slope of the linear part

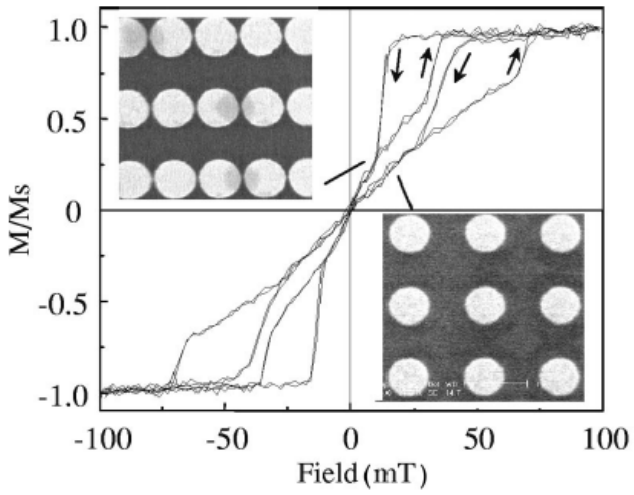

FIGURE 1.12: Hysteresis Loop Permalloy $D = 0.8\,\mu$m for different interdot distances, d, of 800 and 30 nm [23].

of the hysteresis loop, seem to depend not only on the dot diameter and the thickness but also on the inter-dot distance, as is summarized in Figure 1.13 and Figure 1.14. Here, it is shown that H_n and H_a decrease, whereas an initial susceptibility of the vortex increases with decreasing distance. The higher initial susceptibility means that the dot arrays with a strong inter-dot magneto-static coupling ($d < R$) have a higher mobility of the vortex core than an isolated dot with the same size. The decrease in the values for the characteristic fields may be explained by the higher effective field felt by each individual disc, from the contributions of the neighbouring discs. As the dot diameter increases, both H_n and H_a decrease according to the size-dependent in-plane demagnetizing factor [23].

Mejía-López *et al.* [50] reported the study of the role of the magnetic interaction between Fe nano-dots in arrays in the reversal process as a function of the centre-to-centre distance between dots, d. This study considered a system of Fe dots with $D = 65$ nm and $t = 20$ nm, with simulations performed to back up experimental measurements. In Figure 1.15, the variation of the characteristic vortex fields is shown in respect to the normalized distance (d/D). These authors proposed, however, that the closer the dots are to each other, the stronger their interaction is, and consequently, the larger the vortex nucleation field is. When the dot magnetization is mostly aligned in one direction, the inter-dot

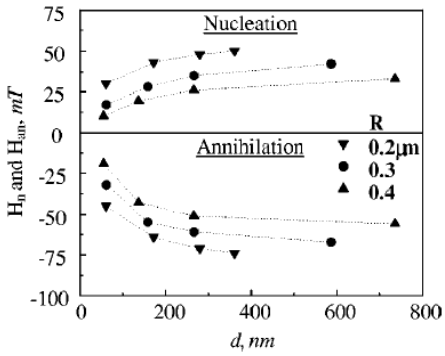

FIGURE 1.13: Experimental H_n and H_a in rectangular arrays as a function of the interdot distance [23].

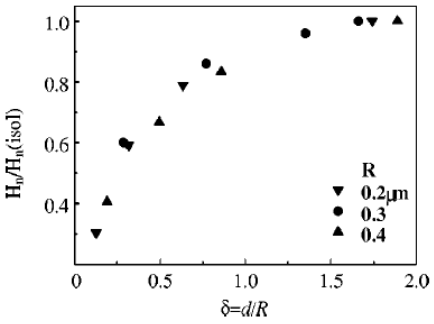

FIGURE 1.14: Normalized experimental nucleation fields vs normalized interdot distance δ [23].

dipolar interaction favours such a configuration, hence opposing vortex nucleation, creating an additional energy barrier for the transition to the vortex state, and increasing the vortex nucleation field. Contrary to Novosad *et al.* [23], these authors concluded that the annihilation field is also affected by the inter-dot interaction but to a lesser degree [50]. This is attributed to a much weaker dipolar interaction between the dots in a vortex state. In this work, it is stated that when $d \leq 2D$, the interaction between two magnetic dots is important and can significantly modify magnetic reversal. While it is only for $d \geq 3D$ that the hysteresis loop coincides well with the one for a single non-interacting dot, the shape of the hysteresis loop for $2D \leq d \leq 3D$, is very similar to the non-interacting case, as can be seen in Figure 1.16. Thus, for $d \geq 2D$ the magnetic properties of two interacting dots are well described by a statistical average of the magnetic properties of non-interacting dots.

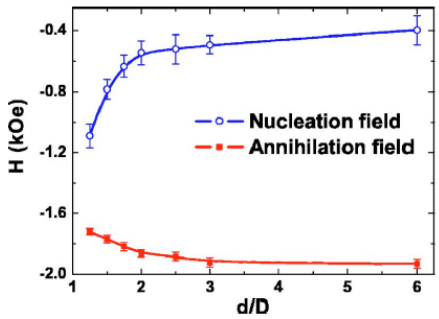

FIGURE 1.15: Vortex nucleation and annihilation fields calculated as a function of d/D [50].

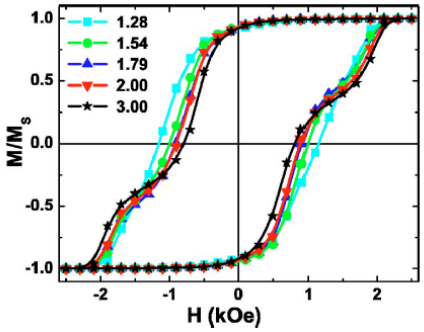

FIGURE 1.16: Hysteresis loops of the central dot interacting with its six nearest neighbors in an hexagonal dot array, for different inter-dot distances [50].

The difference between simulated and experimental data in Figure 1.17 is attributed to the distribution of dot sizes and imperfections of the shape of the dots in the experimental system. Also, the neglected inter-dot interactions, while not producing qualitative changes to the overall hysteresis loop shape, may contribute to some small quantitative corrections [50].

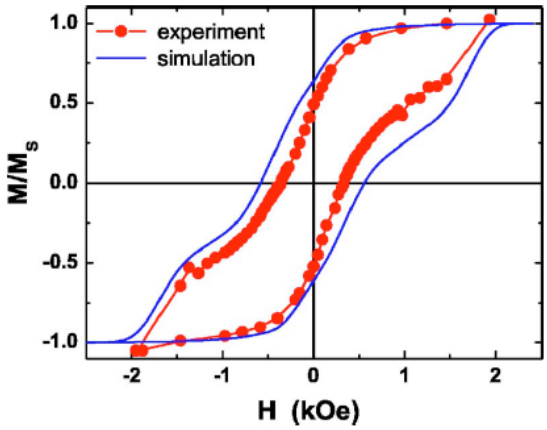

FIGURE 1.17: Hysteresis curve for an array with $t = 20$ nm, $D = 65$ nm and $d = 110$ nm [50].

Guslienko *et al.* [51] developed an analytical model for the magnetization reversal process which was then supported by micromagnetic simulations that can be seen in Figure 1.18 and in Figure 1.19. Decreasing the field leads to vortex nucleation being initiated in two dots located at the ends of the chain, as they are neighbour free on one side, and consequently under a smaller effective magnetic field than the more central dots. Once the discs at the edge nucleate a vortex state, their nearest neighbour discs are subsequently exposed to a reduced effective field, and the nearest neighbour discs can more easily nucleate a vortex [51]. At remanence, the centres of the vortices are at the centre of the dots. Therefore, the magnetic "charges" are practically absent and magneto-static interaction between the individual the dots is small, even for distances d close to zero. After applying the magnetic field, the vortices' centres are shifted and some magnetic "charges" arise on the dots boundaries, which increases the inter-dot magneto-static interaction. The vortices annihilate almost collectively in every dot, allowing us to regard them as identical. $\delta = d/R$ is a key parameter to compare the effect of magneto-static interaction on magnetization reversal in sub-micron dot arrays with different t and R. This is used to explain the hysteresis loop that accompanies this simulation, where the demagnetization curve for the chain exhibits a stepwise decrease because the vortices nucleate at different fields for the different dots [51].

The same conclusion is reached by Zhu *et al.* [24], as it is directly observed that vortex nucleation is first initiated in the two dots that have fewer neighbouring particles, located at the ends of the chains.

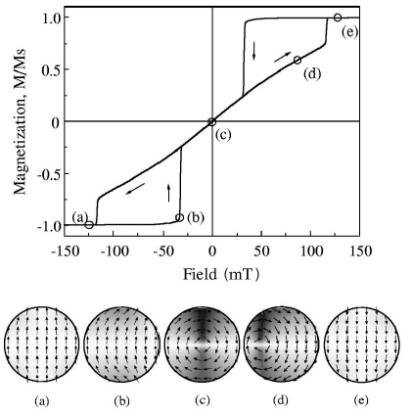

FIGURE 1.18: Hysteresis loops for simulated data of a chain of seven dots with $R = 0.2\mu$m, $t = 60$ nm and $d = 50$ nm [51].

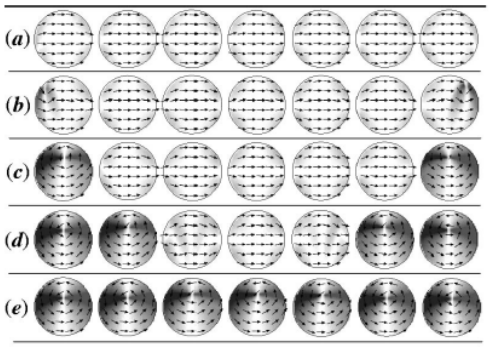

FIGURE 1.19: The evolution of the spin structure in the chain of circular dots for diferent fields [51].

Figure 1.20 illustrates a snapshot of a simulation from the work of Heyderman *et al.* [32], where the distance between dots, and their arrangement in the array, lead to the collective rotation of the magnetic spins. The authors considered that, rather than forming a vortex in each individual dot, the flux closure can occur through a series of dots to minimize the magnetostatic energy.

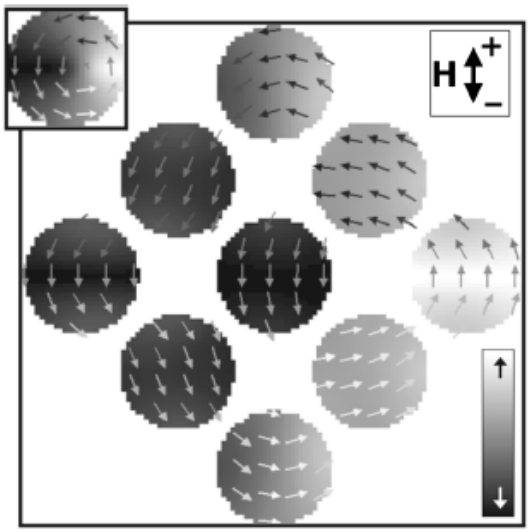

FIGURE 1.20: Snapshot of a micromagnetic simulation showing flux closure with $d = 50$ nm, $t = 16$ nm [32].

Neal *et al.* [31] studied the magnetization reversal in 2 μm diameter epitaxial Fe (1 0 0) discs using scanning Hall probe microscopy, supporting its findings with micromagnetic simulations. In this work, the simulations predicted the presence of a double vortex magnetization reversal process. Comparing the magnetic images and local induction loops at strategic points on the disc, seemed to agree well with this double vortex magnetization reversal mechanism. Despite being a study based on Fe, the dimensions and techniques used pull it apart from the intended in this thesis, not having any direct evidence of this type of magnetization reversal.

1.1.4 Potential technological applications

The possible application of ferromagnetic sub-micron elements in devices like non-volatile magnetic random access memories (MRAMs), small highly sensitive magnetic field sensors, or field programmable spin logic has increased both scientific and commercial interest due to the properties of ferromagnetic structures in the micron and sub-micron ranges [21]. In this context, the spin-vortex configuration attracted a lot of attention due to being characterized by an almost complete flux-closure, leading to negligible stray-fields and thus reducing problems with interactions between elements in close-packed arrays, e.g., in data storage systems. Another noteworthy property is that each vortex-state can carry two bits of information simultaneously, the chirality, c, (sense of rotation) and the polarity, p, of the vortex-core, either pointing up or down [27]. It is common to define $p = 1$ as the core pointing up, and $p = -1$ for pointing down; $c = 1$ when the magnetization curls counter-clockwise and $c = -1$ for clockwise. To be capable of sustaining a bit of information, these two properties need to be somewhat controlled, to allow for the writing/reading process to occur, but stable enough as to preserve the information until necessary. To change its polarization, the vortex has to overcome an energy barrier, which makes it quite stable against thermal fluctuations at room temperature or small magnetic stray fields [52]. Mainly two ways of such control have been reported, either by using a magnetic field pulse or an electrical current [53, 54].

The spin torque effect is the change of magnetization due to the interaction with an electrical current and can be used to control vortex polarity [55]. Liu *et al.* [53] proposed a fast and simple method to switch magnetic vortex cores by applying short electric current pulses, only one hundred picoseconds long. There, an electric current pulse is applied in

the plane of the element. Micro-magnetic finite-element simulations are used to investigate the current-driven magnetization dynamics, which can be seen in Figure 1.21.

The system considered was a disc-shaped Py sample of $D = 200$ nm and $t = 20$ nm thickness. The study uses short Gaussian-shaped current pulses (100 ps) of varying strengths. It was found that to obtain a core reversal, for the considered sample and for this pulse duration, the amplitude must exceed a minimum value of $j = 4.7 \times 10^{12}\,\mathrm{A/m^2}$. It is noted that this high current density might endanger the structural stability of the sample if it was applied continuously, which is avoided in the case where only ultra-short pulses are used. Compared with a magnetic field, an electrical current is much more appropriate to control a device since it can be handled with high precision and can be spatially restricted.

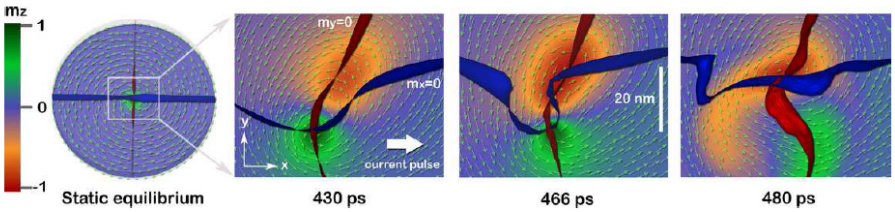

FIGURE 1.21: Current-induced vortex core reversal in a Py nanodisk $d = 200$ nm and $t = 20$ nm [53].

Antos and Otani [54] used micromagnetic simulations to show that the chirality of a vortex in a symmetric nano-disk can also be switched by an in-plane field pulse, because the information about the original state is still present inside the disk for a certain time (before arriving at the saturated equilibrium) so that a vortex with the opposite chirality can be nucleated after turning the field off at a suitably chosen moment. This method eliminates the need for inhomogeneity of the excitation, which has been introduced by a mask or spin transfer torque [54]. As it can be seen in Figure 1.22, turning off the field at different times ($t_{\mathrm{off}} = 836\,\mathrm{ps}$ or $t_{\mathrm{off}} = 988\,\mathrm{ps}$) yields vortices with different chiralities, thus this process is entirely controllable by choosing the appropriate pulse length.

1.2 Biomedical applications of magnetic nanostructures

Magnetic nanoparticles (MNPs) with controllable sizes and magnetic characteristics offer some attractive possibilities in biomedicine. Sizes ranging from a few up to hundreds of nanometres are smaller than or comparable to those of a cell ($10 - 100\,\mu$m), a virus

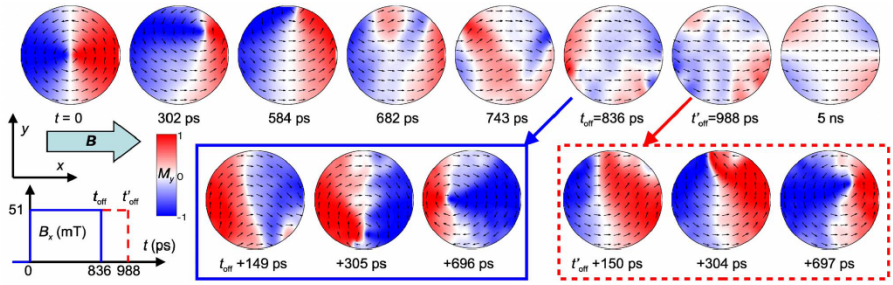

FIGURE 1.22: Vortex core reversa with an applied magnetic field pulse [54].

(20-450 nm), a protein (5-50 nm) or a gene (2 nm wide and 10-100 nm long) [5]. The intrinsic penetrability of magnetic fields into human tissue and the manipulability of MNPs leads to many applications involving the transport and/or immobilization of MNPs, or of magnetically tagged biological entities. The possibility of combining large magnetic moments and an ideal zero remanence, to avoid particle aggregation when the field is turned off, is also very attractive, as well as the ability to be coated with biological molecules to make them interact with or bind to a biological entity [56]. The magnetic response of the blood vessel itself includes both a paramagnetic response from the iron-containing haemoglobin molecules, and a diamagnetic response from those intra-vessel proteins that comprise only carbon, hydrogen, nitrogen and oxygen atoms. It should be noted that the magnetic signal from the injected particles, whatever their size, far exceeds that from the blood vessel itself. This selectivity is one of the advantageous features of biomedical applications of MNPs [5].

The magnetic properties of MNPs depend on their diameter. The critical radius for a magnetic particle to reach the single domain limit is equal to

$$R_{\mathrm{sd}} = \frac{36\sqrt{AK}}{\mu_0 M_{\mathrm{s}}^2} \tag{1.5}$$

where A is the exchange constant and K is the effective anisotropy constant [57]. Like bulk ferromagnets, an array of single domain magnetic nanoparticles can exhibit hysteresis in the magnetization versus field dependence. The key difference between the magnetic behaviour of a bulk magnetic material and a collection of single-domain ferromagnetic (FM) nanoparticles arises from the mechanism by which the magnetization is cycled through the hysteresis loop. In a bulk material, the magnetization increases in response to the field via domain wall nucleation and rotation as well as the rotation of the magnetization vector away from the easy axis of magnetization. In a single domain nanoparticle, domain wall movement is not possible and only coherent magnetization rotation can be used to

overcome the effective anisotropy (K) of the particle [13]. For a single domain particle, the amount of energy required to reverse the magnetization over the energy barrier from one stable magnetic configuration to the other is proportional to KV/k_BT where V is the particle volume, k_B is Boltzmann's constant and T is temperature. If the thermal energy is large enough to overcome the anisotropy energy, the magnetization is no longer stable and the particle is said to be superparamagnetic (SPM). That is, an array of MNPs each with its own moment can be easily saturated in the presence of a field, but the magnetization returns to zero upon removal of the field as a result of thermal fluctuations. High saturation magnetization in a low saturation field, no remanent magnetization and coercive field have been proven to be desired properties that characterize this type of particles, diminishing prominent inter-particle interactions, which normally leads to aggregations of particles. This way the temperature at which the thermal energy can overcome the anisotropy energy of a nanoparticle is referred to as the blocking temperature, T_B [57].

SPM particles have been widely studied for numerous biomedical applications, such as drug delivery [5, 8, 58], Magnetic Resonance Imaging (MRI) contrast enhancement [5, 57] and Magnetic Fluid Hyperthermia (MFH) [10, 13, 59]. Recently, however, other magnetic configurations, such as the vortex state, described in Section 1.1 have revealed themselves promising [12, 25, 26, 60]. In this section, it is given an overview of the more relevant and competing biomedical applications, concerning the use of MNPs; Magnetic Fluid Hyperthermia (MFH) and Magneto-mechanically induced cellular damage.

1.2.1 Magnetic Fluid Hyperthermia (MFH)

MFH is a cancer therapy technique that involves dispersing MNPs throughout the target tissue and then applying an AC magnetic field of sufficient strength and frequency to cause the particles' heating. If the temperature is maintained above the threshold of 42 °C for 30 min or more, the cancer is destroyed. Hyperthermia therapies usually are not viable because of the heating of healthy tissue but the use of magnetic nano-particles helps mitigate that weakness to some intent. The challenge here lies in being able to deliver an adequate quantity of the magnetic particles to generate enough heat in the target using AC magnetic field conditions that are clinically acceptable. Atkinson *et al.* [61] concluded that exposure to fields, where the product of the field amplitude and the frequency, $H \times f$, does not exceed $4.85 \times 10^8 \mathrm{Am}^{-1}\mathrm{s}^{-1}$ is safe and tolerable. However, in most instances, reducing the field strength or frequency to safer levels would almost certainly lead to

such a reduction in the heat output from the magnetic material as to render it useless in this application. Ferromagnetic particles' hysteresis leads to a magnetically induced heating, where the amount of heat generated per unit volume is given by the frequency multiplied by the area of the hysteresis loop. This is represented in equation 1.6, where P_{FM} is the power generated from the hysteresis loop, f is the frequency, H is the field and M the magnetization.

$$P_{\mathrm{FM}} = \mu_0 f \oint H \, dM \tag{1.6}$$

Any other possible heating mechanisms like eddy current heating and ferromagnetic resonance (FMR) are ignored, but these are generally irrelevant in the present context; the particles in question are much too small and the frequencies much too low for the generation of any substantial eddy currents and FMR effects may become relevant but only at frequencies far in excess of those generally considered appropriate for this type of application.

The revitalization of hyperthermia therapies came with the use of SPM particles suspended in water or in a hydrocarbon fluid to make a "magnetic fluid". Rosensweig [62] studied the physical basis of the heating of SPM particles by AC magnetic fields and demonstrated that

$$P_{\mathrm{SPM}} = \mu_0 \pi f \chi'' H^2 \tag{1.7}$$

, where P_{SPM} is the power generated from a SPM particle and χ'' is the out of phase component of the magnetic susceptibility. Measurements of the heat generation from magnetic particles are usually quoted in terms of the specific absorption rate (SAR) in units of Wg^{-1} [59], and multiplying it by the density of the particle yields P_{FM} and P_{SPM}, so this parameter allows for comparison of the efficacies of MNPs covering all the size ranges. Ferromagnetic materials require applied field strengths of about $100\mathrm{kAm}^{-1}$ or more before they approach a fully saturated loop, and therefore only minor hysteresis loops can be utilized given the operational constraint of $15\mathrm{kAm}^{-1}$, giving rise to low SARs. In contrast, SPM materials are capable of generating impressive levels of heating at lower fields. [5, 10].

Maier-Hauff *et al.* [63] reported the results of the first study into the feasibility of using MFH in human patients. The study involved patients with glioblastoma multiforme, a particularly severe type of brain cancer. SPM iron oxide MNPs were used ($\sim$ 15 nm) were dispersed in water at a concentration of 112 mg_{Fe} ml^{-1}. Each tumour was injected with from 0.1 to 0.7 ml of the magnetic fluid per ml of the tumour and then exposed to a

magnetic field of 3.8 to 13.5 kAm^{-1} alternating at 100 kHz. The study successfully demonstrated that this form of therapy using MNPs could be safely applied to the treatment of brain tumours and that hyperthermic temperatures could be achieved. Patient survival and local tumour control were not considered primary endpoints of the study, however, clinical outcomes were observed to be promising with the therapy being well tolerated by all patients.

Matsuda *et al.* [13] studied MFH an effective mesothelioma treatment by using MNPs with a diameter of 40 nm in all three histological subtypes of human mesothelioma cells (i.e., epithelioid NCI-H28, sarcomatoid NCI-H2052, and biphasic MSTO-211H cells). Table 1.2 summarizes the recorded average temperatures for each of the 3 cell types are shown for 3 different dosages, with an exposure time of 20 min. The frequency and intensity of the field were maintained constant at 325 kHz and about 500 Oe. While the temperature of the cell suspension without MNPs was maintained at about $30°C$ throughout the entire exposure time, a dose-dependent temperature rise was observed in all types of mesothelioma cells containing MNPs, suggesting the heating by intracellular MNPs. The different temperatures reached among the histological types could be due to the different amounts of intracellular MNPs in each cell type. In this work, it was reported there was no significant cell mortality with only the intake of the MNPs, and also a significant increase of cell mortality from the cells with MNPs when under an applied AC field.

Dose (μg/mL)	Average Temperature (°C)		
	NCI-H28	NCIH2052	MSTO-211H
0	31 ± 1	32 ± 1	31 ± 1
133	42 ± 1	46 ± 1	35 ± 1
267	51 ± 1	56 ± 1	40 ± 1

TABLE 1.2: Average temperature between 800 and 1200 s in the vicinity of the cells containing MNPs under an AC magnetic field (325 kHz, 500 Oe) for 20 min. [13].

1.2.2 Magneto-mechanically induced cellular damage

The use of the SPM nature of the nanostructures discussed requires a high magnetic field to enable their detection and manipulation. This gave an opportunity for a new kind of magnetic nanostructures to be studied, namely discs in a vortex-like spin configuration that could possibly work with smaller fields, lower frequencies and at lower concentrations.

Magneto-mechanically induced cellular damage is a cancer therapy technique competing with MFH that uses discs in the spin-vortex state. These discs possess unique properties such as high magnetization of saturation, zero remanence due to spin vortex formation (see Section 1.1), intrinsic spin resonance at low frequencies, and the capability of delivering various biomolecules at once. Due to their anisotropic shape, these particles are reported to rotate under an alternating magnetic field of small amplitude, experiencing a torque such that the plane of the disc aligns in a predetermined manner parallel with the direction of the magnetic field, as seen in seen in Figure 1.23. This was verified

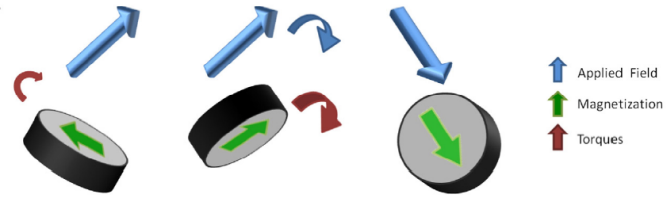

FIGURE 1.23: Discs movement with respect to the applied field [60].

by Rozhkova *et al.* [26], by measuring the intensity of the laser light travelling through an aqueous disc suspension that was monitored as a function of an external field parallel to the beam, which is shown in Figure 1.24 [26]. A clear distinction between two states

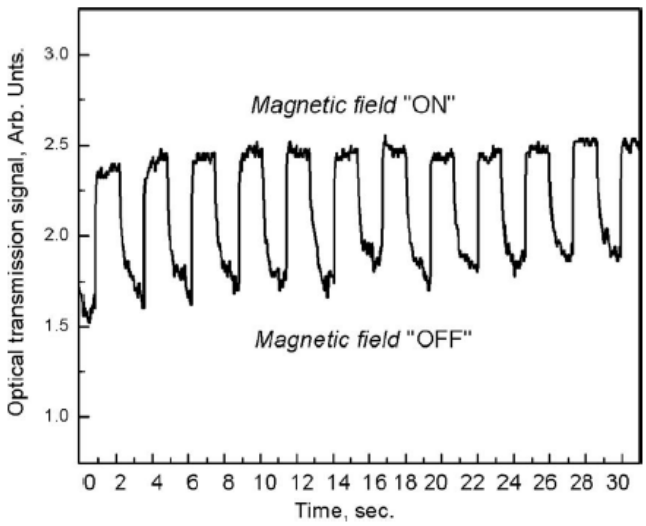

FIGURE 1.24: Laser transmissivity through an aqueous disc suspension modulated by an external field [26].

can be identified, which correspond to the magnetic field being "off" and "on". When the magnetic field, parallel to the laser beam, is turned on, the magnetic nano-discs suffer a before-mentioned torque which leads to them orientating parallel with respect to the field. This compared with the misaligned discs during the "off" state gives an increase

in transmissivity. By changing the pulse duration, it was found that a $2-5$ ms long field pulse of only 5 Oe amplitude is sufficient to achieve a complete rotation of suspended micro-discs, which is a considerably lower magnetic field when comparing with MFH (subsection 1.2.1). In this work, the discs were also prepared with gold surfaces for functionalization by a broad range of cancer-targeting bio-ligands, such as antibodies, peptide protein transduction domains, or nucleic acids aptamers, to allow specific binding to tumour cells in vivo. These authors reported the fabrication process, magnetic behaviour, as well as the surface modification of ferromagnetic micro-discs (5 nm Au/60 nm Py/5 nm Au with a diameter of 1μm) suspended in aqueous solution [26].

Kim *et al.* [12] reported the interfacing of whole cells with biocompatible lithographically defined ferromagnetic micro-discs with a spin-vortex ground state. When the biofunctionalized discs selectively bind to cancer cells, the mechanical force is efficiently applied to the membrane and further on to subcellular components. In this work, it was demonstrated that a spatially uniform and time-varying magnetic field as small as tens of Oe, with a frequency as low as a few tens of hertz and applied for only 10 min, is sufficient to achieve cancer-cell destruction in vitro. This antineoplastic [1] activity is the combined result of the compromised integrity of the cellular membrane and magnetic vortex- mediated initiation of programmed cell death. The discs were 60 nm thick Py with a diameter of about 1μm and the existence of magnetic vortices was experimentally confirmed by hysteresis-loop measurements, Figure 1.25. Here it can be seen zero in-plane magnetic

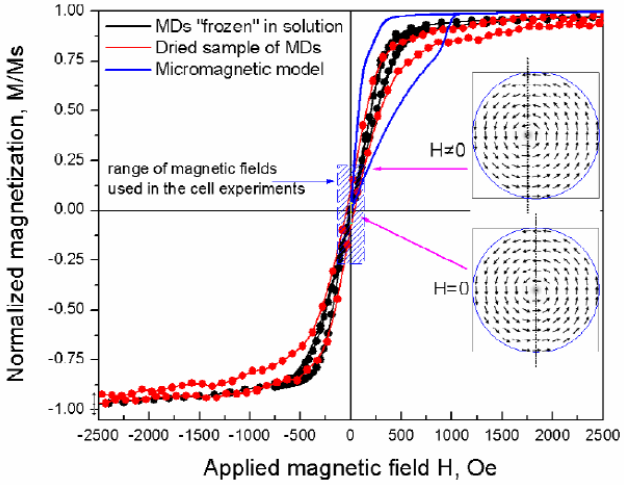

FIGURE 1.25: Hysteresis Loops [12].

[1] Acting to prevent, inhibit or halt the development of a neoplasm (a tumour).

moment in remanence, a linear $M(H)$ dependence in small fields and nucleation and saturation fields of 250 Oe and 600 Oe, respectively. With an applied field, the magnetization component parallel to the field creates a movement of the vortex core. The disc under the magnetic field will then experience a torque $\tau_m = m \times H$, where m is the disc magnetic moment, proportional to both M_s and the magnetic susceptibility, which will rotate the disc as to align its plane parallel to the direction of the applied magnetic field.

The magneto-mechanically induced cell damage was reported for an aggressive form of brain cancer, glioblastoma multiforme [12]. The specific targeting of micro discs to N10 glioma cancer cells was achieved by functionalization of the inorganic material with an anti-human-IL13α2R antibody, because IL13α2R is overexpressed on the surface of glioma cells and serves as a marker for targeting by cytotoxic elements, including nanoparticles. The anti-human-IL13α2R antibody was made to react immediately with the gold surface of the micro discs (hereafter referred to as MD–mAb). A similar procedure was used to modify the magnetic discs with isotype negative control antibody IgG1, which does not provide specific recognition of glioblastoma multiforme [12]. Initial evaluation of the magnetic-field-induced cell death of the MD–mAb relied on assay of cellular lactate dehydrogenase (LDH) released into a medium following the loss of cell membrane integrity. The cells were incubated with MD-mAb on ice for 1h for biding, thoroughly washed and exposed to a spatially uniform AC magnetic field of 90 Oe, with a frequency of < 60 Hz. In all experiments, an average of 10 discs per cell is reported to be used. After magnetic-field exposure, the cells were cultured under standard conditions for recovery. LDH release was tested after 4 h. No significant effect was observed when the discs were functionalized with the isotype-matched negative control IgG1 were used. By contrast, AC magnetic-field-induced MD–mAb showed pronounced cell death as summarized in Figure 1.26. It is reported that the maximum ($\sim$ 90%) effect was detected at low frequencies (10 and 20 Hz), and for more quickly varying fields (40 and 50 Hz) of the same amplitude, a rapid fall in the LDH release (to 75% and 25%, respectively) was reported in Figure 1.26. No significant toxicity was detected at 60 Hz. The falling toxicity with frequency is due to the decrease in disc oscillation amplitude at higher frequencies when the discs are unresponsive to the rapidly changing field, and thus do not affect the cell membrane integrity. To exclude hyperthermia as a possible mechanism of cell damage, the temperature was monitored remotely with an infrared camera, showing it not varying more than a few degrees. The observed LDH leakage is then attributed to targeted

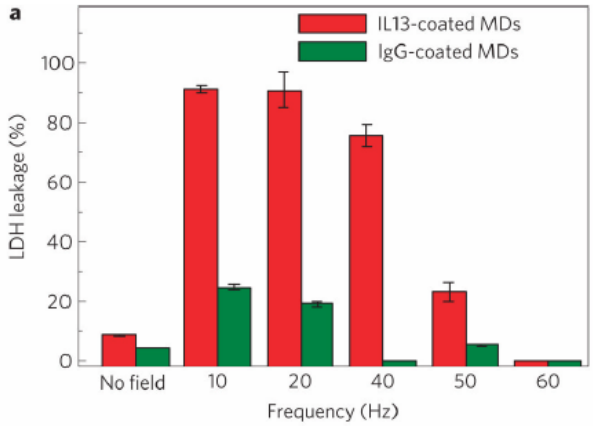

FIGURE 1.26: LDH leakage variation with frequency [12].

membrane rupture or magneto-mechanically induced cell destruction.

Cheng *et al.* [60] tested the in vitro toxicity of 2 μm diameter Py discs with 60 nm of thickness, protected by a 5 nm layer gold cap on either side. The U87 human glioma cells used were loaded with 50 discs per cell and after 24 h of incubation, nearly 100% of U87 glioma cells were observed to have internalized the discs, despite not being functionalized, with no apparent alteration in cellular morphology. The samples were then exposed to a rotating magnetic field of 1 T at 20 Hz, for 30 min. The cells were reported to be visibly disrupted, which lead the authors to suggest that the discs can create a mechanical force that disrupts the cellular integrity.

Mansell *et al.* [25] compared the efficiency of two types of 2 μm diameter discs, antiferromagnetic (CoFeB/Pt) and with vortex (Py), for mechanical cancer cell destruction, under an applied rotating magnetic field. These two sets of discs were incubated with human U87 brain tumour cells for 24 hours at a concentration of 50 particles per cell, without functionalization, and were observed to be internalized. The cells were then subject to a minute of applied rotating field os 10 kOe, after which their viability was investigated. These authors found that the antiferromagnetic discs were more efficient for destroying cancer cells than the Py discs, in the vortex state. Mora *et al.* [46] reported the fabrication and full characterization process of two sets of Py discs (D= 650 nm and t=50 nm; D= 450 nm and t=25 nm) and their study with cell viability. The toxicity of the Py discs was assessed in primary melanoma cultures. A375 skin cancer cells were incubated for 24 hours with different concentrations of the 650 nm in diameter and 50 nm in thickness discs were used. This being 0 (control), 40, 60, and 140 discs per cell. These authors found that, with an incubation period of 24h, without an applied magnetic field, the discs were

innocuous, highlighting how these structures are excellent candidates for studying in new biotechnological applications.

Kim *et al.* [12] also provides a comparison between this technique and the well-explored use of magnetic nanoparticles to achieve hyperthermia effects. The main problems with magnetic hyperthermia are invasiveness, targeting (restricting the hyperthermia effect to the specific area of interest) and achieving homogenous heat distributions within the target organ which may lead to either insufficient treatment effects or lethal exposure of neighbouring cells. In contrast to hyperthermia treatment, magneto-mechanic stimulus induced by micro discs is transmitted directly to the targeted cell with high specificity and high efficiency. Owing to the use of a magnetically soft material with a unique spin arrangement, namely a spin-vortex state, the biologically relevant effect was achieved through the application of weaker magnetic fields < 100 Oe of a frequency of a few tens of Hz, applied for a duration of only 10 min. This contrasts with the much stronger fields of frequencies of hundreds of kilohertz, required to achieve heating-induced cell toxicity with SPM particles. In this experiment, it is reported that the external power (proportional to fH^2) supplied to cell cultures were on average at least 100,000 times smaller than that used at present in hyperthermia treatments with MNPs.

Chapter 2

Experimental details

In this chapter, a brief description of the sample fabrication and characterization methods will be given.

2.1 Fabrication techniques

The samples were either fabricated by two different approaches, top-down and bottom-up. In the top-down route, a substrate patterning was performed by interference lithography, followed up by thermal evaporation/ion beam deposition. In the bottom-up route, nanoporous alumina templates were fabricated, followed by electrodeposition.

2.1.1 Top-down route

The top-down approach is described below. This method refers to the building of new micro/nao-structures (nanodiscs) from larger structures (metallic target).

Starting with a silicon substrate, the anti-reflective coating (ARC) WIDE-8B was spin coated at 5000 rpm for 60 seconds and baked on a hotplate in two steps: 40 seconds at 100 ºC and then 60 seconds at 180 ºC. The negative resist tone (TSMR-IN027) application followed. It was spin coated on the ARC at 400 rpm for 60 seconds followed by a baking step at 90 ºC for 90 seconds which led to a 280 nm resist stack. The sample was patterned by use of interference lithography immediately after the spin coating steps (same day), to prevent resist ageing.

2.1.1.1 Interference Lithography

Interference lithography is a maskless patterning technique that takes advantage of the repetitive nature of the desired pattern. Two, or more, coherent beams, with the same polarization, are made to interfere and project the interference pattern (Figure 2.5) on the resist. Here, the beams are symmetrically incident at angels of $\pm\theta$ and the period of the interference pattern is $\lambda/2n\sin(\theta)$. A simple experimental set-up is represented in Figure 2.1b where the beams are folded onto each other with $\theta \sim 45$ °. After exposure, the photosensitive material is developed, revealing the desired periodic pattern.

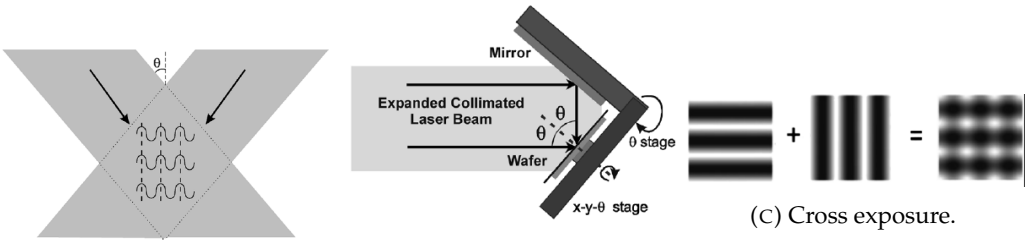

(A) Cross exposure.

(B) Experimental arrangment of Interference Lithography from Brueck [35].

(C) Cross exposure.

FIGURE 2.1: Interference lithography schematics

The system, where our samples were made, used a Lloyd's mirror interferometer with a He-Cd laser ($\lambda = 325$ nm) as a light source. After the first exposure (7 minutes), another exposure (also 7 minutes), rotated 90°, was performed to yield a square array of dots, as schematized in Figure 2.1c. Controlling the exposure dose, changing the angle of incident light or rotating the sample holder, one can easily adjust the periodicity of the array and the lateral size of the pattern. The exposed resist was post-baked at 110 ºC for 90 seconds and developed in AZ 736 MIF for 1 min. Finally, the samples were cleaned with deionized water for 90 seconds and dried with nitrogen.

2.1.1.2 Thermal Evaporation

Thermal evaporation is a physical vapour deposition (PVD) method, of high deposition rates, where the material source is heated (resistive heating), in a vacuum chamber, to high temperature so that its surface atoms have sufficient energy to leave the surface. The atoms will then traverse the vacuum chamber, at thermal energy, and coat a substrate. The pressure in the chamber must be below the point where the mean free path is longer than the distance between the evaporation source and the substrate. This deposition method

was used for the first batch of samples. The base pressure used ranged from 3×10^{-6} to 6×10^{-6} mbar, while the work pressure was around 10^{-4} mbar. The experimental set up can be observed in Fig. 2.2a, where a home-made vacuum chamber was used. The vacuum was supplied by the combination of a rotative and a diffusion pumps.

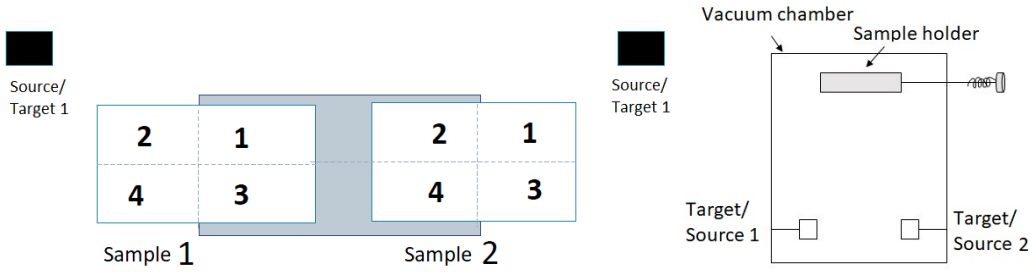

(A) Front view.

(B) Side view.

FIGURE 2.2: Experimental set-up for the thermal evaporation.

A cross-section view of the discs can be found in Fig. 2.3a. The 27 nm thick Al layer serves as a sacrificial layer, allowing the removal of the discs from the substrates. The 10 nm Au caps are to protect the sample from oxidation. The Al and Fe layers were deposited using Source 1, with deposition rates of 3.5 nm/min and 1 nm/min, respectively. The Au layers were deposited using Source 2, with a deposition rate of 2.2 nm/min.

(A) Thermally evaporated discs.

(B) Ion beam deposited discs.

FIGURE 2.3: Cross section view of the multilayered discs.

2.1.1.3 Ion Beam Deposition

Ion beam deposition (IBD) is also a PVD method that produces high-quality films with excellent precision. The IBD system used, Figure 2.4, consists of an ion source, a target and a substrate. The ion beam source features a discharge chamber, where the ions (Ar^+)

	Cathode	Discharge	Beam	Accelerator
Current (A)	6.8	2	0.0065	0.0007
Voltage (V)	5.4	38	1000	148

TABLE 2.1: Typically used values for Ion Beam Deposition.

are generated and grids with a negative potential, relative to the ground, which is responsible for the acceleration of the ions to a high velocity. The ion beam focuses on a target material, and the sputtered material then deposits onto the substrate.

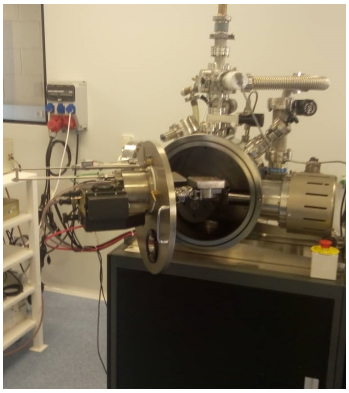

(A) IBD image.

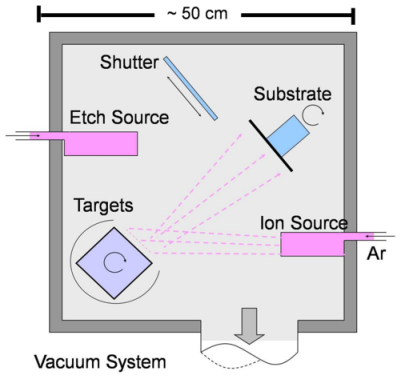

(B) IBD scheme.

FIGURE 2.4: IBD image.

This system was used to produce multi-layers of thin films, as schematized in Figure 2.3b, as well as deposited in the patterned substrate. The high base vacuum achievable; the low and well controllable deposition rate made this an appealing choice. The IBD was used to deposit layers of Aluminium (30 nm), serving the purpose of the sacrificial layer, Titanium (10 nm), to prevent oxidation, Iron (from 30 to 90 nm) and once again Titanium (10 nm). The deposition rates for Al, Ti and Fe are, 0.54, 0.31 and 1.06 $\text{Å}/s$, respectively. The targets were cleaned for 2 min before and between depositions. The base pressured ranged from 3×10^{-7} to 6×10^{-8} Torr, the work pressure was 1.4×10^{-4} and the rest of the used parameters for the IBD are presented in table 2.1.

2.1.2 Bottom-up route

Another fabrication method used was the template-assisted electrodeposition in porous anodic alumina (PAA) templates, a bottom-up approach which starts with building blocks such as atoms, molecules, etc., whose assembly is controllable.

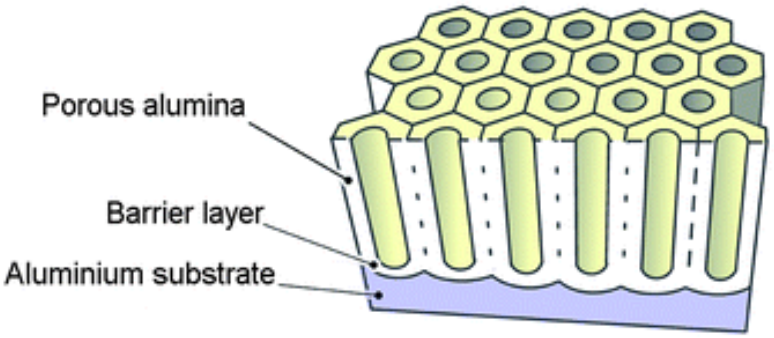

FIGURE 2.5: Scheme of PAA adapted from [14].

2.1.2.1 Porous anodic alumina (PAA) templates

Aluminium becomes rapidly coated with a thin oxide layer, in ambient atmospheres, called the native layer. This layer serves to prevent the further oxidation of the metal surface. Anodization refers to the phenomenon where the Al is electrochemically oxidized, to produce a thicker oxide layer than the native one. It is called this way because the Al is de anode in the electrolytic cell when the reaction takes place [41]. Two different morphologies can be formed by the anodic aluminium oxide (AAO) films, nonporous (continuous film) and porous (PAA). This depends mainly on the nature of the electrolyte used for anodization [64]. Focusing on the PAA, it's divided into two parts, a thin oxide barrier layer which is in conformal contact with the Al and a relatively thick porous oxide film composed of nanopores extending from the oxide barrier to the surface of the film. These nanopores, in specific electrochemical conditions, self-organize into a close-packed hexagonal arrangement [65, 66].

The pre-treatment of the substrate is of foremost importance when dealing PAA since the surface morphology and purity influences a lot the organization of the template.

Substrate cleaning An Al foil (99.997% purity) was cut in squares of 1.5 cm^2 and subsequently pressed to level the surface. The samples were rinsed in ultrasound baths of acetone and ethanol for 3 minutes, without passing them through water since the electropolish solution was hydrophobic.

Electropolishing Electropolishing is the electrolytic removal of a metal in an ionic solution by means of an electrical potential and is used to remove a thin layer of undesired materials on the surface of the metal. This process also improves the Al surface prior to the anodization, by smoothing the peaks and valleys [67]. The set-up used, observed in

Fig. 2.6a, consisted in a metal substrate (anode) and a platinum mesh (cathode), which were in an electrolyte solution that establishes an electric circuit with a DC voltage applied. The temperature of the electrolyte had to be controlled (bellow 10°) and the DC voltage (20V) was applied for two minutes. After this process the substrates were rinsed with ethanol, followed by deionized water and thus ready to be anodized.

(A) Electropolishing.

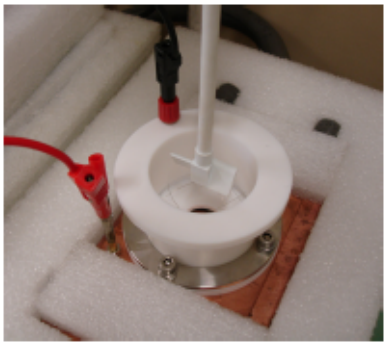

(B) Anodization cell.

FIGURE 2.6: Experimental set-ups [15].

Anodization The electrochemical cell used consists of a Teflon container with the Al substrate (working electrode) placed in a small hole, on the bottom, and a Pt mesh is inserted at the top (counter electrode), Figure 3.14b. An O-ring is used to prevent any leakage between the sample and the container. The anodization was performed under constant potential and the current monitored as a function of time using a digital source meter (Keithley 2400 C) controlled by a home-developed LabVIEW program. The source meter was connected to the Pt mesh and to a Cu plate in direct contact with the Al sample. The anodization of the samples was performed in two steps, always with the oxalic acid ($C_2O_4H_2$) as the electrolyte, with 0.3 mol/L. In the first step, 40 V applied for 10 minutes (mild anodization conditions) while keeping the temperature around 3°C. This creates a thin PAA template to suppress breakdown effects caused by the high current densities, used in the second step. An increased rate of 0.5 (or 0.6) V/s follows, to get the hard anodization step at to 140 (or 150) V (hard anodization). This voltage was applied for three hours, being followed up by another minute with 40 V, to stabilize the barrier layer at the bottom of the pores [38].

Aluminium removal and Pore widening After the anodization process, the Al is removed from the samples using 0.2 M $CuCl_2$ in a 4.1 M HCl aqueous solution, at room

temperature. The opening of the pore and consequently widening was done using a solution of 0.5 M $H3PO_4$ at room temperature. A thin Au layer was then sputtered on the backside of the membrane to serve as the working electrode.

2.1.2.2 Electrodeposition

Electrodeposition is a chemical deposition method with a high growth rate in which an electrolyte solution is used to deposit material in a conductive substrate. The set-up used for electrodeposition was similar to the anodization, with the PAA template as the cathode and Pt mesh as the anode. A LabVIEW routine was used to control the process. The electrodeposition used was a method of co-deposition of Cu and Fe. The solution used allows for both of the metals to be deposited, consecutively by applying different static potentials. Firstly, a gold layer was electrodeposited for 5 min by applying 1 V to ensure a more homogeneous contact for further electrodepositions (Figure 2.7). After this a layer of Cu was deposited with an applied potential of -0.6 V, following up with a shorter deposition of Fe, at -1.1 V. This process was repeated to produce 15 bilayers of electrodeposited material. While depositing Fe, as it has a higher potential, some Cu will be deposited as well, but the impurities are negligible, since the Cu concentration is considerably lower than the Fe concentration [68].

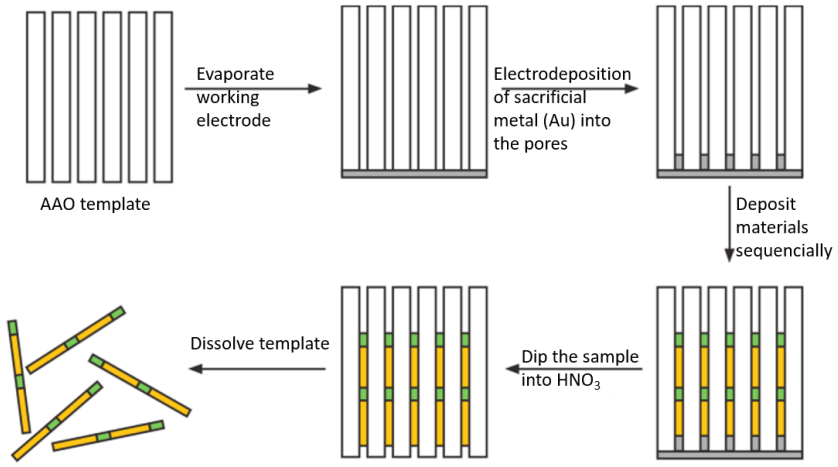

FIGURE 2.7: General scheme for electrodeposition (ED) of materials into porous AAO adapted from [41].

2.2 Characterization methods

The film structure and morphology were characterized by X-ray diffraction and scanning electron microscopy, respectively. The magnetic properties were assessed with superconducting quantum interference device, magneto-optic Kerr effect and Ferromagnetic resonance.

2.2.1 Scanning electron microscopy

Scanning electron microscopy (SEM) uses a high energy electron beam to study the samples morphology. With the beam focused on the sample and with a set of magnetic lenses that control its motion, on the surface, an image of the detected electrons after the interaction with the sample surface can be created. The most commonly used modes are secondary electrons, backscattered electrons and energy-dispersive X-ray spectroscopy (EDS). Secondary electrons obtain energy from inelastic collisions with weakly bonded electrons. Their intensity is dependent on the depth of the interaction which makes them a useful tool to image the topography of the surface. Backscattered electrons are the result of an elastic backscattering with sample electrons. Larger atoms have a higher probability of scattering electrons, the brighter the spot the larger the atomic number. The secondary electrons mode reveals fundamental information about the morphology of the sample, while the backscattered electrons complement it with a chemical signature of the sample. The origin of the characteristic X-rays is in the atomic deexcitation when an outer shell electron, originally occupies an empty place on an inner shell that was left empty by an electron extracted due to the energy transferred from the incident electrons. As the energy difference between core shells differs for each atomic species, the chemical composition of the sample can be identified just by detecting the emitted x-rays and by and comparing it with known X-ray emission energy values. The device used to characterize our samples was a FEI Quanta 400FEG high resolution (HR) SEM.

2.2.2 X-Ray diffraction

X-ray diffraction (XRD) analysis allows for the identification and structural characterization of the samples. The diffraction pattern arises from the interaction between the X-rays and the electrons in the atoms. Bragg diffraction happens when the wavelength of the

incident electromagnetic radiation is comparable to the inter-atomic distances in the crystalline sample, acting as diffractive centres. The constructive interference between the reflected radiation results in Bragg peaks, to each a set of Miller indices *hkl* corresponds. Bragg's law can be found in Equation 2.1.

$$n\lambda = 2d_{hkl}sin(\theta) \tag{2.1}$$

where n is an integer, λ is the wavelength, $2d_{hkl}$ is the distance between planes with Miller indices *hkl* and θ is the angle of incidence of the X-ray in relation with the atomic plane. Our XRD measurements were performed on a Rigaku SmartLab diffractometer, at IFIMUP-IN.

2.2.3 Superconducting quantum interference device

Superconducting quantum interference device (SQUID) is a very sensitive magnetometer based on superconducting loops. This device features a superconducting magnet in a helium bath, that applies a magnetic field up to 5.5 T, and a magnet control system that allows for accurate magnetization measurements in the 5 - 380 K temperature range. There are two types of SQUID, the radio frequency (RF) SQUID and the direct current (DC) SQUID having one Josephson junction, and two or more, respectively. A Josephson junction is made by sandwiching a thin layer of a nonsuperconducting material between two layers of superconducting material, which allow quantum tunnelling effect to occur. This effect is influenced by magnetic fields in its vicinity, which enables the Josephson junction to be used in devices that measure extremely weak magnetic fields. The SQUID used in this work is from Quantum Design at IFIMUP-IN.

2.2.4 Magneto optic Kerr Effect

Magneto-optic Kerr effect (MOKE) describes the change of the polarization states of light when reflected at a magnetic material. Three different configurations are depicted in Fig.2.8. In the polar configuration, the magnetization lies perpendicularly to the sample surface, as seen in Fig. 2.8a. In Fig. 2.8b the longitudinal Kerr effect configurations are illustrated, where the magnetization lies parallel to the sample surface and to the plane of incidence. The transversal configuration is characterized by the magnetization parallel to the sample surface while perpendicular to the plane of incidence, as shown in Fig. 2.8c.

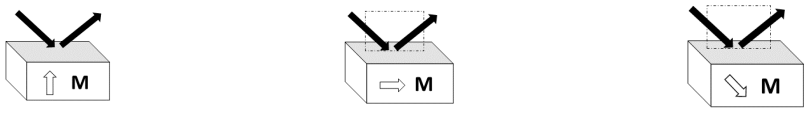

(A) Polar configuration. (B) Longitudinal configuration. (C) Transversal configuration.

FIGURE 2.8: Possible configurations for Moke.

2.2.5 Vibrating Sample Magnetometer

Vibrating sample magnetometer (VSM) is a device used for magnetic characterization. The sample is magnetized under an uniform magentic field and then sinosoidally vibrated, normally with the help of a piezoelectric material. This vibration will lead to a change in the magnetic field which induces an electrical field in a coil based on Faraday's Law of Induction, as is schematized in Figure 2.9.

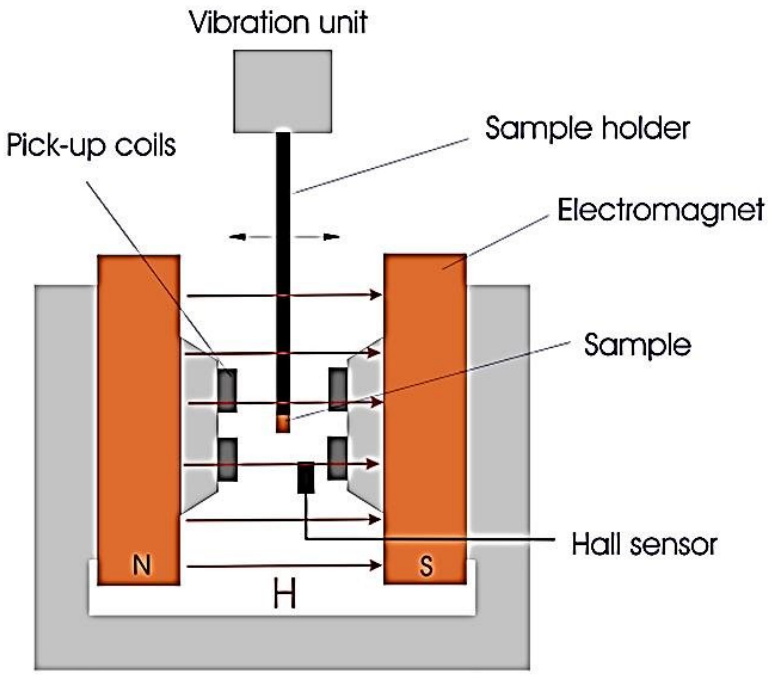

FIGURE 2.9: Schematic configuration of VSM from [69].

2.2.6 Ferromagnetic Ressonance

Ferromagnetic ressonance (FMR) is a technique that, by detecting the precessional motion of the magnetization in ferromagnetic/ferrimagnetic samples, measures its magnetic properties. The damped motion of a magnetic moment about the direction of an external

magnetic field is described by the Landau-Lifshitz-Gilbert equation

$$\frac{d\vec{M}}{dt} = -\mu_0\gamma(\vec{M} \times \vec{H}_{eff}) + \frac{\alpha}{M_s}(\vec{M} \times \frac{d\vec{M}}{dt}) \tag{2.2}$$

where M is the magnetization, M_s the saturaton magnetization, H_{eff} the effective field, α is the dimensionless Gilbert damping parameter that describes a viscous-like damping proportional to the "velocity" of the magnetization, and $\gamma = -\mu_B g/\hbar$ (with $g = 2$) is the gyromagnetic ratio. An external magnetic field applied on the sample will induce Zeeman splitting of the energy levels and a radio frequency magnetic field, in the perpendicular direction to the external field, is used to probe the magnitude of the splitting. The magnetization processes around the external field H at the Larmor frequency ($\omega_0 = \gamma H$) and the resonance occurs when the frequency of the perpendicular RF field is equal to ω_0.

The system used is composed of a vector network analyser (VNA), a coplanar waveguide (CPW), where the sample is to be set that excites it with an electromagnetic signal from the VNA and an electromagnet, that subjects the sample to a static magnetic field. The VNA measures the ratio between the input and output signals, S_{21}, which is a complex number. The CPW's transverse RF applied field varies its frequency over time for different uniform field values. Each uniform field value would lead to the material absorbing a different frequency, due to the different Zeeman splitting.

Chapter 3

Magnetic nanodiscs

In this Chapter, the structural, morphological and magnetic characterization of the discs is presented.

3.1 Discs grown in templates defined by interference lithography

3.1.1 Morphological and Structural Characterization

3.1.1.1 Scanning Electron Microscope (SEM)

The discs fabricated, as reported in subsection 2.1.1, were imaged with recourse to a SEM.

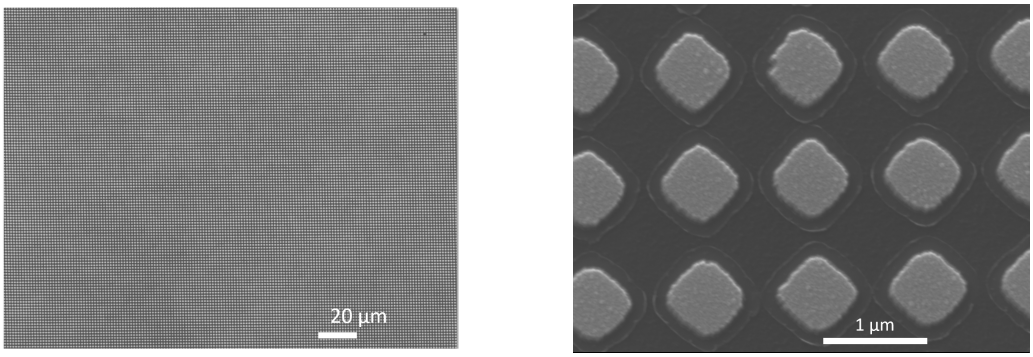

(A) Ampliation of 12000×. (B) Ampliation of 27000×.

FIGURE 3.1: SEM images of the thermally evaporated discs.

Two of these images can be seen in Figures 3.1 and 3.2, revealing how the discs' shape is not an ideal circle, instead of being more like a lozenge, with two different axis sizes. This is to be expected due to the nature of the discs fabrication, namely the interference lithography discussed in subsubsection 2.1.1.1.

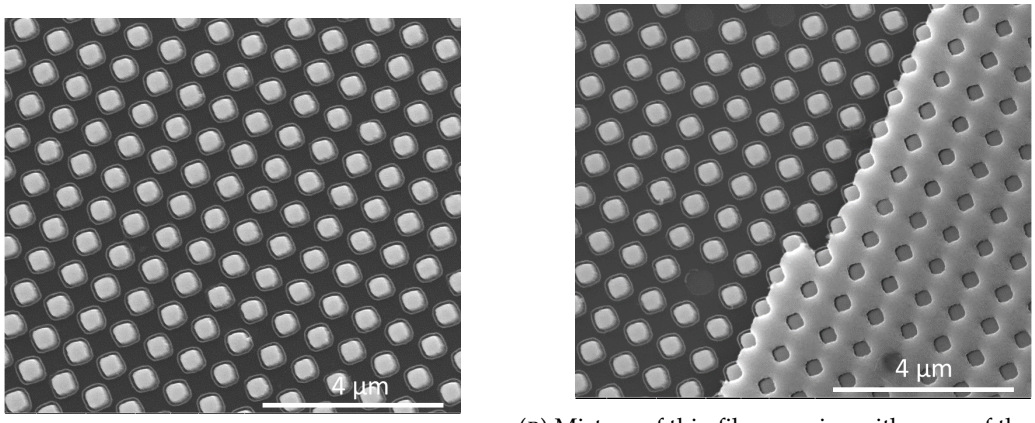

(A) Region with only uncovered discs.

(B) Misture of thin film remains with some of the discs revealed.

FIGURE 3.2: SEM images of the ion beam deposited discs.

The lift off of the thermally evaporated discs was done using an already optimized process, which lead to a complete removal of the photoresist and deposited metal layer. Areas of 2×2 cm^2 of homogeneous discs were obtained, as shown in Figure 3.1a. The lift off of the ion beam deposited samples, however, was tried using an acetone bath with ultrasounds. As can be seen in Figure 3.2, not all of the thin film was removed in the latter case. In fact, most of the photoresist and thin film were observed to remain intact, having only a few areas of uncovered discs. This has been considered to be because of the ageing and heating (during the ion beam deposition), of the photoresist that could have dried it, making it harder to remove. This misstep is sure to affect the magnetic characterization of said samples.

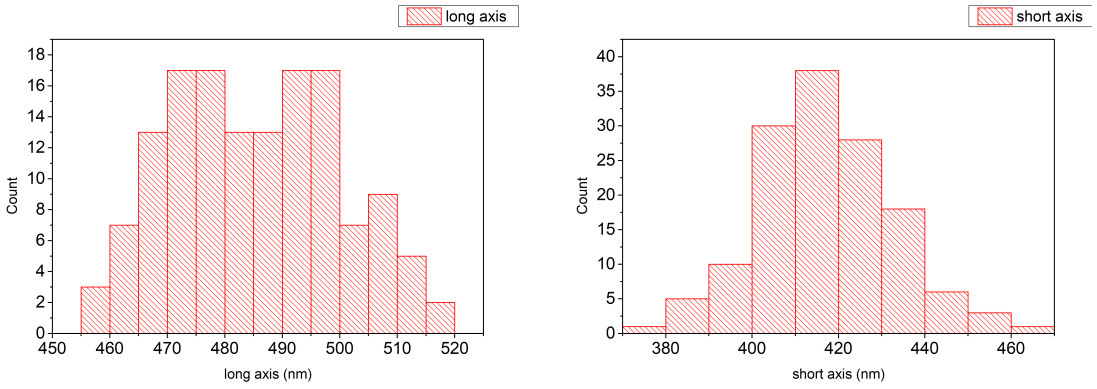

(A) Short axis' histogram

(B) Long axis' histogram

FIGURE 3.3: Histogram analysis discs' dimensions in the patterned substrate.

The size distribution inherent to interference lithography was also taken into account, and histograms, relative to each of the main axis of the discs, were made with the help

of an image analysis software, ImageJ [70]. These histograms are presented in Figure 3.3. The average sizes for the long-axis and short-axis were $\overline{x} = 485,51$ nm and $\overline{y} = 416,37$ nm, respectively with $\sigma_x = 15,43$ nm and $\sigma_x = 14,57$ nm. From this section forward, the discs are regarded as having the average dimensions, for simplicity sake.

3.1.1.2 X-ray diffraction (XRD)

A $\theta - 2\theta$ X-ray diffraction analysis was performed on the samples for a structural characterization. The scans and analysis are presented in Figure 3.4. and lets us confirm the presence of Al, Au and Fe, as well as inferring that the Fe structure is a body-centred cubic (BCC) with preferential growth in the (110) direction. This last information is useful for more accurate simulations used in Chapter 4, as it allows us to understand along which crystallographic directions it is easier to magnetize (easy or hard axis) and so define the anisotropy.

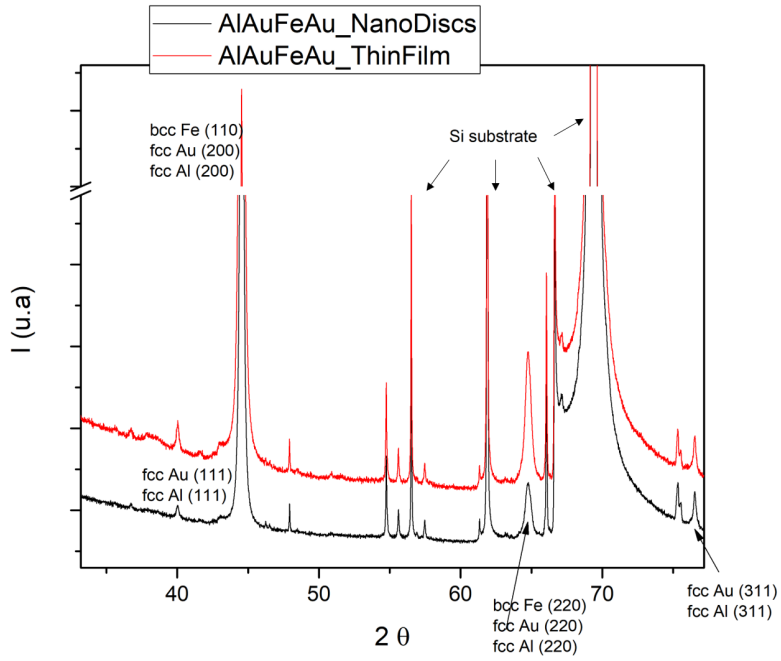

FIGURE 3.4: X-ray diffraction analysis.

The identified peaks were the same for the thin film and the patterned samples. The peaks attributed to Fe are overlapped with those of Au and Al, which hinders the quantitative analysis and makes the determination of the grain size impossible. Some of the peaks present in Figure 3.4 were, however, not identified, which could have been a red herring to the possibility of the inhomogeneity of the samples, due to the presence of iron

oxides or other contaminations from the evaporation, to be discussed in the following section.

3.1.2 Magnetic characterization

For magnetic characterization, SQUID, MOKE and FMR were the chosen techniques.

3.1.3 SQUID

The numbering in the thermal evaporation set-up (Figure 2.2a, section 2.1.1) served the purpose of identifying the samples' position during said evaporation, to evaluate the uniformity of the process. Each of the numbered square samples was cut into four parts, leading the samples to be designated by 3 numbers in the hysteresis loops to be presented. Two measurements were performed for each sample, differing only the direction of the applied magnetic field, one being parallel and the other perpendicular to the sample plane. The samples hysteresis loops were of the form represented in Figure 3.5. This behaviour is due to the big contribution of the Silicon substrate whose thickness many times exceeded that of the active sample. With this in mind, the linear parts of the graph were fitted and the diamagnetic contribution of the Silicon was then subtracted from the real behaviour of our active sample.

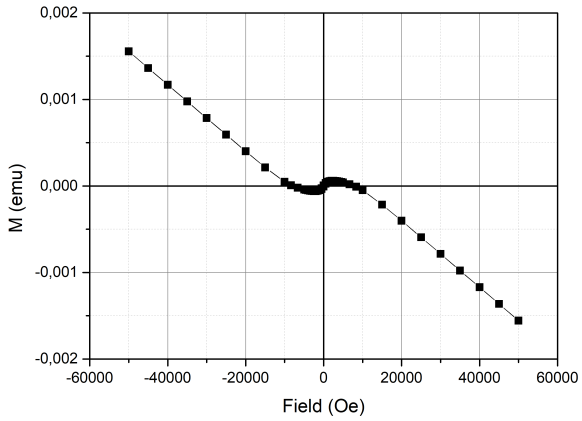

FIGURE 3.5: Sample 124, parallel direction

In Figure 3.6 it is first shown the hysteresis loops obtained for the thin film that accompanied the deposition, for reference. Figure 3.6a reflects the behaviour of a thin film of a soft ferromagnetic material, as expected, while Figure 3.6b, does not [71]. Although needing a much higher saturation field when compared with the easy axis, the narrowing

of the loop when approaching zero-field was not in agreement with the typical behaviour of a soft ferromagnetic material, seen in the literature [72].

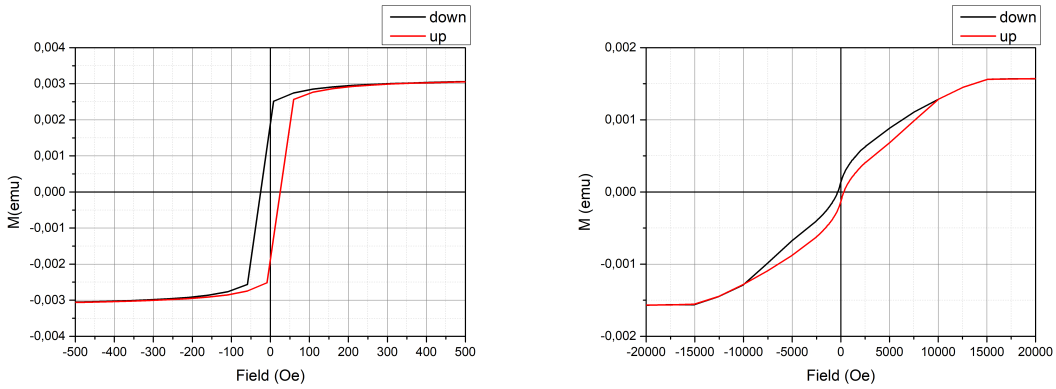

(A) Parallel to the thin film surface. (B) Perpendicular to the thin film surface.

FIGURE 3.6: SQUID measurements for the thin film.

The nanodiscs' hysteresis loops are present in Figures 3.7 and 3.8. Here, two samples were chosen from distant sides of the set-up to better understand the uniformity of the samples prepared by thermal evaporation. The behaviour of the samples under parallel and perpendicular applied magnetic field is different but not entirely as expected, for nanodiscs with D= 500 nm and t=50 nm (see section 4.1). Figures 3.7b and 3.8b are almost exactly equal, having both a high saturation field of almost 2T and also showing the same broad behaviour. They only differ in the coercive field, H_c and remanent magnetization, M_{rem}, as is summarized in table 3.1.

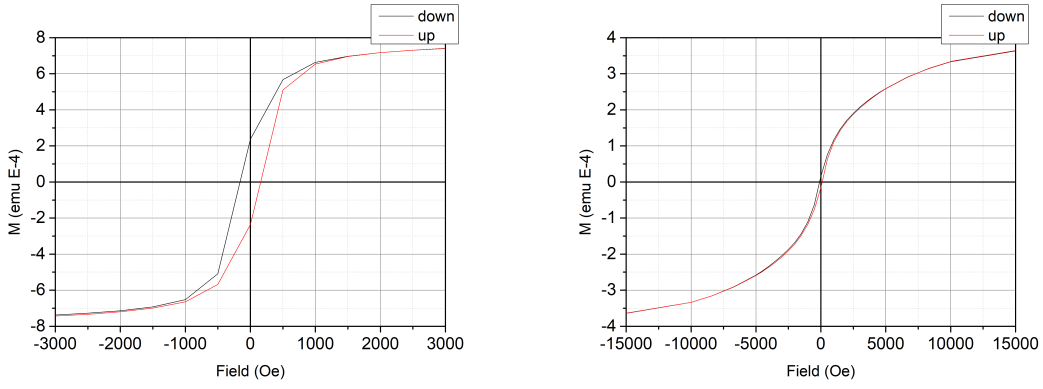

(A) Parallel direction (B) Perpendicular direction

FIGURE 3.7: SQUID measurements for the sample 111, for the parallel and perpendicular direction.

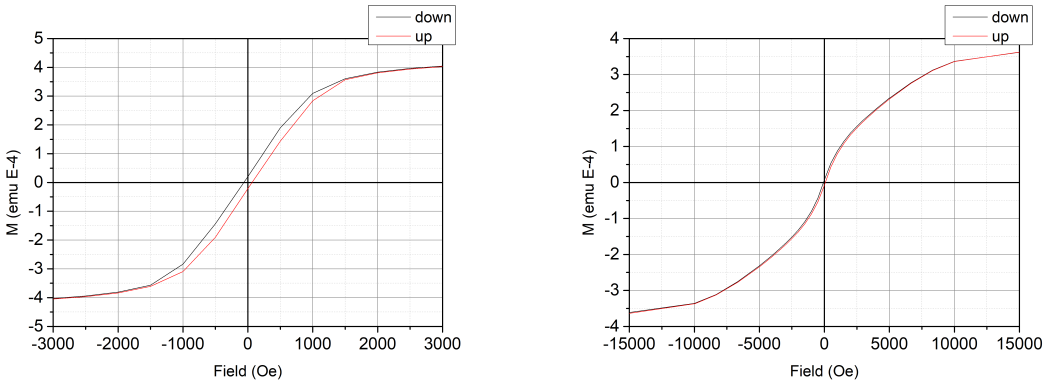

(A) Sample 124, parallel direction

(B) Sample 124, perpendicular direction

FIGURE 3.8: SQUID measurements for the sample 124, for the parallel and perpendicular direction.

Figures 3.7a and 3.8a do not show the typical vortex behaviour it would be expected from the in-plane applied magnetic field. Instead, these hysteresis loops are characterized by having a small coercivity and remanence magnetization different than zero, with their characteristic fields also summarized in table 3.1.

	M_{sat} **(emu)**	H_c **(Oe)**	M_{rem} **(emu)**	H_{Sat} **(Oe)**
111 par	6.2×10^{-4}	75	2×10^{-5}	2000
124 par	4×10^{-4}	65	2.1×10^{-5}	3000
111 per	4×10^{-4}	100	1.6×10^{-5}	20000
124 per	4×10^{-4}	75	7.5×10^{-6}	20000

TABLE 3.1: Characteristic fields of the hysteresis loops measured by SQUID.

From Figures 3.7, 3.8 and table 3.1, it can be seen that the samples 111 and 124 have different behaviours, especially in the parallel direction, which suggests a lack of homogeneity of the deposition. With the vortex-state typical behaviour lacking from the measurements, three different possibilities were thought out: the massive Silicon substrate was hindering, or hiding, the results; the thermal evaporation's lack of uniformity was too much; a combination of the effects that the discs' dimensions (aspect ratio) and the inter-dot distance have did not allow for a vortex state to form.

MOKE measurements were purposed, as the contribution of the substrate would be decreased and also a higher degree of localization could be acquired.

3.1.3.1 MOKE on the thermally evaporated samples

MOKE measurements of the samples 111 and 121 are showed in Figure 3.9. There are clear differences between Figures 3.9a and 3.9b, as one shows a clear vortex-like hysteresis

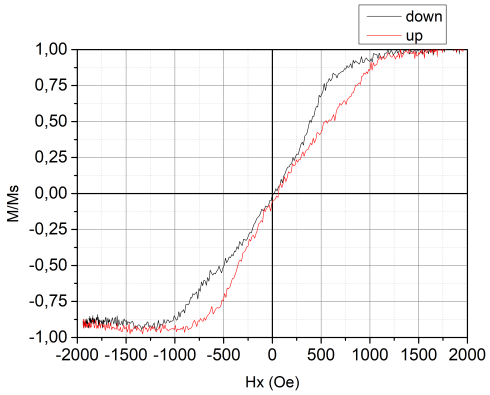

(A) Sample 111

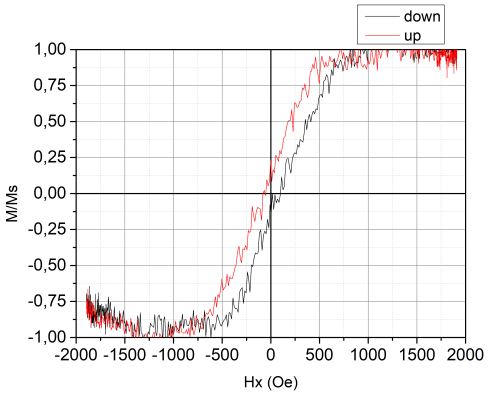

(B) Sample 121

FIGURE 3.9: MOKE measurements.

loop and the other seems similar to what would be expected of a soft ferromagnetic thin film. This confirms the supposition of the non-uniformity of our samples and also puts MOKE as a good choice for this kind of surface-sensitive magnetic characterization. In the regions where the vortex state was found, the vortex characteristic fields were H_n=650 Oe and H_a=1206 Oe.

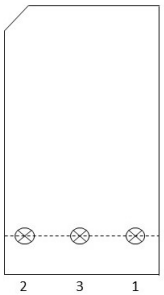

(A) Moke measurements' positions on sample 121.

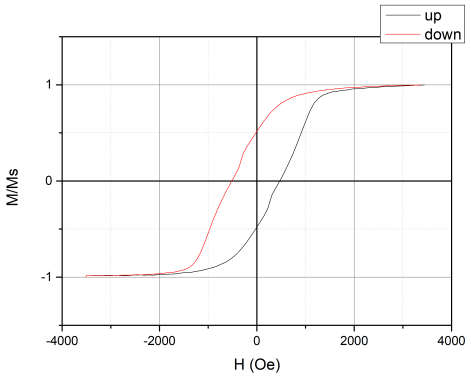

(B) First position.

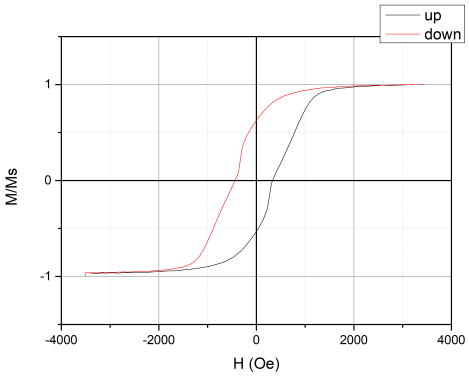

(C) Second position.

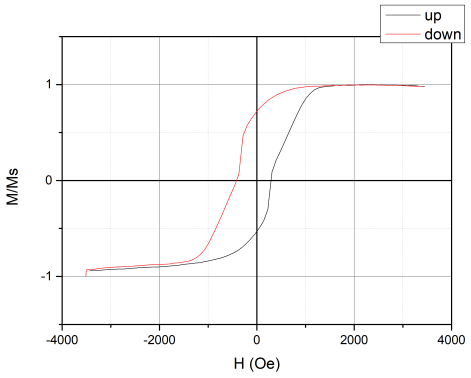

(D) Third position.

FIGURE 3.10: MOKE measurements in different positions.

Still, about the non-uniformity, the same sample (121) was measured in 3 different positions, as shown in Figure 3.10a. The measurements can be found in 3.10. Once again, Figure 3.10b shows a vortex state expected from a typical ferromagnetic material nanostructured with these dimensions, with non-zero remanence and coercivity but the Figures 3.10c and 3.10d, despite also having these characteristic values different than zero, appear to demonstrate some narrowing of the hysteresis loops akin of a light version of the transitions expected from the vortex state. This might imply that some portion of the sample, not all, is in the vortex state, which again supports the assumption of non-uniformity but raises the question to what caused it, since the measurements were too close together for the thermal evaporation's inherent lack of uniformity to be the cause. FMR measurements were then envisioned to assess these possibilities.

3.1.3.2 Ferromagnetic ressonance (FMR)

FMR measurements were performed on the nanodiscs, obtained by thermal evaporation, but nothing could be observed, probably due to the low signal. Thus the thin film was analysed instead. The result can be seen in Figure 3.11a where the shape (broadening) of the line suggests that the sample was, at least, partly oxidized. For each field and frequency, the colour gives a measure of peak intensity. As Figure 3.11a shows a larger darker region, it means that there are a lot of different peaks superimposing and resulting in a larger, broader peak. This is what would be expected of an inhomogeneous sample [73, 74] and is even more evident when in comparison with 3.11b, which is the FMR measurement of a 60 nm thin film of Fe deposited using an IBD. In the latter, the darker region is a better-defined line, characteristic of a homogeneous thin film.

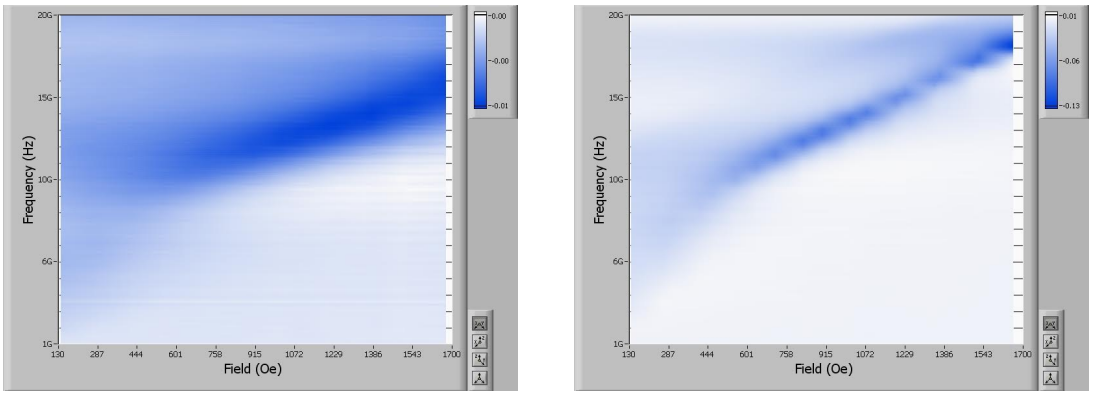

(A) Thin film (50 nm) deposited in thermal evaporator. (B) Thin film (60 nm) deposited in IBD.

FIGURE 3.11: FMR measurement of both thin films.

$$f = \gamma\sqrt{H(H + M_s)} \tag{3.1}$$

In Figure 3.12, each point represents a peak in the FMR spectra, so an even more graphical comparison between the two results and the theoretical prevision is presented. This prediction uses the Kittel formula (equation 3.1) and bulk values of Fe, for γ=2.96×10^6 (gyromagnetic ratio) and M_s=1752 A/m.

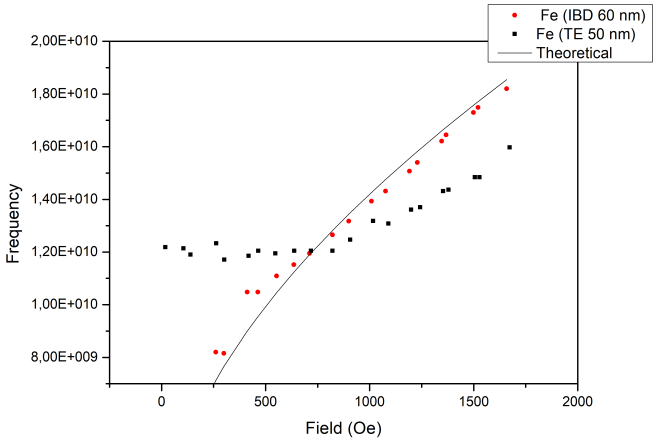

FIGURE 3.12: Comparisson between the two experimental values and the theoretical prediction.

The theoretical line is in agreement with the values for the IBD film. The values fo the thermally evaporated thin film, however, do not follow the theoretical line behaviour. The conclusions taken from the FMR analysis are that the thermally evaporated samples consist of contaminated and/or partly oxidized Fe probably due to the lower vacuum offered by the evaporation set-up, when compared with the IBD. The latter seems now a good option to follow as the higher vacuum and lower deposition rates improve the quality and uniformity of the films.

3.1.3.3 MOKE on the ion beam deposited samples

MOKE measurements were performed on the later ion beam deposited samples. Figure 3.13 shows two hysteresis loops for different thickness samples of 30 and 70 nm, respectively. In Figure 3.13a, it is shown a square hysteresis loop, similar to the observed in the thin film sample (section 3.1.3.1). This can be attributed to the fact that there still persists thin film mixed with the discs, where the discs contribution is negligible. It is not possible to know the regions where the lift-off was successful to perform the moke measurements.

This region was probably unaffected from the lift-off. However, as for Figure 3.13b, this shape is somewhat different, there is a decrease in M_s probably because it caught a region where the lift-off successfully removed some of the thin film, but not all.

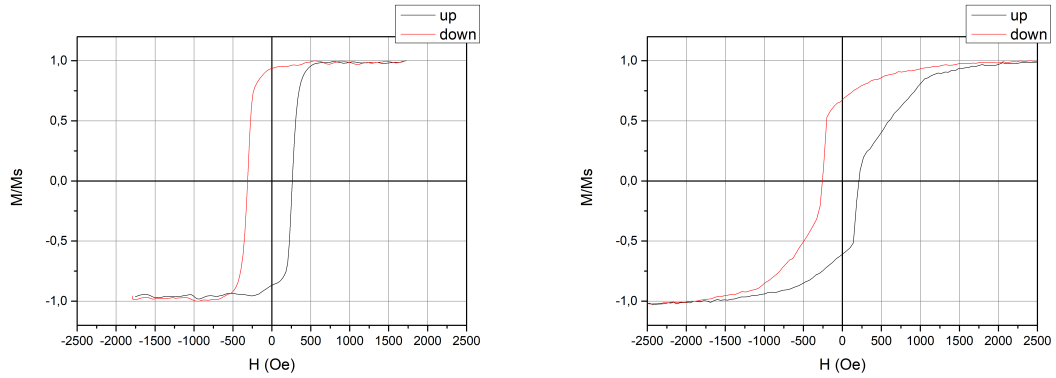

(A) 30 nm. (B) 70 nm.

FIGURE 3.13: Hysteresis loops for ion beam deposited samples, with different thickness.

As discussed earlier in section 3.1.1.1, the lift-off was not entirely successful, but MOKE being a very locally sensitive technique, it would be possible to get different hysteresis loops even within the same sample. The fact that there still persists thin film mixed with the discs is going to affect the measurements. The lift-off process ought to be optimized for a more clear analysis and magnetic characterization of these samples.

3.2 Discs in Porous alumina templates

Porous anodic alumina templates (PAAT) were fabricated using the method described in section 2.1.2.1. In Figure 3.14 the anodization curves of one sample are showned.

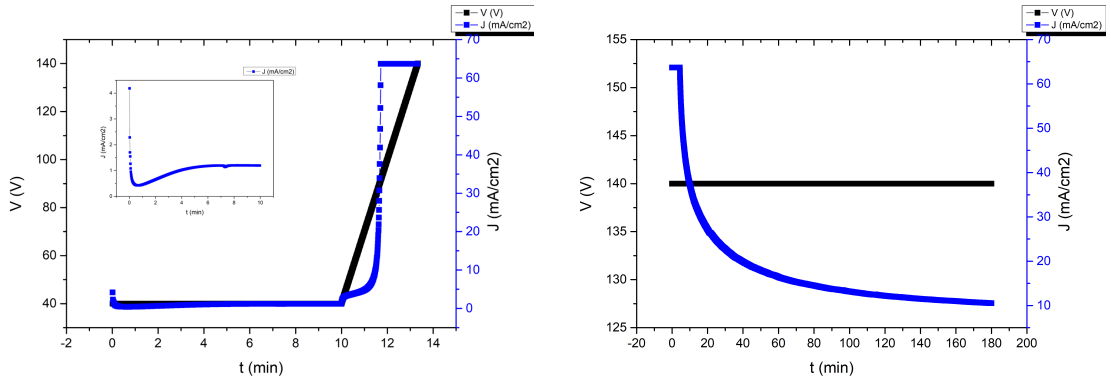

(A) Pre-anodization. (B) Anodization.

FIGURE 3.14: Anodization curves.

Figure 3.14a shows the mild anodization done at 40 V to form a protective layer and the linear increase in the transition between the mild and hard anodization voltages. It can be seen the normal behaviour of an anodization curve. As soon as the voltage starts to be applied, an oxide layer barrier starts to grow, lowering drastically the current density. Following this, pore nucleation, and further growth takes place. The current density then stabilizes corresponding to the continuous growth of the PAA layer (Figure 3.14a). The values of the current density, j, go from 1.2 mA/cm^2 to 63,7 mA/cm^2, both typical values for the respective mild and hard anodization. The hard anodization was performed for three hours, to obtain templates with 150 μm of thickness. In the hard anodization curve, Figure 3.14b, the current density is initially saturated, meaning that the oxide layer in the bottom of the pores is not proportional to the anodization potential but is thick enough to prevent breakdown. There is a decrease in the current density, without saturating. This means that the oxide layer is always growing without reaching a constant anodization rate.

3.2.1 Morphological Characterization

SEM images of the PAA templates were taken, before the pore widening (Figure 3.15) and after the electrodeposition, 3.16. Images of the top and bottom of the PAA templates are shown in Figure 3.15. The small diameter of the pores on the top surface of the PAA (Figure 3.15a) is a result of the 5 minutes of mild anodization (pre-anodization) performed. Nanopores with approximately 35 nm in diameter and 105 nm in interpore distance were observed, as expected for mild anodization at 40V [39, 65, 75].

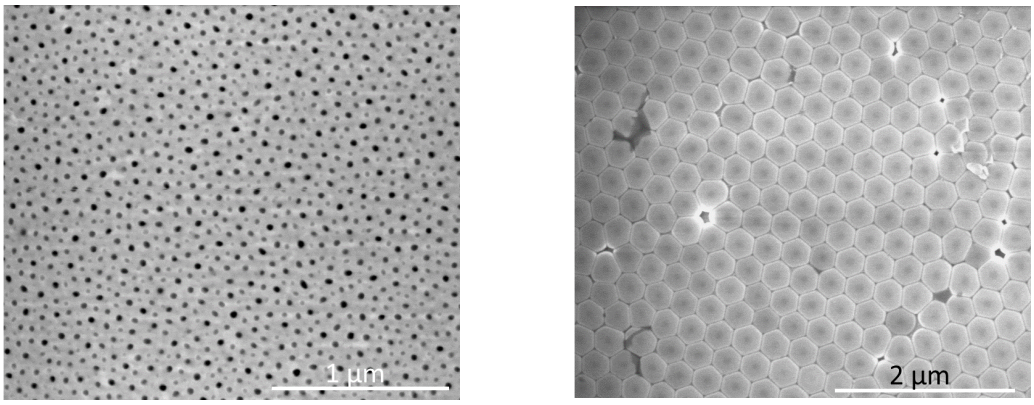

(A) Top surface of the PAA template. (B) Bottom surface of the PAA template.

FIGURE 3.15: SEM images of the PAA templates after hard anodization.

After applying 140 V for the hard anodization process, the neighbouring pores will collapse into each other, resulting in the larger pores seen in the bottom (Figure 3.15b). Nanopores with 60 nm in diameter and 300 nm in interpore distance were observed, consistent with what was reported in the literature [38].

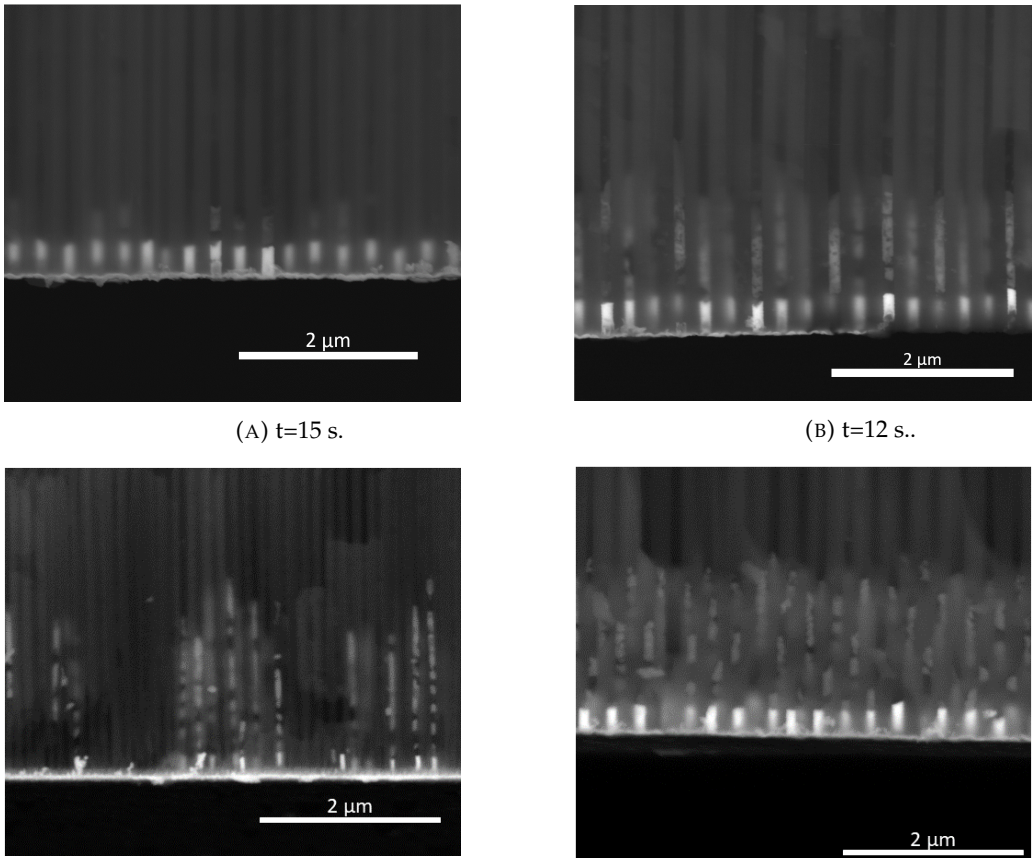

(A) t=15 s.

(B) t=12 s..

(C) t=9 s.

(D) t=6 s.

FIGURE 3.16: SEM images for the four electrodeposited samples, with different Fe deposition times.

Four samples were used for electrodeposition, with different deposition times for the iron layers, t= 6, 9, 12, 15 seconds. The respective SEM images are shown in Figure 3.16. Using these images we were able to measure the pore diameter, after the widening process, to be D_p=110 nm. These cross-sectional images also show the high homogeneity of the PAA template with pores perfectly parallel to each other. We were unable to measure the length of the segmented wires due to poor contrast between Cu and Fe. The clearer parts in the interior of the PAA's pores correspond to the NWs. The bottom of the pores is filled with Au segments that present in every sample. The Fe and Cu segments are more difficult to distinguish given the proximity in electronic density. For the samples with t_{Fe} = 15 and t_{Fe} = 12 s it is really difficult to observe the segments of the wanted materials.

For the samples with t_{Fe} = 9 and t_{Fe} = 6 s it is possible to observe some segments with different contrast, the darker ones corresponding to Fe and the brighter ones to Cu.

The electrodeposition curves, corresponding to the four samples, follow in Figure 3.17. With this data, we were able to fill in table 3.2 and determine the expected length of the nanowires segments. The area of the sample was A=$(0.5)^2 \times \pi$ cm^2 but the effective area that counts towards electrodeposition depends on the porosity of the sample. With the voltage used, the porosity was 3% [38], which gives A_{eff}=0.023562 cm^2. The average current density and the total charge were then calculated for each of the metals, from the electrodeposition curves in Figure 3.17.

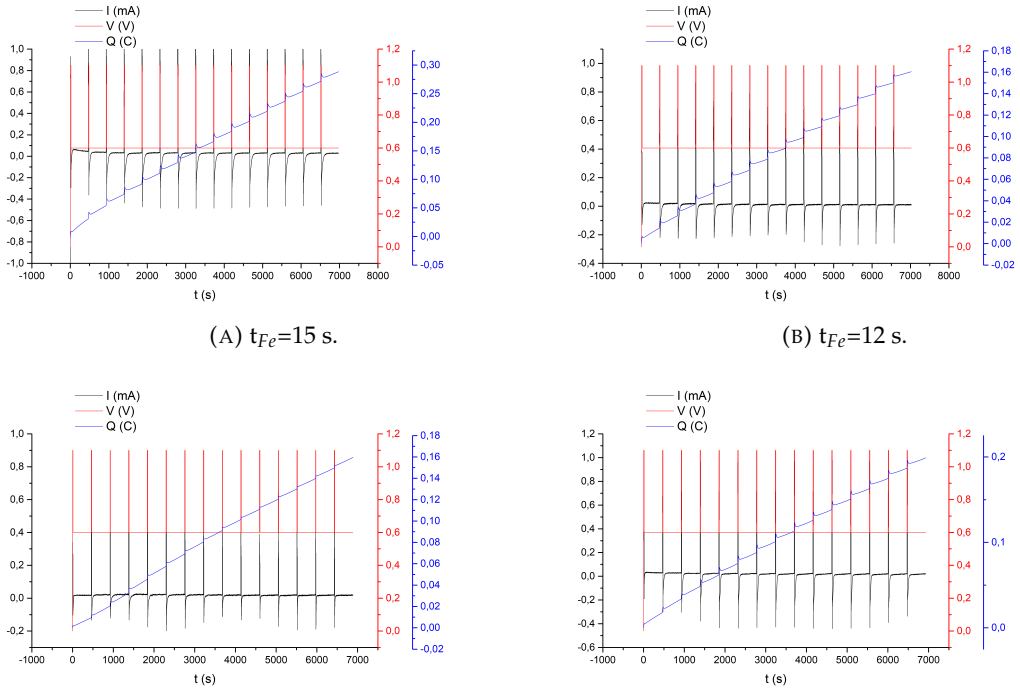

(A) t_{Fe}=15 s. (B) t_{Fe}=12 s.

(C) t_{Fe}=9 s. (D) t_{Fe}=6 s.

FIGURE 3.17: Electrodeposition curves for the four electrodeposited samples, with different Fe deposition times.

Using $\int_0^t Idt = zeN_A \frac{m}{M}$, the deposited mass was calculated. Here z is the valence electrons, e the charge, N_A the Avogadro number, M the molar mass and m the deposited mass. After calculating m, the path was free to reach the segments' length. The number of pores was achieved by dividing the effective area by the individual pore area. Assuming the wires are cylinders, the lengths can be estimated. The results are summarized in table 3.2. The expected Fe lengths, obtained through calculations, were 0.19, 0.52, 0.18 and 0.63 nm, for the deposition time of 6, 9, 12, and 15 s, respectively. The thickness of the Fe layers is clearly lower than the expected for these electrodeposition times. This means that the

electrodeposition process needs to be optimized and the electrodeposition rate needs to be calculated for PAA templates obtained by hard anodization with 150 mm in length.

t_{Cu} (s)	t_{Fe} (s)	j_{Cu} (mA/ cm^2)	j_{Fe} (mA/ cm^2)	Q_{Cu} (C)	Q_{Fe} (C)	m_{Cu} (mg)	m_{Fe} (μg)	L_{Cu} (μm)	L_{Fe} (nm)	L_{NWs} (mm)
450	15	0.942	1.16E-2	4.24E-01	1.75E-04	0.279	5.071E-2	13.23799	2.733	0.1986
450	12	0.494	4.04E-3	2.22E-01	4.85E-05	0.146	1.408E-2	6.93857	0.7589	0.1041
450	9	0.399	1.57E-2	1.80E-01	1.41E-04	0.118	4.096E-2	5.60948	2.208	0.08417
450	6	0.790	8.42E-3	3.56E-01	5.05E-05	0.235	1.468E-2	11.11071	0.7914	0.16667

TABLE 3.2: Electrodeposition parameters.

3.2.2 Magnetic characterization

3.2.3 Vibrating sample magnetometer (VSM)

The samples were measured in VSM. A representative hysteresis loop is presented in Figure 3.18, corresponding to the sample with t_{Fe}= 9s. The measurements have considerable

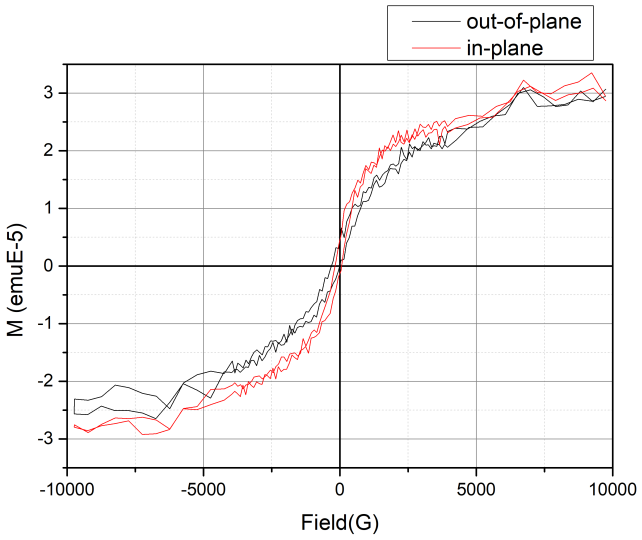

FIGURE 3.18: VSM measurements on the sample with t_{Fe}= 9s.

noise associated with them, which is understandable, given that the layers of Fe are much thinner than those of Cu. The hysteresis loops for the in-plane and out of plane magnetization differ on the apparent saturation field. The in-plane loop seems to approach saturation before its out-of-plane counterpart. The difference is really subtle, but one

thing that can be concluded is that it is not possible to exclude the vortex state from these measurements. The average length of Fe presented in table 3.2, let us infer that instead of layers of Fe, what probably occurred was a nucleation of Fe particles without smoothing out. This would explain the average length of Fe being so low and is the reason why the electrodeposition process has to be optimized to better understand the magnetic characteristics of nanodiscs with dimensions appropriate for the vortex state.

Chapter 4

Micromagnetic Simulations

To better understand and support the experimental results, micromagnetic simulations were carried out. These simulations were performed with MuMax3 software [76]. MuMax3 is a GPU-accelerated micromagnetic simulation program that calculates the space- and time-dependent magnetization dynamics in nano-/micro-sized ferromagnets using a finite-difference discretization. The scripting language resembles a subset of the Go programming language. A web-based HTML 5 user interface is provided, allowing the user to inspect and control the simulations from within a web browser [76].

When writting the scripts, firstly, the magnetic constants were defined. The iron magnetic saturation was defined as $M_{sat,Fe} = 1700 \times 10^3$ (A/m), the exchange stiffness $A_{ex,Fe} = 2.1 \times 10^{-11}$ (J/m) and the magnetocristalline anisotropy used was $K_{c1,Fe} = 4.8E4$ (J/m^3). After X-ray diffraction analysis on the Fe thin film (3.1.1.2), the easy axis orientation was also defined as $K_{c1v_{Fe}}$ =vector$(cos(45 * pi/180), 0, -sin(45 * pi/180))$ and $K_{c2v_{Fe}}$ =vector$(cos(45 * pi/180), 0, sin(45 * pi/180))$. Cell size was chosen to be 5 x 5 x 5 (nm^3), which is smaller than the Fe characteristic length R$_0$=$\frac{\sqrt{A}}{M_s}$ =8.5 nm [77], and the damping parameter was taken as 0.5, to ensure rapid convergence. The geometries used were either thin cylinders (circular discs) or the precise shape of the discs taking into account our SEM images, as will be shown in the following sections. Usually, periodic boundary conditions were set, as in the real sample.

The program starts by issuing a random magnetic state in the desired geometry and taking a snapshot of it, following up by minimizing the energy which results in the fundamental state, also recorded. After this step, the discs are submitted to a magnetic field loop that forces positive and negative saturation, recording the data in a table. At each step, an explicit Runge-Kutta method for advancing the Landau-Lifshitz equation is performed.

RK45, the Dormand-Prince method, offers 5-th order convergence and a 4-th order error estimate used for adaptive time step control [76].

4.1 Experimental discs

The treated SEM images of the discs, seen in Fig 4.1, were used to define the geometry of the scripts. The idea was to replicate as accurately as possible the real sample. The images have two distinct regions, black and white, defined as magnetic and non-magnetic, respectively.

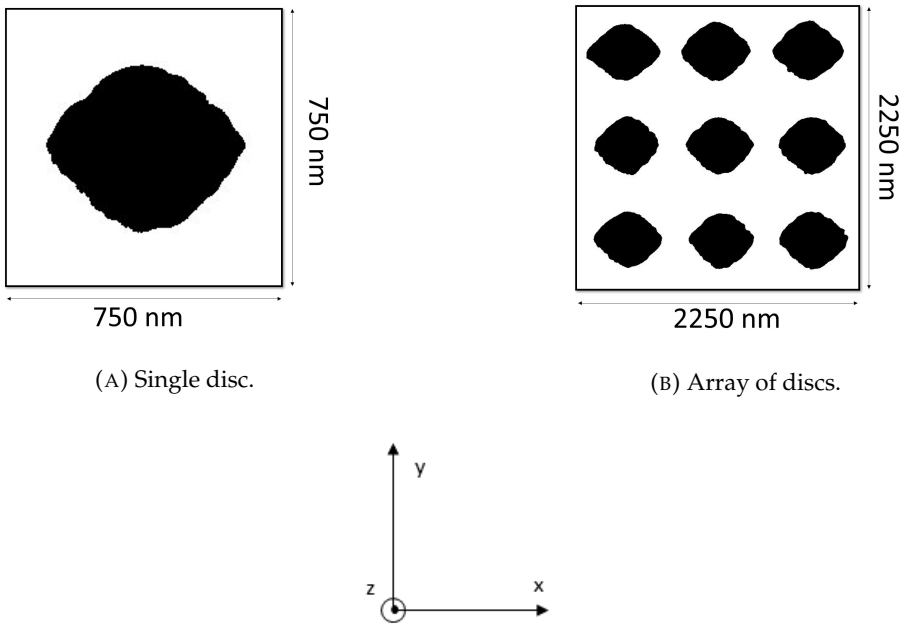

(A) Single disc.

(B) Array of discs.

(C) Direction of the fields.

FIGURE 4.1: SEM images used to define the discs' geometry.

The intrinsic anisotropy of the disc meant it would behave differently, even depending on the direction of the in-plane applied magnetic field. Starting with the single disc, the fields were either applied in the x or y directions and also on the perpendicular, z-axis. This would be easily comparable with the magnetically recorded data in section 3.1.2.

Figure 4.2c shows the behaviour of the magnetization as a function of the applied external magnetic field in the z-direction (B_z) where the high field saturation is observed. This overall shape is in good agreement with the magnetic data, however here a lower value of coercivity is found. The disc at remanence is in the vortex state, but with the increasing field, the magnetic moments almost linearly start to align with the z-direction

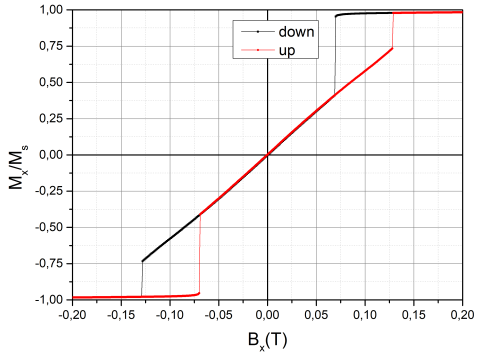

(A) Hysteresis loop in the x-direction.

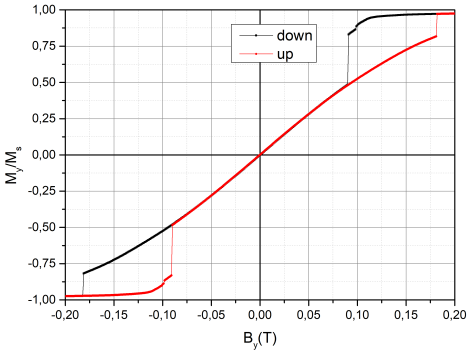

(B) Hysteresis loop in the y-direction.

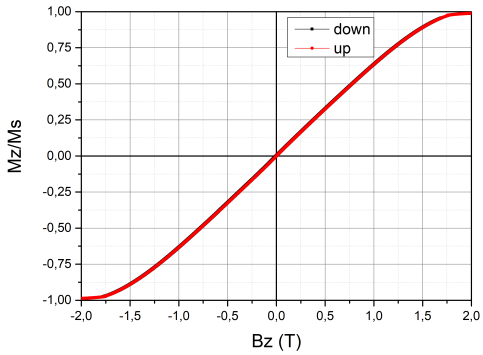

(C) Simulated hysteresis loop for applied filed in the z-axis, for 50 nm of Fe.

FIGURE 4.2: Simulated hysteresis loop for single disc with 50 nm of Fe, for in-plane and out of plane applied magnetic field.

until saturation is reached. In this section, the simulated samples will hereafter be designated, for simplicity sake, by t_direction, for example, 50_z refers to the sample with 50 nm of thickness with an applied field in the z-direction (Figure 4.2c).

The main objective was, however, to study and identify typical vortex characteristics in the hysteresis loops when the applied field was parallel to the disc plane (x- and y-direction). Figure 4.2 illustrates the desired behaviour, as explained in Chapter 1. In both axes, there are two clear, abrupt, transitions, corresponding to the vortex nucleation and annihilation, as well as a linear part on the hysteresis loop, representing the movement of the vortex core. The vortex characteristic fields were H_n=0,0698 T, H_a=0,129 T for the x-direction and H_n=0,1129 T, H_a=0,1718 T for the y-direction. The values obtained from Figure 3.9a (section 3.1.3.1) are closer to the ones obtained from Figure 4.2a. The remanent state can be observed in Figure 4.3 where the expected vortex is apparent. Each colour represents a direction of the magnetic moments.

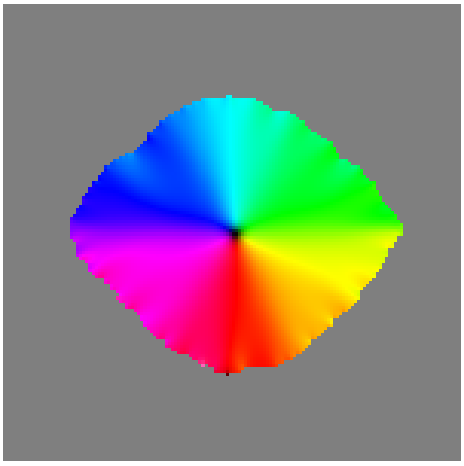

FIGURE 4.3: Simulated image of the remanent state of the Fe disc, with 50 nm.

4.1.1 Thickness

The thickness of the discs was then varied to have a better grasp of the conditions needed for the vortex to nucleate. A vortex state was encountered in remanence between 30 and 90 nm, and between 20 and 90 nm in the x- and y-directions, respectively. The difference noted here can be explained by the discs not being perfectly circular, having one axis, x, bigger than the other one, y (histograms on subsection 3.1.1.1). This leads to a difference in aspect ratio, which, as will be discussed below, is crucial to determine if the sample is or not in the vortex state. The 20_x hysteresis loop also showed two abrupt transitions but did not have zero magnetic moment at remanence. Also the linear, vortex-motion, part of the loop was moved from the origin, as can be observed in Figure 4.4a. This is not in line with the expected vortex behaviour and more closely resembles a typical ferromagnetic state, in agreement with 1.5, from Cowburn *et al.* [17]. Its y-direction counterpart has no remanence, two abrupt transitions near zero and a linear part of the hysteresis loop, thus being in the vortex state.

In some of the thicker discs, the hysteresis loop form even became somewhat distorted, comparing to the ideal vortex-behaviour, as can be seen in Figure 4.5. Here, before the abrupt transitions, there is already some loss in the magnetization. This indicates that the disc was not in the single-spin state anymore but still wasn't a fully-closed flux state either. Possibly the answer lies somewhere in the middle, with an intermediary state, where some magnetic moments begin to deviate from the field direction, appearing until the full vortex could nucleate [20, 21].

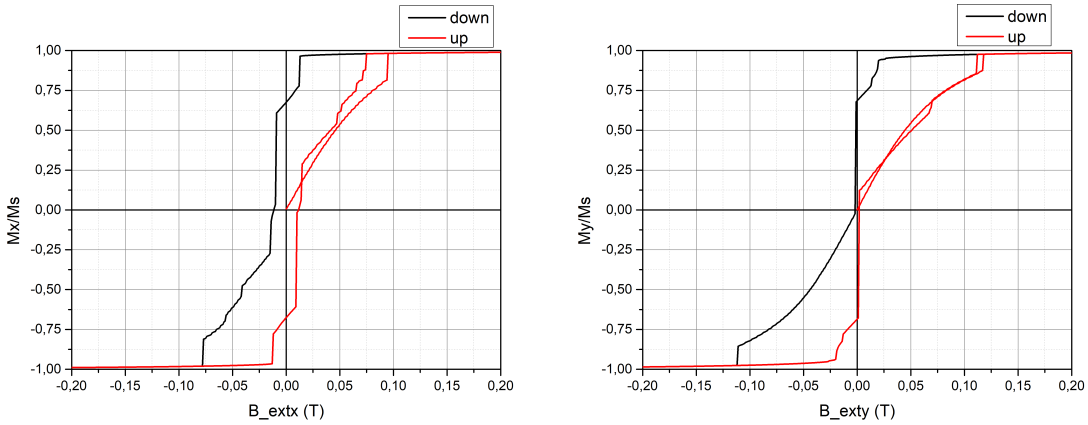

(A) Hysteresis loop in the x-direction. (B) Hysteresis loop in the y-direction.

FIGURE 4.4: Simulation for single disc hysteresis loop for 20 nm of Fe, for in-plane applied magnetic field.

4.1.2 Inter-dot interctions

The difference between the single disc and the disc array simulations, with periodic boundary conditions (PBC), were negligible. This supports the assumption that the inter-dot distances used in our samples (250 nm) did not play a significant role, and also meant that more often than not, the single disc image was the one used for the simulations.

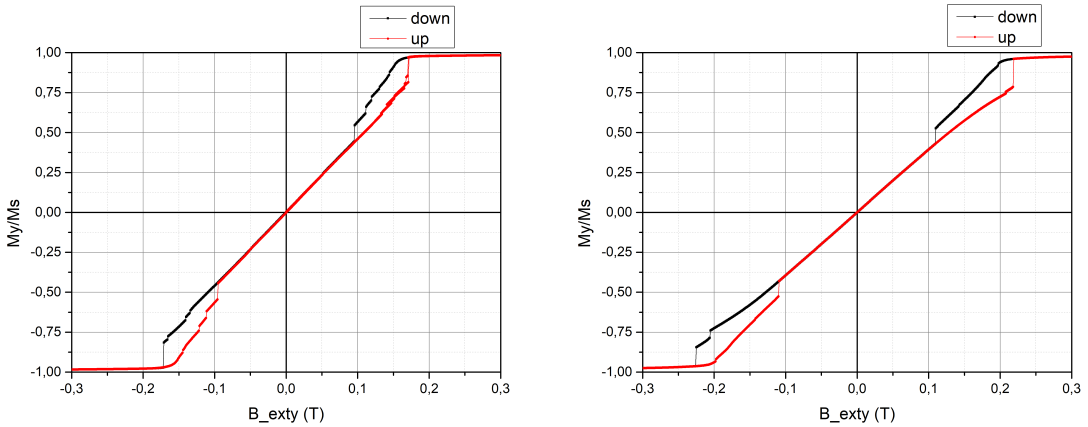

(A) Hysteresis loop in the x-direction. (B) Hysteresis loop in the y-direction.

FIGURE 4.5: Simulation for single disc hysteresis loop for 80 nm of Fe, for in-plane applied magnetic field.

Figure 4.6 shows snapshots at six different applied fields in an array of nine discs, without periodic boundary conditions, to demonstrate the nucleation process.

Starting off, all of the discs are in the saturated state (Figure 4.6a). As the field starts to reduce, some inhomogeneities begin to make an appearance at one of the discs in the outer rows (Figure 4.6b). This can be explained since no periodic boundary conditions are

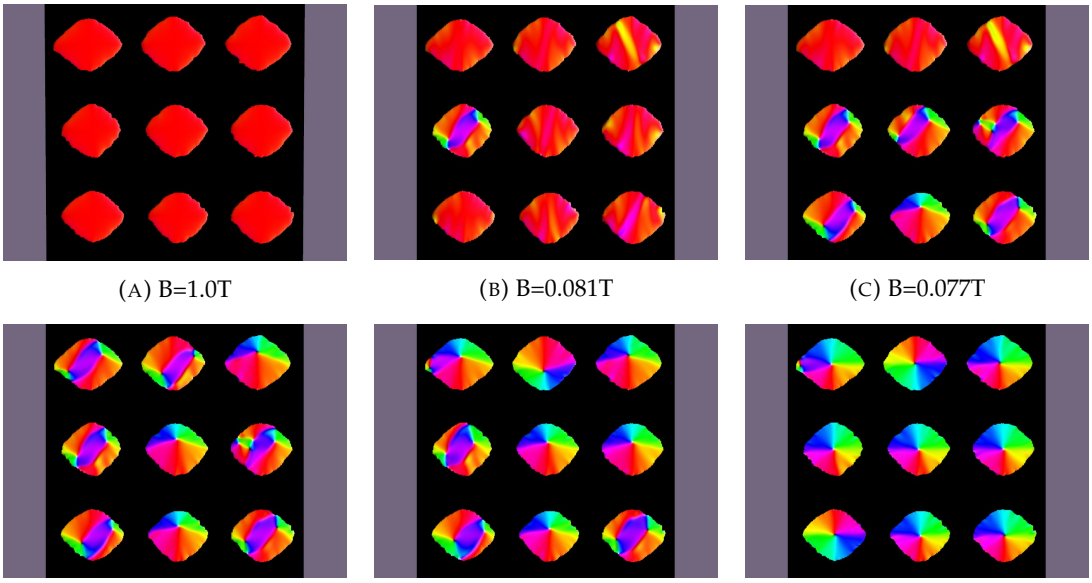

(A) B=1.0T (B) B=0.081T (C) B=0.077T

(D) B=0.067T (E) B=0.056T (F) B=0.011T

FIGURE 4.6: Field evolution of an array of 50 nm thickness Fe discs, without PBC

implemented, therefore the outer discs are the ones are less affected by their neighbours. Between Figure 4.6c and Figure 4.6d, all of the disc have already started to nucleate. It is noted that this transition is not as abrupt as presumed, revealing the more probabilistic nature of the event [28]. Even in Figure 4.6e, some inhomogeneities can be found, before the final image (Figure 4.6e) where the vortex is present in all of the discs and nearly centred. This images can correspond to the hysteresis loop in Figure4.2a.

4.1.3 Vortex characteristic fields

The vortex nucleation and annihilation fields are plotted against the thickness, for each of direction, in Figure 4.7. Here, even the 20_x, 90_x and 90_y's transitions were considered, as they show the upper and lower limits to the desired behaviour.

With the increase in thickness comes an increase in E_{demag} (Eq. 1.3), which means that the demagnetizing fields within each particle need higher externally applied fields to be counterbalanced [20], thus a magnetic vortex nucleates at higher fields. This also means that the discs will require more energy to expel the vortex which leads to an increase in the annihilation field. As the thickness continues to increase, other magnetic states start to appear.

The thickness is not the only parameter that influences the results, the diameter of the disc is the other key parameter. Thus, the vortex characteristic fields are plotted with respect to the aspect ratio, $r = D/t$, in Figure 4.8. As the aspect ratio increases, a non-linear

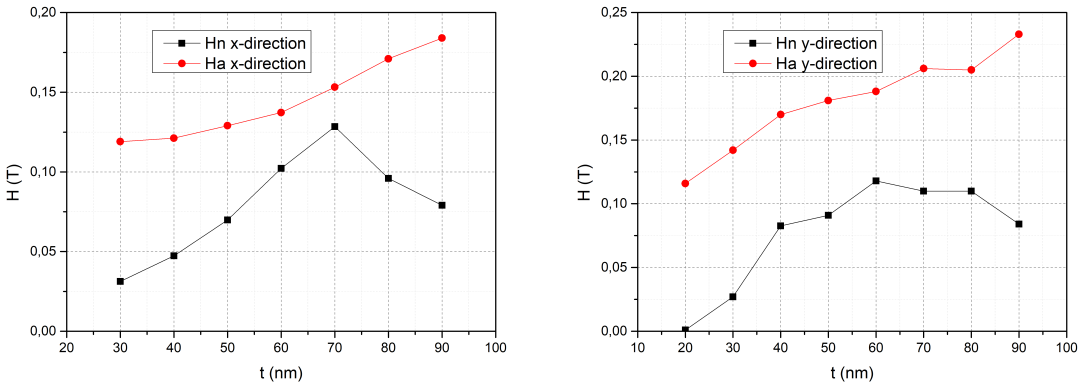

(A) x-direction. (B) y-direction.

FIGURE 4.7: Nucleation and Anihilation fields for different thickness.

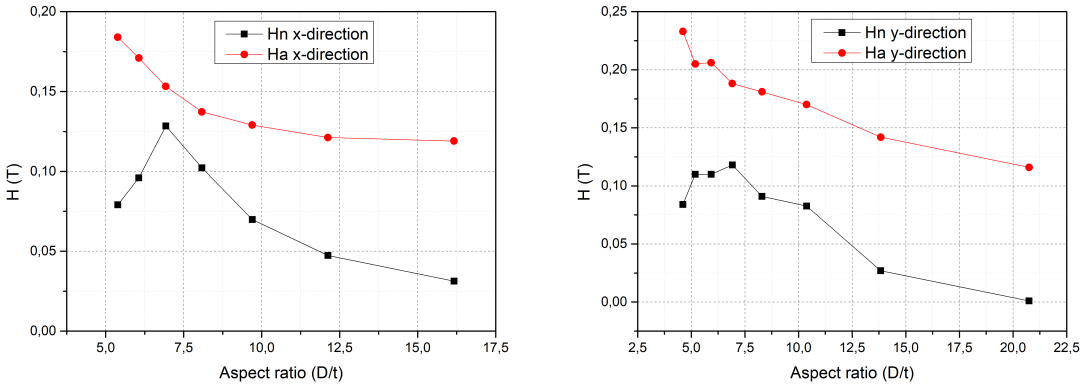

(A) x-direction. (B) y-direction.

FIGURE 4.8: Nucleation and Anihilation fields for different aspect ratios, D/t.

decrease is observed in both vortex nucleation and annihilation fields, in agreement with the standard behaviour reported in Schneider *et al.* [21]. This behaviour can be explained, once more, by looking at the competition between the demagnetizing energy (Eq. 1.3) and the exchange energy (Eq. 1.4). In the case of the nucleation fields, for low aspect ratios (lower than 7), in both 4.8a and 4.8b, they appear to not follow the same trend as the others, this may be explained as being the lower limit of the behaviour, when the assumption "thin disc" falls short [47] and the remanent state tends to the single domain.

4.1.4 Magnetic susceptibility

The linear part of the loop can be associated with the vortex core motion, as reported by Guslienko *et al.* [20]. In remanence, when the vortex is (ideally) in the centre of the disc,

the moments are aligned with the borders. As the magnetic field is applied, the magnetic moments tend to align with it, disturbing the prior magnetic state and leading to a vortex core motion perpendicular to the applied field. Thus, as the magnetic susceptibility can be related with the derivative of the magnetic moment versus to the field, one can relate it to how easily a vortex core is disturbed and set in motion by an external magnetic field. Guslienko *et al.* [20] proposed a model equation for this behaviour in permalloy discs

$$\chi(0) = \frac{A}{B\beta(ln(\frac{C}{\beta}) + D)} \tag{4.1}$$

with A=1, B=2, C=8, D=$\frac{1}{2}$ and $\beta = t/D$, the inverse of the aspect ratio definition used in this thesis.

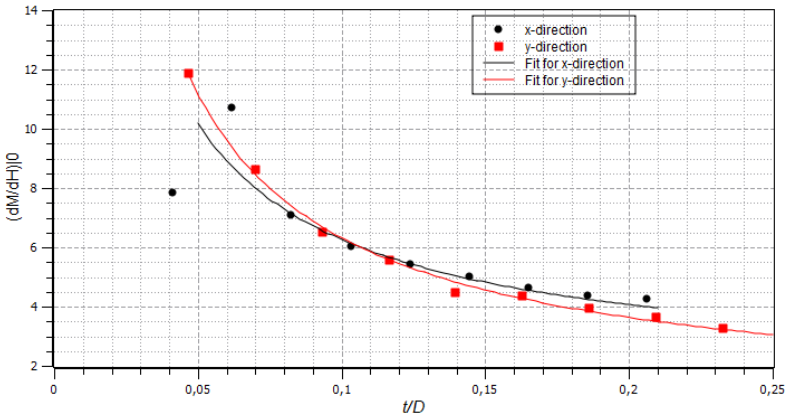

FIGURE 4.9: Magnetic susceptibility as a function of $\beta = t/D$.

In Figure 4.9, it can be observed the relationship between the slope around zero field and the thickness of the sample, although the low thickness stands out. The dM/dH, in the x-direction, for samples with 20 nm of Fe is noticeably lower than the others, which supports the claim that this sample is not in the vortex state. This was the reason it was not included in the region to be fitted by 4.1. The dM/dH, in the y-direction, for 100 nm of Fe also seems to deviate more from the tendency than the value in the x-direction, once again highlighting how the different sizes of both axes affect the hysteresis loop for the same thickness. Other than the already mentioned outlier points, the simulated data appears to be in good agreement with the proposed model, as expected. The behaviour of the slope values seems to indicate that discs with smaller thickness have a higher mobility of the vortex core under an in-plane applied magnetic field. It is also worth noting that the susceptibility increases sharply near the dot's instability region, where it is expected a transition of the vortex state to the in-plane magnetized single domain state, as suggested

by Guslienko *et al.* [20, 51]. This model was fitted to the simulated data, resulting in Figure 4.9. The parameters obtained wereA=1.75, B=4.41, C=-0.768, D=0.926 and A=1.8, B=1.12, C=0.28, D=1.55 for the x- and y-direction, respectively.

4.2 Ideal discs

For biological applications the size of the nanostructures has to be well controlled, being beneficial diminishing the size from the already fabricated samples (500 nm) [6]. Keeping this in mind, another fabrication route was considered, such as nanoporous alumina templates (see subsection 2.1.2). In this section, comprehensive simulations were based on circular cylinders. The objective was to better understand the dimension limits of the ideal vortex behaviour, without having to worry about in-plane intrinsic anisotropies. The parameters in direct study were the discs aspect ratio and inter-dot distance. Figure 4.10 shows the vortex state, in remanence, for a Fe disc with t =50 nm.

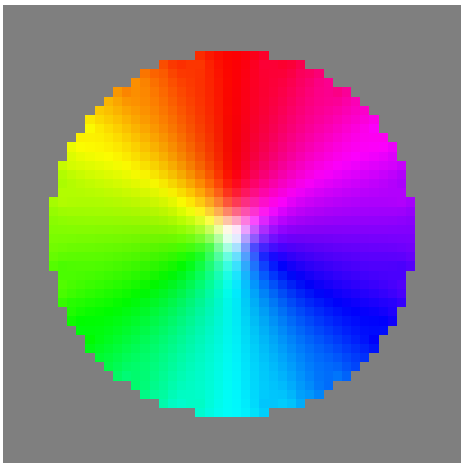

FIGURE 4.10: Simulated image of the remanent state of the Fe disc, for 50 nm.

For studying the inter-dot distance, four diameters (200, 300, 400 and 500) were set, varying the inter-dot distance from $R/4$ to just above $2R$, with $24R/10$. One of the alumina templates' key features is the dependence between the pore diameter of the pore and the interdot distance (see subsection 2.1.2.1), thus, the first objective here was to assert which disc separation was the threshold to consider a disc isolated. In Figure 4.11 two hysteresis loops for different interdot distances are shown. Here, despite sharing the same overall shape, a clear difference in the vortex characteristic fields is observable and shall be addressed in the next subsection.

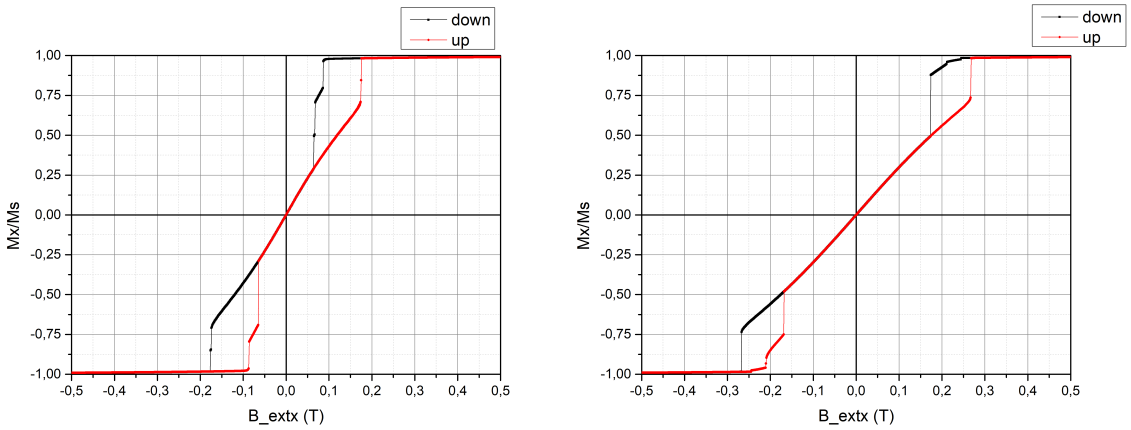

(A) Interdot distance of 25 nm.

(B) Interdot distance of 200 nm.

FIGURE 4.11: Hysteresis loops for discs of $D = 200$ nm, $t = 50$ nm and different interdot distances.

Several different combinations of thickness and diameter were simulated to study the dependence in aspect ratio, and can be schematized in Figure 4.12, accompanied by a few chosen hysteresis loops 4.13.

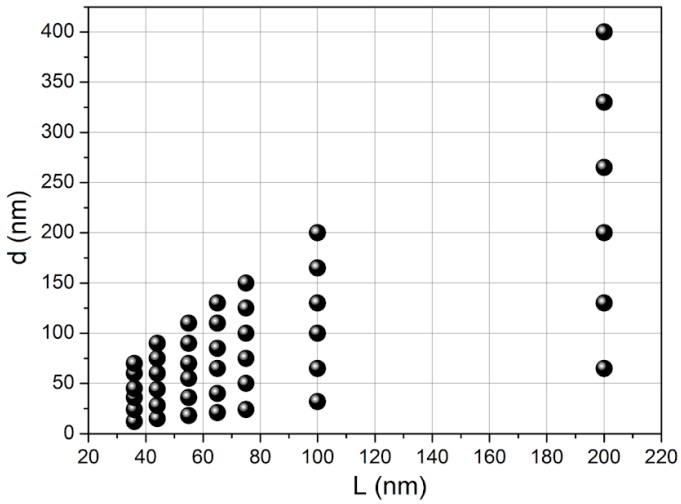

FIGURE 4.12: All different combinations of thickness and diameter of the simulated discs

In Figure 4.13 are represented some of the different combinations of simulated data, where a typical vortex-state hysteresis loop is present, with two abrupt transitions, zero remanence and a linear behaviour around zero field. The difference between these hysteresis loops is the values of the field at which nucleation (H_n) and annihilation (H_a) take place, as also de slope value of the near zero-field behaviour. All of this is to be discussed more in the next sections.

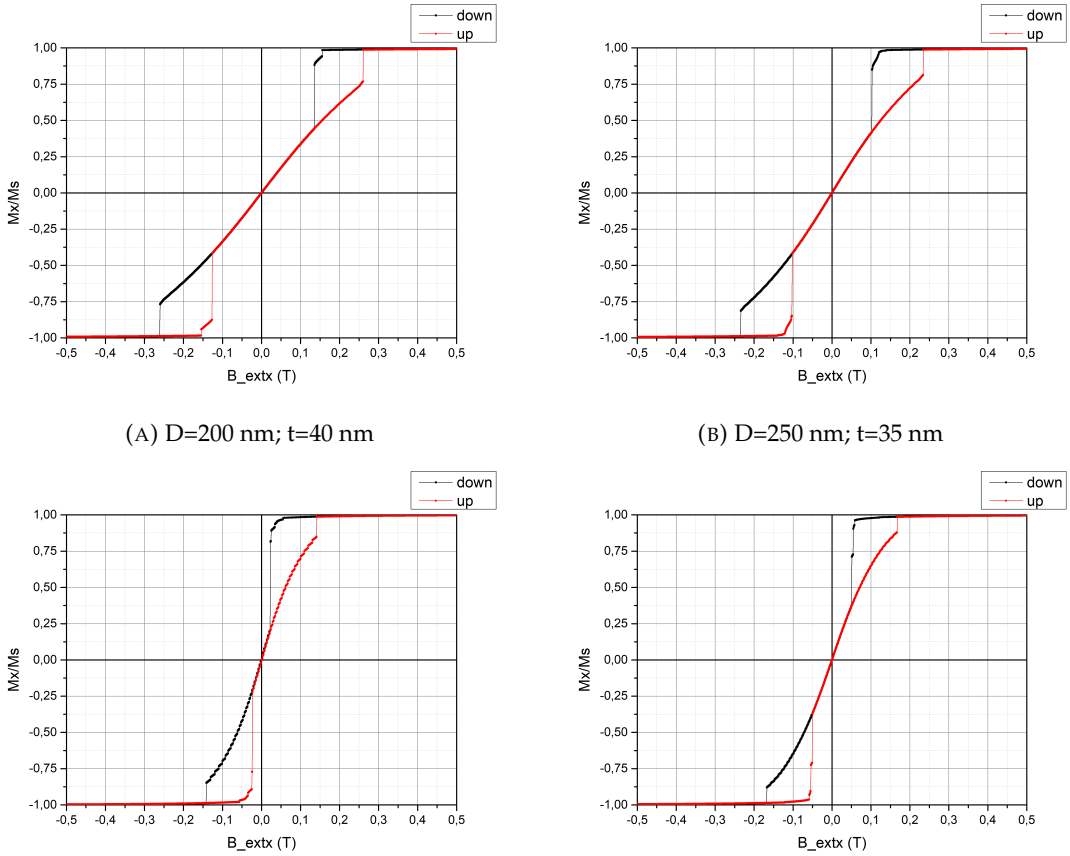

(A) D=200 nm; t=40 nm

(B) D=250 nm; t=35 nm

(C) D=300 nm; t=30 nm

(D) D=400 nm; t=25 nm

FIGURE 4.13: Hysteresis loops for different aspect ratio combinations.

4.2.1 Vortex characteristic fields

The vortex characteristic fields' dependence with the interdot distance is presented here in Figure 4.14. The values for the nucleation and annihilation fields, for the same diameter, increase rapidly between $R/4$ to $4R/5$ and then starts to increase more slowly between R and $2R$, before stagnating completely. The increased magnetostatic interactions, for smaller distances, lead to the lowering of the needed field to nucleate a vortex or annihilate it. When the distance becomes large enough, this effect is negligible and the disc can be regarded as isolated. The described behaviour is transversal to all of the four different diameters studied. The threshold seems to be $2R$ but the difference between R and $2R$ is small enough to not be important in situations where a close-packed structure is desirable, as in magnetic memories [2–4, 52].

Using the diameter/thickness combinations displayed in table 4.12, the behaviour of the nucleation and annihilation fields with increasing aspect ratio is studied and illustrated in Figure 4.15. Here, the same broad behaviour of Figure 4.8 is present, where

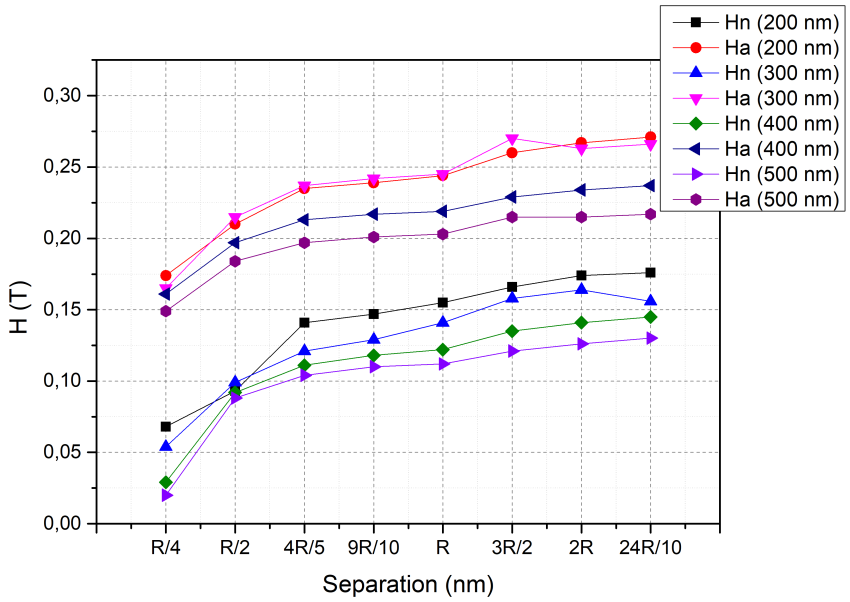

FIGURE 4.14: Nucleation (H_n) and Anihilation (H_a) fields for different interdot distance.

with increasing aspect ratio, the vortex characteristic fields decrease. This has also been discussed in subsection 1.1.3.1.

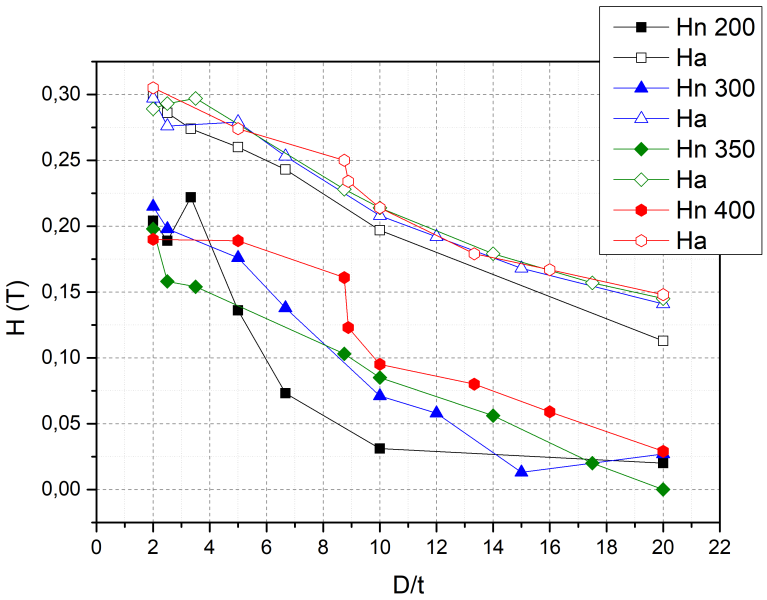

FIGURE 4.15: Nucleation and Anihilation fields for different aspect ratios.

In Figure 4.16 the nucleation and annihilation fields of discs for five different diameters, with varying thickness, are presented. The tendency here is a non-linear increase, where the last points start to behave irregularly, especially in the nucleation field. There

is an increase, in the nucleation field, until $t = 100$ nm, after which it becomes practically independent of t. On the other hand, the annihilation field increases until $t = 50$ nm, behaving irregularly towards saturation after. This irregular behaviour can be interpreted as the effects of being on the limiting part of the vortex state [17, 21]. For investigating how

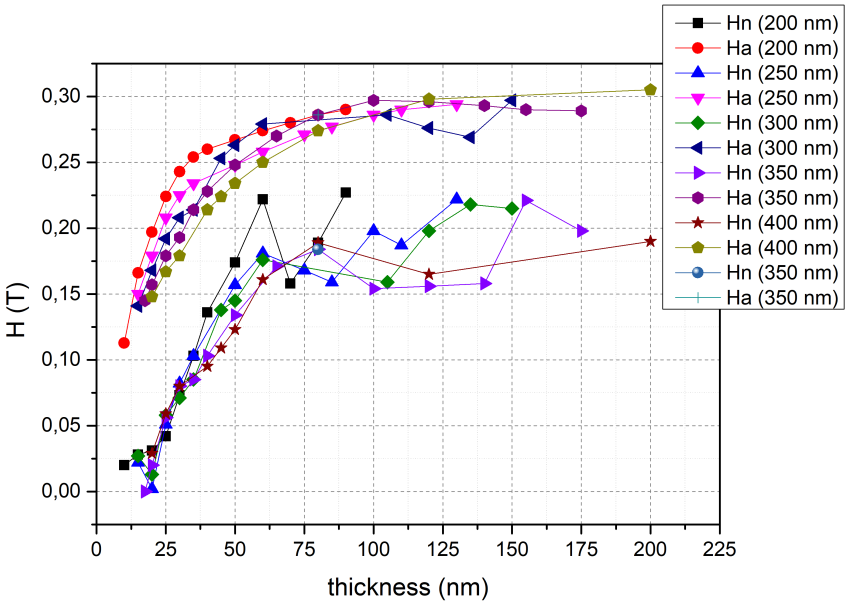

FIGURE 4.16: Nucleation and Anihilation fields for different thickness.

the diameter influenced the characteristic fields, discs with constant thickness ($t = 50$) and varying diameter were simulated.

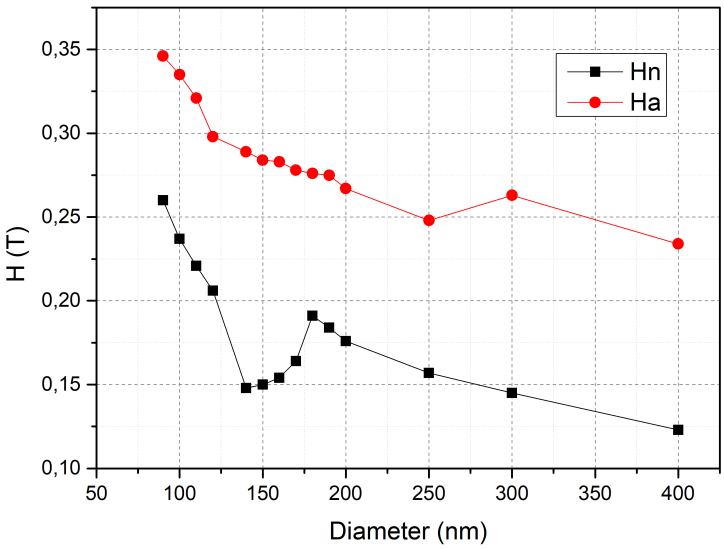

FIGURE 4.17: Nucleation and Anihilation fields for different Diameters.

The results are presented in Figure 4.17. In hindsight, it was probably an incongruence not to make the unchanging parameter the aspect ratio. The first discs fields' values are probably more due to the very low aspect ratio than because of some influence of the diameter. This can be assumed by looking at the pronounced inflexion point in the graph, where possibly the aspect ratio effect importance is greatly decreasing. As a result, not a lot of information can be inferred from this, other than the broad decreasing tendency.

4.2.2 Magnetic susceptibility

In Figure 4.18, a non-linear decrease can be observed, for all of the five different diameters, with varying thickness. Once again this goes in line with the theory proposed by

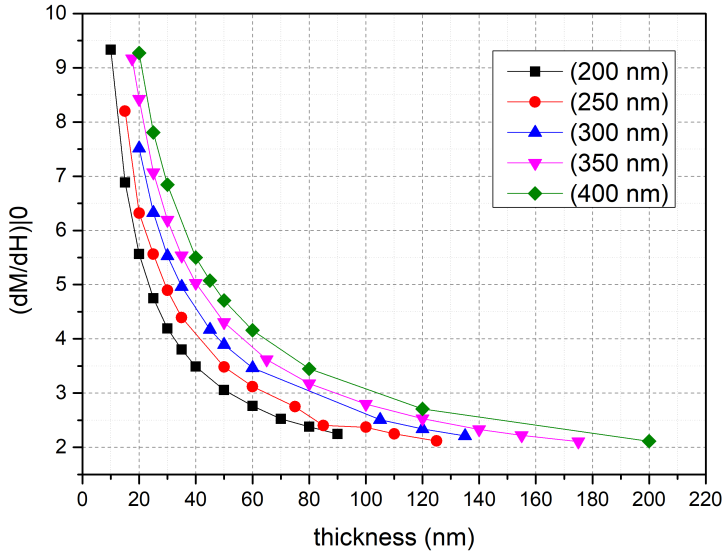

FIGURE 4.18: Magnetic susceptibility as a function of the thickness.

Guslienko *et al.* [20] and the discussion of Figure 4.9, reinforcing the idea that the vortex core's mobility decrease with the increasing thickness. The proposed model was also fitted (Figure 4.19 with the obtained parameters illustrated in table 4.1.

diameter (nm) /parameters	A	B	C	D
200	1,53	0,832	1,30	0,798
250	1,44	1,26	0,903	0,753
300	2,96	0,314	1,84	1,98
350	1,06	0,908	1,22	0,560
400	1,34	0,498	1,09	1,09

TABLE 4.1: Parameters of the fitting.

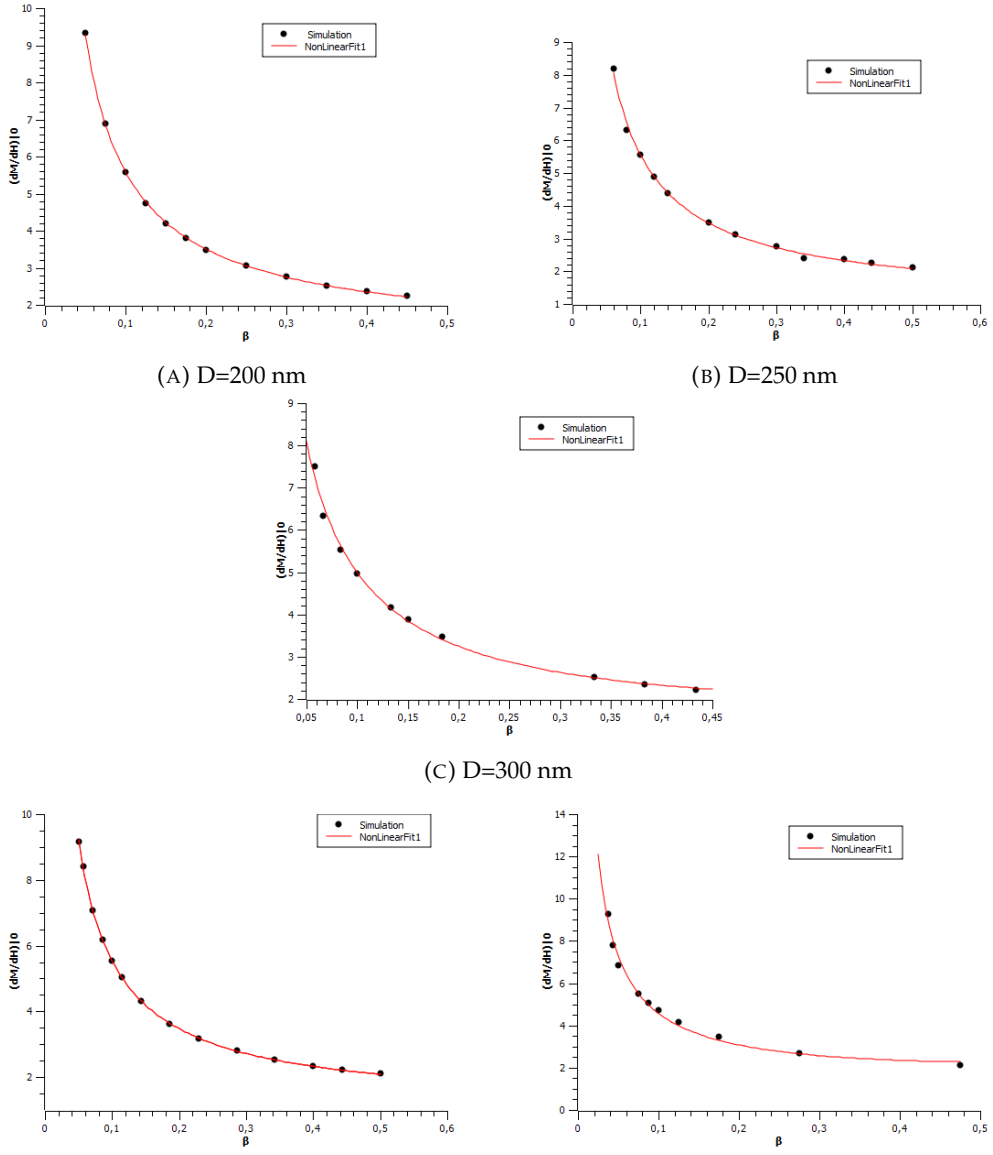

(A) D=200 nm

(B) D=250 nm

(C) D=300 nm

(D) D=350 nm

(E) D=400 nm

FIGURE 4.19: Magnetic susceptibility as a function of $\beta = t/D$, for different diameters.

The field's dependency, on the interdot distance represented in Figure 4.20, can again be explained by the fact that being so close, the dots' magnetic moments cause their neighbours to feel higher fields than the externally applied magnetic field. With more close-packed disc arrays, more this effect is felt, thus leading to each vortex core needing less applied field to move. As the disc separation increases, the slope value stabilizes, meaning that the disc can be considered not-affected by its neighbours, being an isolated disc [23].

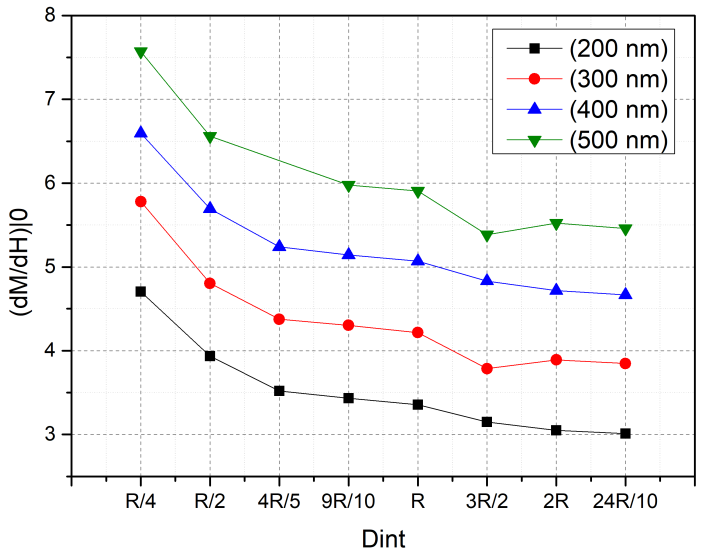

FIGURE 4.20: Magnetic susceptibility as a function of interdot distance.

Despite the vortex characteristic fields dependence in the diameter not turning up quite as desired, the magnetic susceptibility analysis still followed. Figure 4.21 shows a linear tendency in this dependence.

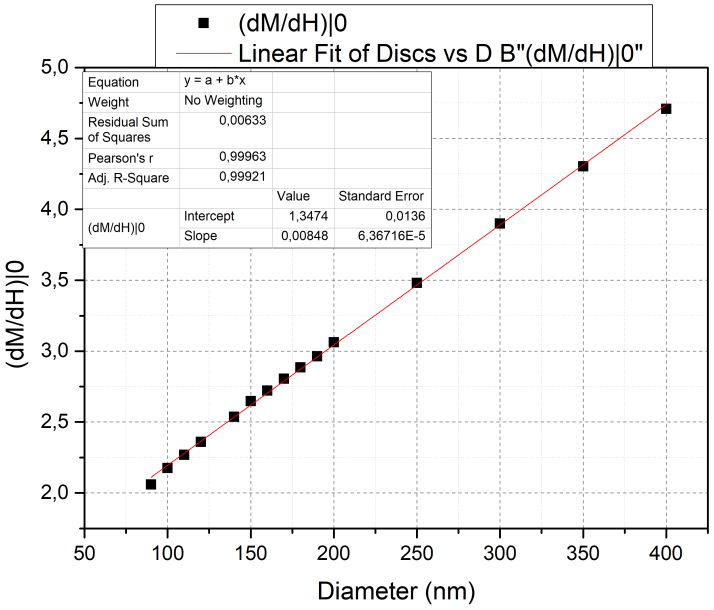

FIGURE 4.21: Magnetic susceptibility as a function of the Diameter.

The vortex core seems to be easier to disturb the larger the disc is. The lower values of the diameter seem to deviate more from the linear tendency than those above 150 nm,

which is understandable given the reason presented in the prior subsection.

The underlying objectives of this study were to identify which combinations of aspect ratio would be favourable to the formation of a vortex-state for future applicabilities for biotechnological purposes and, ideally, using nanoporous alumina templates and better understand the experimental results of section 3.1.2. Throughout this chapter, it was made clear that thin discs with an aspect ratio, $r = D/t$, between 5 and 15 are within a region where the vortex state is present. Thus, it would be a good choice for future fabrication with nanoporous alumina templates an aspect ratio that sits somewhere in between those value. For example, with D=100 nm the thickness could vary from t= 7 nm to t= 20 nm. Applying this knowledge to the discs in the template (defined by interference lithography) of D 500 nm, the thickness at which a vortex state should be present ranges from t= 30 nm to t=90 nm. This rules out the lack of uniformity in the thermal evaporation as the main problem, as the thickness would have to be very different from 50 nm to loose de vortex state.

Chapter 5

Nanodiscs in biomedical applications

This chapter regards the cell uptake and viability studies of the previously fabricated samples, for future bio-applications.

5.1 Introduction

For these nano-discs to be applicable to magneto mechanically induced damage techniques, their effect on the cells has to be studied. Despite not having measurements that indicate a clear vortex state, the thermally evaporated samples could still be used to evaluate particle uptake and cell viability. These parameters were assessed at this stage, with the use of flow cytometry. Flow cytometry is a technique used for separating, counting, examining and classifying cells, as they flow in a fluid stream through a beam of light. Different parameters allow for the measurement of different cellular characteristics, such as relative size (forward scattered light), relative granularity or internal complexity (side scattered light), and relative fluorescent intensity (Fluorescence) [78]. This technique is widely used to assess cell viability and particle uptake [79–82], which is why it was decided to be used in this work.

5.2 Experimental methods

5.2.1 Disc removal

The removal of the Al sacrificial layer was done using a solution of KOH (15%) in an ultrasound bath. The released discs were then collected using a magnet. This process was repeated several times, for each sample, to ensure maximum efficacy. Although it can be

assumed that some discs were irredeemably lost, at least it is reasonable to assume that the number of discs is in the same order of magnitude.

5.2.2 Flow cytometry

Human leukaemia monocyte THP1 cell line was obtained from European Culture Collections (Salisbury, UK). The monocytes were prepared in a 24-well plate with different nano-disc concentration in 300 μL of pH 7.4 buffer, as schematized in Figure 5.1. Each well corresponded to 50.000 cells that were grown in DMEM supplemented with fetal bovine serum and penicillin/streptomycin at 37 °C with 5 % CO_2. The cells were incubated with the nanodiscs, also at 37 °C, for 19h. The cells were examined in the BD Accuri^{TM} C6 flow cytometer.

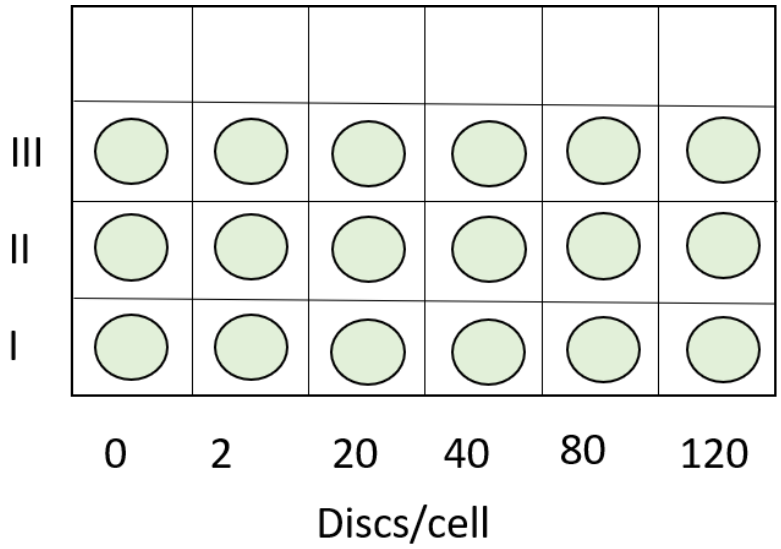

FIGURE 5.1: Schematization of the arrangment in the 24-well plate.

5.3 Results

Using image analysis software ImageJ, SEM images (Figure 3.1) and given the area of the samples the number of discs was estimated to be in the order of 2×10^9.

5.3.1 Cell Viability

The cells were stained with propidium iodide, as it is permeant to live cells. This allowed to evaluate the toxicity of the nanodiscs was evaluated in monocytes cultures, for different concentrations. The results of the cell viability studies are shown in Figure 5.2. Every

concentration available had less than 10% of dead cells, which leads us to believe that this nano-discs are innocuous without an applied magnetic field.

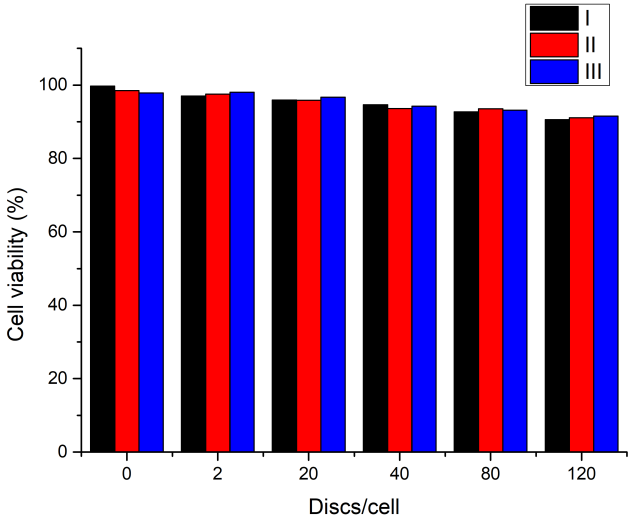

FIGURE 5.2: Percentage of cell viability with the number of discs per cell.

5.3.2 Particle uptake

The difference in the height of the side scattered light (SSC-H) was measured to infer particle uptake. The results are summarized in Figure 5.3. As mentioned before, the analysis of the SSC-H allows for an assessment of the internal complexity or relative granularity, so by comparing these results, it can be seen that the discs were internalized. The smaller differences for higher concentrations may reveal to be because of some form of saturation.

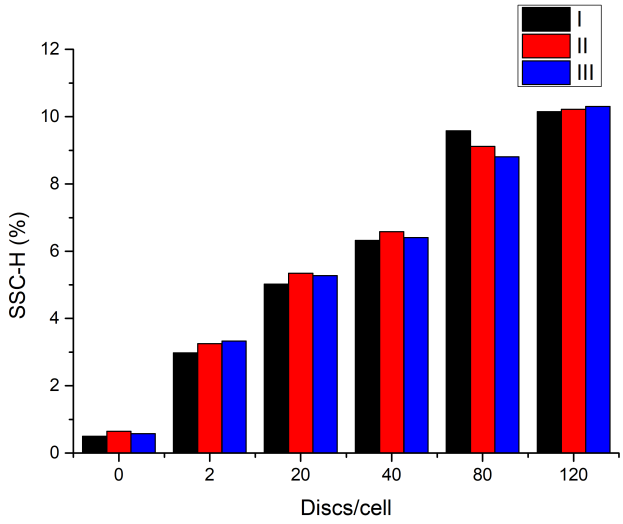

FIGURE 5.3: Percentage of SSC-H with the number of discs per cell.

This chapter served the purpose to start to bridge the gap between the physical concepts and its potential applications. These studies allowed us to evaluate two fundamental paramenters for potencial biomedical application: disc uptake and toxicity. The results presented makes them good candidates for bio-applications, namely magneto mechanically induced damage.

Chapter 6

Final remarks and future work

The development and comprehension of different magnetic effects is of the uttermost importance in the pursuit of novel solutions, namely for the biotechnological field. With this in mind, the vortex state, in nanodiscs, and its dependance on aspect ratio and interdot distance was studied.

Thermally evaporated nanodiscs (layers of Al, Au, Fe, Au) were fully characterized with help of scanning electron microscopy (SEM), X-ray diffraction (XRD), superconducting quantum interference device (SQUID), magneto-optic Kerr effect (MOKE) and ferromagnetic resonance (FMR). FMR measurements let us infer that the thermally evaporated samples suffered from a contamination/non-uniformity issue. This was probably due to some oxidation of the Fe layer. However, the vortex state was still found in some regions of these samples. New discs (layers of Al, Ti, Fe, Ti) were fabricated, by ion beam deposition, on the substrate previously patterned by interference lithography. The choice of this technique was supported by FMR measurements. These discs were also characterized with the same techniques, but the lift-off process was not optimized; not all the photoresist and thin film were removed, which affected the results. The magnetic mesurements ought to be repetead when the lift -off process is completed.

Micromagnetic simulations were performed based on the SEM images of the fabricated discs to better understand and predict the results. Here, the only parameter varied was the thickness of the discs and it was found that the vortex state should be present for thicknesses, t, between 30 and 90 nm. Following this, several simulations were performed with ideal discs in mind. The behaviour of the vortex state with respect to the interdot distance, d, and aspect ratio, $r = D/t$, was studied. It was found that when $d \geq D$, the interaction between discs is negligible. The vortex state was observed to be present in

remanence from r= 5 to r=15. The magnetic susceptibility of this magnetic state was also studied with respect to the above mentioned parameters, with the results in agreement with the literature.

Porous alumina templates were fabricated and used for electrodepositing Fe (6, 9, 12, 15 s) and Cu (450 s) segmented nanowires. The objective here was to begin operating with a bottom-up method, using the knowledge obtained from the simulations. The nanowires were then analysed with vibrating sample magnetometer (VSM) but the vortex state was not observable. Measurements with higher accuracy are to be performed, using SQUID at low temperatures. The electrodeposition process also needs to be optimized.

The discs fabricated by thermal evaporation were released from the substrate and used to test cell viability and cellular uptake, with different concentrations (0, 2, 20, 40, 80, 120 discs/cell), by flow cytometry. The discs were observed to have been internalized. It was observed that the increase in particle uptake between 80 and 120 discs/cell was small, meaning that we could be reaching a saturation region. None of the concentrations resulted in a cell survivability of less than 90 %, which means that the discs are innocuous, without an applied magnetic field. In the future, the discs fabricated would be used to progress the study with cell lines towards the application of magneto-mechanically induced damage.

New discs should be fabricated by using more substrates patterned by interference lithography, electrodeposition on porous alumina template, or even by combining porous alumina templates with IBD.

Appendix A

Mumax code

Code for simulating magnetization reversal for the experimental discs

```
1  //Magnetic Material Parameters
2  ////////////////////////////////
3  //Isolated Fe dot (Real)
4
5  Msat_Fe := 1700e3 // Magnetizacao de Saturacao (A/m)
6  Aex_Fe := 2.1e-11 //Exchange Stiffness (J/m)
7  Kc1_Fe := 4.8e4  //Magnetocristalline Anisotropy (J/m3)
8  Kc2_Fe := 0
9  Kc1v_Fe := vector(cos(45*pi/180), 0, -sin(45*pi/180))
10 Kc2v_Fe := vector(cos(45*pi/180), 0, sin(45*pi/180))
11
12
13
14 //Geometric Parameters
15 ///////////////////////
16
17 XCells := 150   // Number of cells on x axis
18 YCells := 150   // Number of cells on y axis
19 ZCells := 20    // Number of cells on z axis
20 SpaceSizeX_Int := 750   // Size of simulated sample
21 SpaceSizeY_Int := 750   // Size of simulated sample
22 SpaceSizeZ_Int := 100    // Size of simulated sample
23 SpaceSizeX := SpaceSizeX_Int*1e-9
24 SpaceSizeY := SpaceSizeY_Int*1e-9
```

```
25 SpaceSizeZ := SpaceSizeZ_Int*1e-9
26
27 CellSizeX_Int := SpaceSizeX_Int/XCells
28 CellSizeY_Int := SpaceSizeY_Int/YCells
29 CellSizeZ_Int := SpaceSizeZ_Int/ZCells
30 CellSizeX := CellSizeX_Int*1e-9
31 CellSizeY := CellSizeY_Int*1e-9
32 CellSizeZ := CellSizeZ_Int*1e-9
33
34 SetPBC(30, 30, 0)   // Periodic Boundarey Conditions
35
36 SetGridsize(XCells, YCells, ZCells)
37 SetCellsize(CellSizeX, CellSizeY, CellSizeZ)
38
39 //Geometry Definitions
40 ////////////////////////
41
42 EdgeSmooth = 0
43
44 Dot_Fe := imageShape("E:/Mumax_Sim/Ludgero/Fe_dots_Bilbao/
       Fe_1Disk_750x750nm_Final.jpg")
45
46 setgeom(Dot_Fe)
47
48 saveas(geom, "Dot_Fe_Geom")
49
50 //Magnetic Properties Assignment
51 ////////////////////////////////
52 //Fe
53
54 DefRegion(1, Dot_Fe)
55 Msat.SetRegion(1, Msat_Fe)
56 Aex.SetRegion(1, Aex_Fe)
57 KC1.SetRegion(1, Kc1_Fe)
58 KC2.SetRegion(1, Kc2_Fe)
59 AnisC1.SetRegion(1, Kc1v_Fe)
60 AnisC2.SetRegion(1, Kc2v_Fe)
61
62 //Saving Initial Parameters
63 ///////////////////////////
64
```

```
65 saveas(Msat, "Dot_Msat_Fe")
66 saveas(Aex, "Dot_Fe_Exchange")
67 saveas(regions, "Dot_Fe_Regions")
68 saveas(KC1, "Dot_Fe_KC1_Values")
69 saveas(KC2, "Dot_Fe_KC2_Values")
70 saveas(AnisC1, "Dot_Fe_AnisVectorsKC1")
71 saveas(AnisC2, "Dot_Fe_AnisVectorsKC2")
72
73 //Table Definitions
74 ////////////////////
75
76 tableadd(m_full)
77 tableadd(B_ext)
78
79 //Initial Magnetization
80 ////////////////////////
81
82 m = RandomMag()
83 saveas(m, "Dot_Fe_m_initial_Random.ovf")
84
85 //Evolver
86 /////////
87
88 SetSolver(5) //RK45
89 Out_Crit_Tor := 2.5e-4 //Max Torque relaxation criteria.
90 alpha = 0.5 //Landau-Lifshift damping
91 MaxErr = 1e-7
92 Dt_Sat := 0
93 MinimizerStop = 1e-6
94
95 //SIMULATION
96 ////////////
97
98 Bmax  := 1000.0e-3  // in Teslas
99 Bmin1  := 1.0e-3  // in Teslas
100 Bmin2  := -1.0e-3  // in Teslas
101 Bstep :=  1.0e-3  // in Teslas
102
103 BApp0 := 0.0000 //Field value in T.
104 B_ext = vector(0, BApp0, 0)
105 RunWhile(MaxTorque > Out_Crit_Tor) //Evolution until relaxation
```

```
saveas(m, "Fe_Disk_m_Demag_0.0000T.ovf")
TableSave()

for B:=0.0; B<=Bmax; B+=Bstep{
    B_ext = vector(0, B, 0)
    minimize()    // small changes best minimized by minimize()
    tablesave()
}

for B:=Bmax; B>=Bmin1; B-=Bstep{
    B_ext = vector(0, B, 0)
    minimize()    // small changes best minimized by minimize()
    tablesave()
}

B := 0.0000 //Field value in T
B_ext = vector(0, B, 0)
minimize()    // small changes best minimized by minimize()
saveas(m, "Fe_Disk_m_Reman_0.0000T.ovf")
tablesave()

for B:=Bmin2; B>=-Bmax; B-=Bstep{
    B_ext = vector(0, B, 0)
    minimize()    // small changes best minimized by minimize()
    tablesave()
}

for B:=-Bmax; B<=Bmax; B+=Bstep{
    B_ext = vector(0, B, 0)
    minimize()    // small changes best minimized by minimize()
    tablesave()
}
```

Code for simulating magnetization reversal for the ideal discs

```
//Magnetic Material Parameters
////////////////////////////
//Isolated Fe dot (Real)

Msat_Fe := 1700e3 // Magnetizacao de Saturacao (A/m)
```

```
6  Aex_Fe := 2.1e-11 //Exchange Stiffness (J/m)
7  Kc1_Fe := 4.8e4  //Magnetocristalline Anisotropy (J/m3)
8  Kc2_Fe := 0
9
10 Kc1v_Fe := vector(cos(45*pi/180), 0, -sin(45*pi/180))
11 Kc2v_Fe := vector(cos(45*pi/180), 0, sin(45*pi/180))
12
13 //Geometric Parameters
14 ////////////////////
15
16 XCells := 67*2   // Number of cells on x axis
17 YCells := 67*2   // Number of cells on y axis
18 ZCells := 10    // Number of cells on z axis
19 SpaceSizeX_Int := 335*2   // Size of simulated sample
20 SpaceSizeY_Int := 335*2   // Size of simulated sample
21 SpaceSizeZ_Int := 50    // Size of simulated sample
22 SpaceSizeX := SpaceSizeX_Int*1e-9
23 SpaceSizeY := SpaceSizeY_Int*1e-9
24 SpaceSizeZ := SpaceSizeZ_Int*1e-9
25
26 CellSizeX_Int := SpaceSizeX_Int/XCells
27 CellSizeY_Int := SpaceSizeY_Int/YCells
28 CellSizeZ_Int := SpaceSizeZ_Int/ZCells
29 CellSizeX := CellSizeX_Int*1e-9
30 CellSizeY := CellSizeY_Int*1e-9
31 CellSizeZ := CellSizeZ_Int*1e-9
32
33 SetPBC(30, 30, 0)   // Periodic Boundarey Conditions
34
35 SetGridsize(XCells, YCells, ZCells)
36 SetCellsize(CellSizeX, CellSizeY, CellSizeZ)
37
38 //Geometry Definitions
39 ////////////////////
40
41 EdgeSmooth = 0
42
43 Dot_Fe := cylinder(300e-9, 50e-9).repeat(3370e-10,3370e-10,0).Transl(15175e
       -10,15175e-10,0)
44
45 setgeom(Dot_Fe)
```

```
46
47 saveas(geom, "Dot_Fe_Geom")
48
49 //Magnetic Properties Assignment
50 ////////////////////////////////
51 //Fe
52
53 DefRegion(1, Dot_Fe)
54 Msat.SetRegion(1, Msat_Fe)
55 Aex.SetRegion(1, Aex_Fe)
56 KC1.SetRegion(1, Kc1_Fe)
57 KC2.SetRegion(1, Kc2_Fe)
58 AnisC1.SetRegion(1, Kc1v_Fe)
59 AnisC2.SetRegion(1, Kc2v_Fe)
60
61 //Saving Initial Parameters
62 ///////////////////////////
63
64 saveas(Msat, "Dot_Msat_Fe")
65 saveas(Aex, "Dot_Fe_Exchange")
66 saveas(regions, "Dot_Fe_Regions")
67 saveas(KC1, "Dot_Fe_KC1_Values")
68 saveas(KC2, "Dot_Fe_KC2_Values")
69 saveas(AnisC1, "Dot_Fe_AnisVectorsKC1")
70 saveas(AnisC2, "Dot_Fe_AnisVectorsKC2")
71
72 //Table Definitions
73 ///////////////////
74
75 tableadd(m_full)
76 tableadd(B_ext)
77
78 //Initial Magnetization
79 ///////////////////////
80
81 m = RandomMag()
82 saveas(m, "Dot_Fe_m_initial_Random.ovf")
83
84 //Evolver
85 /////////
86
```

```
87 SetSolver(5) //RK45
88 Out_Crit_Tor := 2.5e-4 //Max Torque relaxation criteria.
89 alpha = 0.5 //Landau-Lifshift damping
90 MaxErr = 1e-7
91 Dt_Sat := 0
92 MinimizerStop = 1e-6
93
94 //SIMULATION
95 ////////////
96
97 Bmax  := 1000.0e-3  // in Teslas
98 Bmin1  := 1.0e-3  // in Teslas
99 Bmin2  := -1.0e-3  // in Teslas
100 Bstep :=  1.0e-3  // in Teslas
101
102 BApp0 := 0.0000 //Field value in T.
103 B_ext = vector(BApp0, 0, 0)
104 RunWhile(MaxTorque > Out_Crit_Tor) //Evolution until relaxation
105 saveas(m, "Fe_Disk_m_Demag_0.0000T.ovf")
106 TableSave()
107
108 for B:=0.0; B<=Bmax; B+=Bstep{
109     B_ext = vector(B, 0, 0)
110     minimize()   // small changes best minimized by minimize()
111     tablesave()
112 }
113
114 for B:=Bmax; B>=Bmin1; B-=Bstep{
115     B_ext = vector(B, 0, 0)
116     minimize()   // small changes best minimized by minimize()
117     tablesave()
118 }
119
120 B := 0.0000 //Field value in T
121 B_ext = vector(B, 0, 0)
122 minimize()   // small changes best minimized by minimize()
123 saveas(m, "Fe_Disk_m_Reman_0.0000T.ovf")
124 tablesave()
125
126 for B:=Bmin2; B>=-Bmax; B-=Bstep{
127     B_ext = vector(B, 0, 0)
```

```
128     minimize()    // small changes best minimized by minimize()
129     tablesave()
130 }
131
132 for B:=-Bmax; B<=Bmax; B+=Bstep{
133     B_ext = vector(B, 0, 0)
134     minimize()    // small changes best minimized by minimize()
135     tablesave()
136 }
```

Bibliography

[1] A. Fernandez-Pacheco, R. Streubel, O. Fruchart, R. Hertel, P. Fischer, and R. P. Cowburn, *Three-dimensional nanomagnetism*, Nature Communications **8**, 15756 (2017).

[2] N. Nishimura, T. Hirai, A. Koganei, T. Ikeda, K. Okano, Y. Sekiguchi, and Y. Osada, *Magnetic tunnel junction device with perpendicular magnetization films for high-density magnetic random access memory*, Journal of Applied Physics **91**, 5246 (2002).

[3] R. P. Cowburn, *Room Temperature Magnetic Quantum Cellular Automata*, Science **287**, 1466 (2000).

[4] J. d'Albuquerque e Castro, D. Altbir, J. C. Retamal, and P. Vargas, *Scaling approach to the magnetic phase diagram of nanosized systems*, Physical Review Letters **88**, 2372021 (2002).

[5] Q. A. Pankhurst, J. Connolly, J. S. K, and J. Dobson, *Applications of magnetic nanoparticles in biomedicine*, Journal of physics D: Applied Physics **36**, R167 (2003).

[6] O. V. Salata, *Applications of nanoparticles in biology and medicine*, Journal of Nanobiotechnology **2**, 1 (2004), arXiv:NIHMS150003 .

[7] S. Dutz, R. Müller, D. Eberbeck, I. Hilger, and M. Zeisberger, *Magnetic nanoparticles adapted for specific biomedical applications*, Biomedizinische Technik **60**, 405 (2015).

[8] C. Sun, J. S. H. Lee, and M. Zhang, *Magnetic nanoparticles in MR imaging and drug delivery*, Advanced Drug Delivery Reviews **60**, 1252 (2008).

[9] L. Mohammed, H. G. Gomaa, D. Ragab, and J. Zhu, *Magnetic nanoparticles for environmental and biomedical applications: A review*, Particuology **30**, 1 (2017).

[10] Q. A. Pankhurst, N. K. Thanh, S. K. Jones, and J. Dobson, *Progress in applications of magnetic nanoparticles in biomedicine*, Journal of Physics D: Applied Physics **42**, 1 (2009).

[11] H. Rui, R. Xing, Z. Xu, Y. Hou, S. Goo, and S. Sun, *Synthesis, functionalization, and biomedical applications of multifunctional magnetic nanoparticles*, Advanced Materials **22**, 2729 (2010).

[12] D. H. Kim, E. A. Rozhkova, I. V. Ulasov, S. D. Bader, T. Rajh, M. S. Lesniak, and V. Novosad, *Biofunctionalized magnetic-vortex microdiscs for targeted cancer-cell destruction*, Nature Materials **9**, 165 (2010).

[13] S. Matsuda, E. Nakajima, T. Nakanishi, A. Hitsuji, *et al.*, *Effective induction of death in mesothelioma cells with magnetite nanoparticles under an alternating magnetic field*, Materials Science and Engineering C **81**, 90 (2017).

[14] M. Pashchanka and J. J. Schneider, *Origin of self-organisation in porous anodic alumina films derived from analogy with Rayleigh–Bénard convection cells*, Journal of Materials Chemistry **21**, 18761 (2011).

[15] C. T. de Sousa, *Development of Nanoporous Alumina Templates for Biotechnological Applications*, Master's thesis, Department of Physics and Astronomy Faculty of Sciences of the University of Porto (2011).

[16] W. F. Brown, *The Fundamental Theorem of Fine-Ferromagnetic-Particle Theory*, Journal of Applied Physics **39**, 993 (1968), https://doi.org/10.1063/1.1656363 .

[17] R. P. Cowburn, D. K. Koltsov, A. O. Adeyeye, M. E. Welland, and D. M. Tricker, *Single-domain circular nanomagnets*, Physical Review Letters **83**, 1042 (1999).

[18] A. Wachowiak, J. Wiebe, M. Bode, O. Pietzsch, M. Morgenstern, and R. Wiesendanger, *Direct observation of internal spin structure of magnetic vortex cores*, Science **298**, 577 (2002).

[19] T. Shinjo, T. Okuno, R. Hassdorf, †. K. Shigeto, and T. Ono, *Magnetic Vortex Core Observation in Circular Dots of Permalloy*, Science **289**, 930 (2000), http://science.sciencemag.org/content/289/5481/930.full.pdf .

[20] K. Y. Guslienko, V. Novosad, Y. Otani, H. Shima, and K. Fukamichi, *Field evolution of magnetic vortex state in ferromagnetic disks*, Applied Physics Letters **78**, 3848 (2001).

[21] M. Schneider, H. Hoffmann, S. Otto, T. Haug, and J. Zweck, *Stability of magnetic vortices in flat submicron permalloy cylinders*, Journal of Applied Physics **92**, 1466 (2002).

[22] J. M. Garcia-Martin, A. Thiaville, J. Miltat, T. Okuno, L. Vila, and L. Piraux, *Imaging magnetic vortices by magnetic force microscopy: Experiments and modelling*, Journal of Physics D: Applied Physics **37**, 965 (2004).

[23] V. Novosad, K. Y. Guslienko, H. Shima, Y. Otani, *et al.*, *Effect of interdot magnetostatic interaction on magnetization reversal in circular dot arrays*, Physical Review B **65**, 060402 (2002).

[24] X. Zhu, V. Metlushko, B. Ilic, and P. Grutter, *Direct Observation of Magnetostatic Coupling of Chain Arrays of Magnetic Disks*, IEEE Transactions on Magnetics **39**, 2744 (2003).

[25] R. Mansell, T. Vemulkar, D. C. M. C. Petit, Y. Cheng, J. Murphy, M. S. Lesniak, and R. P. Cowburn, *Magnetic particles with perpendicular anisotropy for mechanical cancer cell destruction*, Scientific Reports **7**, 4257 (2017).

[26] E. A. Rozhkova, V. Novosad, D. H. Kim, J. Pearson, R. Divan, T. Rajh, and S. D. Bader, *Ferromagnetic microdisks as carriers for biomedical applications*, Journal of Applied Physics **105**, 5 (2009).

[27] Szary, P. , *Indication of vortex stabilization and buckling in circular shaped magnetic nanostructures*, Journal of Applied Physics **107,(2010**, 1 (2010).

[28] A. Fernandez and C. J. Cerjan, *Nucleation and annihilation of magnetic vortices in submicron-scale Co dots*, Journal of Applied Physics **87**, 1395 (2000).

[29] T. Pokhil, D. Song, and J. Nowak, *Spin vortex states and hysteretic properties of submicron size NiFe elements*, Journal of Applied Physics **87**, 6319 (2000).

[30] a. Fernandez, M. Gibbons, M. Wall, and C. Cerjan, *Magnetic domain structure and magnetization reversal in submicron-scale Co dots*, Journal of Magnetism and Magnetic Materials **190**, 71 (1998).

[31] J. S. Neal, H. G. Roberts, M. R. Connolly, S. Crampin, S. J. Bending, G. Wastlbauer, and J. A. Bland, *Magnetisation reversal in epitaxial Fe(1 0 0) disks studied by high resolution scanning Hall probe microscopy*, Ultramicroscopy **106**, 614 (2006).

[32] L. J. Heyderman, H. H. Solak, C. David, D. Atkinson, R. P. Cowburn, and F. Nolting, *Arrays of nanoscale magnetic dots: Fabrication by x-ray interference lithography and characterization*, Applied Physics Letters **85**, 4989 (2004).

[33] X. Zhu, P. Grütter, V. Metlushko, and B. Ilic, *Magnetization reversal and configurational anisotropy of dense permalloy dot arrays*, Applied Physics Letters **80**, 4789 (2002).

[34] S. Okazaki, *High resolution optical lithography or high throughput electron beam lithography: The technical struggle from the micro to the nano-fabrication evolution*, Microelectronic Engineering **(2015)**, 23–35 (2015).

[35] S. R. J. Brueck, *Optical and interferometric lithography-nanotechnology enablers*, Proceedings of the IEEE **93**, 1704 (2005).

[36] P. A. Savale, *Physical Vapor Deposition (PVD) Methods for Synthesis of Thin Films: A Comparative Study*, Applied Science Research, 2016, **8**, 1 (2016).

[37] J. O. Edgar Alfonso and G. Cubillos, "Crystallization," (IntechOpen, 1970) Chap. 15 - Thin Film Growth Through Sputtering Technique and Its Applications, pp. 397–432.

[38] U. G. WOO LEE, RAN JI and K. NIELSCH, *Fast fabrication of long-range ordered porous aluminamembranes by hard anodization*, nature materials **VOL 5**, 741 (2006).

[39] F. Li, L. Zhang, and R. M. Metzger, *On the growth of highly ordered pores in anodized aluminum oxide*, Chemistry of Materials **10**, 2470 (1998).

[40] K. Nielsch, J. Choi, K. Schwirn, R. B. Wehrspohn, and U. Gosele, *Self-ordering regimes of porous alumina: The 10journal Nano Letters **VOLUME 2**, 677 (2002)*.

[41] W. Lee and S.-J. Park, *Porous Anodic Aluminum Oxide: Anodization and Templated Synthesis of Functional Nanostructures*, Chemical Reviews **114**, 7487 (2014).

[42] M. Susano, M. P. Proenca, S. Moraes, C. T. Sousa, and J. P. Araújo, *Tuning the magnetic properties of multisegmented Ni/Cu electrodeposited nanowires with controllable Ni lengths*, Nanotechnology **27**, 10pp (2016).

[43] C. T. Sousa, D. C. Leitao, M. P. Proenca, J. Ventura, A. M. Pereira, and J. P. Araujo, *Nanoporous alumina as templates for multifunctional applications*, Applied Physics Reviews **1**, 031102 (2014).

[44] Y. P. Ivanov, A. Chuvilin, L. G. Vivas, J. Kosel, O. Chubykalo-Fesenko, and M. Vázquez, *Single crystalline cylindrical nanowires – toward dense 3D arrays of magnetic vortices*, Scientific Reports **6** (2016), 10.1038/srep23844.

[45] T. Okuno, K. Shigeto, T. Ono, K. Mibu, and T. Shinjo, *MFM study of magnetic vortex cores in circular permalloy dots: behavior in external field*, Journal of Magnetism and Magnetic Materials **240**, 1 (2002).

[46] B. Mora, A. Perez-Valle, C. Redondo, M. D. Boyano, and R. Morales, *Cost-Effective Design of High-Magnetic Moment Nanostructures for Biotechnological Applications*, ACS Applied Materials & Interfaces **10**, 8165 (2018).

[47] J. A. Osborn, *Demagnetizing Factors of the General Ellipsoid*, Physical Review **67**, 1 (1945).

[48] M. S. Cohen, *Lorentz Microscopy of Small Ferromagnetic Particles*, Journal of Applied Physics **36**, 1 (1965).

[49] M. Schneider, H. Hoffmann, and J. Zweck, *Lorentz microscopy of circular ferromagnetic permalloy nanodisks*, Applied Physics Letters **77**, 2909 (2000).

[50] J. Mejía-López, D. Altbir, A. H. Romero, X. Batlle, I. V. Roshchin, C.-P. Li, and I. K. Schuller, *Vortex state and effect of anisotropy in sub-100-nm magnetic nanodots*, Journal of Applied Physics **100**, 104319 (2006).

[51] K. Y. Guslienko, V. Novosad, Y. Otani, H. Shima, and K. Fukamichi, *Magnetization reversal due to vortex nucleation, displacement, and annihilation in submicron ferromagnetic dot arrays*, Physical Review B - Condensed Matter and Materials Physics **65**, 244141 (2002).

[52] S. Bohlens, B. Krüger, A. Drews, M. Bolte, G. Meier, and D. Pfannkuche, *Current controlled random-access memory based on magnetic vortex handedness*, Applied Physics Letters **93**, 142508 (2008), https://doi.org/10.1063/1.2998584 .

[53] Y. Liu, S. Gliga, R. Hertel, and C. M. Schneider, *Current-induced magnetic vortex core switching in a Permalloy nanodisk*, Applied Physics Letters **91**, 9 (2007), arXiv:0702048 [cond-mat] .

[54] R. Antos and Y. Otani, *Simulations of the dynamic switching of vortex chirality in magnetic nanodisks by a uniform field pulse*, Physical Review B - Condensed Matter and Materials Physics **80**, 1 (2009), arXiv:0903.4653 .

[55] W. Jin, H. He, Y. Chen, and Y. Liu, *Controllable vortex polarity switching by spin polarized current*, Journal of Applied Physics **105**, 1 (2009).

[56] M. Zhang, C. M. Earhart, C. Ooi, R. J. Wilson, M. Tang, and S. X. Wang, *Functionalization of high-moment magnetic nanodisks for cell manipulation and separation*, Nano Research **6**, 745 (2013).

[57] N. A. Frey, S. Peng, K. Cheng, and S. Sun, *Magnetic nanoparticles: synthesis, functionalization, and applications in bioimaging and magnetic energy storage*, Chemical Society Reviews **38**, 2532 (2009).

[58] A. J. Cole, V. C. Yang, and A. E. David, *Cancer theranostics: the rise of targeted magnetic nanoparticles*, Trends in Biotechnology **29**, 323 (2011).

[59] A. Jordan, R. Scholz, P. Wust, H. Fähling, and Roland Felix, *Magnetic fluid hyperthermia (MFH): Cancer treatment with AC magnetic field induced excitation of biocompatible superparamagnetic nanoparticles*, Journal of Magnetism and Magnetic Materials **201**, 413 (1999).

[60] Y. Cheng, M. E. Muroski, D. C. Petit, R. Mansell, *et al.*, *Rotating magnetic field induced oscillation of magnetic particles for in vivo mechanical destruction of malignant glioma*, Journal of Controlled Release **223**, 75 (2016), arXiv:15334406 .

[61] W. J. Atkinson, I. A. Brezovich, and D. P. Chakraborty, *Usable Frequencies in Hyperthermia with Thermal Seeds*, IEEE Transactions on Biomedical Engineering **BME-31**, 70 (1984).

[62] R. Rosensweig, *Heating magnetic fluid with alternating magnetic field*, Journal of Magnetism and Magnetic Materials 252 (2002) 370–374 **252**, 370 (2002).

[63] K. Maier-Hauff, R. Rothe, R. Scholz, U. Gneveckow, *et al.*, *Intracranial Thermotherapy using Magnetic Nanoparticles Combined with External Beam Radiotherapy: Results of a Feasibility Study on Patients with Glioblastoma Multiforme*, Journal of Neuro-Oncology **81**, 53 (2006).

[64] J. W. Diggle, T. C. Downie, and C. W. Goulding, *Anodic oxide films on aluminum*, Chemical Reviews **69**, 365 (1969).

[65] H. Masuda and K. Fukuda, *Ordered Metal Nanohole Arrays Made by a Two-Step Replication of Honeycomb Structures of Anodic Alumina*, Science **268**, 1466 (1995).

[66] F. Keller, M. S. Hunter, and D. L. Robinson, *Structural Features of Oxide Coatings on Aluminum*, Journal of The Electrochemical Society **100**, 411 (1953).

[67] D. C. Leitao, A. Apolinario, C. T. Sousa, J. Ventura, J. B. Sousa, M. Vazquez, and J. P. Araujo, *Nanoscale Topography: A Tool to Enhance Pore Order and Pore Size Distribution in Anodic Aluminum Oxide*, The Journal of Physical Chemistry C **115**, 8567 (2011).

[68] R. Oriňáková, A. Turoňová, D. Kladeková, M. Gálová, and R. M. Smith, *Recent developments in the electrodeposition of nickel and some nickel-based alloys*, Journal of Applied Electrochemistry **36**, 957 (2006).

[69] M. Rafique, *Study of the Magnetoelectric Properties of Multiferroic Thin Films and Composites for Device Applications*, Master's thesis, COMSATS Institute of Information Technology (2015).

[70] C. T. Rueden, J. Schindelin, M. C. Hiner, B. E. DeZonia, A. E. Walter, E. T. Arena, and K. W. Eliceiri, *ImageJ2: ImageJ for the next generation of scientific image data*, BMC Bioinformatics **18** (2017), 10.1186/s12859-017-1934-z.

[71] I. Bensehil, A. Kharmouche, and A. Bourzami, *Synthesis, Structural, and Magnetic Properties of Fe Thin Films*, Journal of Superconductivity and Novel Magnetism **30**, 795 (2016).

[72] A. Bendjerad, S. Boukhtache, A. Benhaya, D. Luneau, H. El, and K. Benyahia, *Modeling of magnetic properties of iron thin films deposited by RF magnetron sputtering using Preisach model*, Serbian Journal of Electrical Engineering **13**, 229 (2016).

[73] A. Layadi, *A theoretical investigation of Ferromagnetic Resonance Linewidth and damping constants in coupled trilayer and spin valve systems*, AIP Advances **5**, 057113 (2015).

[74] J. R. Fermin, A. Azevedo, F. M. de Aguiar, B. Li, and S. M. Rezende, *Ferromagnetic resonance linewidth and anisotropy dispersions in thin Fe films*, Journal of Applied Physics **85**, 7316 (1999).

[75] A. P. Li, F. Müller, A. Birner, K. Nielsch, and U. Gösele, *Hexagonal pore arrays with a 50–420 nm interpore distance formed by self-organization in anodic alumina*, Journal of Applied Physics **84**, 6023 (1998).

[76] A. Vansteenkiste, J. Leliaert, M. Dvornik, M. Helsen, F. Garcia-Sanchez, and B. V. Waeyenberge, *The design and verification of MuMax3*, AIP Advances **4**, 107133 (2014).

[77] G. S. Abo, Y.-K. Hong, J. Park, J. Lee, W. Lee, and B.-C. Choi, *Definition of Magnetic Exchange Length*, IEEE Transactions on Magnetics **49**, 4937 (2013).

[78] P. Quirke, *Introduction to Flow Cytometry*, Journal of Clinical Pathology **45**, 275 (1992).

[79] M. Moskvin, M. Babič, S. Reis, M. M. Cruz, *et al.*, *Biological evaluation of surface-modified magnetic nanoparticles as a platform for colon cancer cell theranostics*, Colloids and Surfaces B: Biointerfaces **161**, 35 (2018).

[80] S. A. C. Lima, A. Gaspar, S. Reis, and L. Durães, *Multifunctional nanospheres for co-delivery of methotrexate and mild hyperthermia to colon cancer cells*, Materials Science and Engineering: C **75**, 1420 (2017).

[81] Q. Feng, Y. Liu, J. Huang, K. Chen, J. Huang, and K. Xiao, *Uptake, distribution, clearance, and toxicity of iron oxide nanoparticles with different sizes and coatings*, Scientific Reports **8** (2018), 10.1038/s41598-018-19628-z.

[82] S. A. C. Lima and S. Reis, *Temperature-responsive polymeric nanospheres containing methotrexate and gold nanoparticles: A multi-drug system for theranostic in rheumatoid arthritis*, Colloids and Surfaces B: Biointerfaces **133**, 378 (2015).